UNIVERSITY OF SOUTHAMPTON

Faculty of Physical Sciences and Engineering
Department of Physics and Astronomy

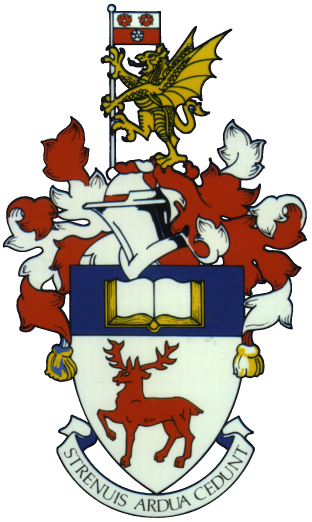

Multi-wavelength Observations of Accreting Compact Objects

by

Juan Venancio Hernández Santisteban

A thesis submitted for the degree of Doctor of Philosophy

November 2016

UNIVERSITY OF SOUTHAMPTON

ABSTRACT

FACULTY OF PHYSICAL SCIENCES AND ENGINEERING
DEPARTMENT OF PHYSICS AND ASTRONOMY

Doctor of Philosophy

MULTI-WAVELENGTH OBSERVATIONS OF ACCRETING COMPACT OBJECTS

by Juan Venancio Hernández Santisteban

The study of compact binaries invokes core astrophysical concepts ranging from stellar and sub-stellar atmospheres and interiors, stellar and binary evolution to physics of accretion. All of these systems are hosts to a compact object a white dwarf, neutron star or black hole − which produces a wide variety of exotic and energetic phenomena across the full electromagnetic spectrum. In this thesis, I will make use of multi-wavelength observations ranging from far-ultraviolet to near-infrared in order to investigate two main topics: a) the late evolution of cataclysmic variables, and b) the accreting state of transitional millisecond pulsars.

Firstly, I analyse the *Very Large Telescope* X-Shooter time-resolved spectroscopy of the short orbital period cataclysmic variable, SDSS J1433+1011, in Chapter 2. The wide wavelength coverage allowed me to perform a detailed characterisation of the system, as well as a direct mass measurement of the brown dwarf companion. I show that the donor in SDSS J1433+1011 successfully transitioned from the stellar to sub-stellar regime, as predicted by evolutionary models. Further light-curve modelling allowed me to show that a low albedo as well as a low heat-circulation efficiency is present in the atmosphere of the sub-stellar donor. In Chapter 3, I analyse data from large synoptic surveys, such as SDSS and PTF, to search for the predicted population of *dead* cataclysmic variables. Following the non-detection of dead CVs, I was able to estimate the space density ($\rho_0 < 2 \times 10^{-5}$ pc^{-3}) of this hidden population via a Monte Carlo simulation of the Galactic CV population. In Chapter 4, I present *Hubble Space Telescope* ultraviolet observations of the transitional millisecond pulsar PSR J1023+0038, during its latest accretion state. In combination with optical and near-infrared data, I show that a standard accretion disc does not reach the magnetosphere of the neutron star. Instead, the overall spectrum is consistent with a truncated disc at $\sim 2.3 \times 10^9$ cm away from the compact object. Furthermore, the ultraviolet data shares remarkable similarities with the only accreting white dwarf in a propeller regime, AE Aqr. Finally, I summarise my results in Chapter 5 and provide future lines of research in accreting compact binaries based on this work.

Contents

List of Figures

List of Tables

Declaration of Authorship

I, Juan Venancio Hernández Santisteban , declare that the thesis entitled *Multi-wavelength Observations of Accreting Compact Objects* and the work presented in the thesis are both my own, and have been generated by me as the result of my own original research. I confirm that:

- this work was done wholly or mainly while in candidature for a research degree at this University;
- where any part of this thesis has previously been submitted for a degree or any other qualification at this University or any other institution, this has been clearly stated;
- where I have consulted the published work of others, this is always clearly attributed;
- where I have quoted from the work of others, the source is always given. With the exception of such quotations, this thesis is entirely my own work;
- I have acknowledged all main sources of help;
- where the thesis is based on work done by myself jointly with others, I have made clear exactly what was done by others and what I have contributed myself;
- most of the work presented in Chapter 2 has been published as:

1. J. V. Hernández Santisteban, C. Knigge, S. P. Littlefair, R. P. Breton, V. S. Dhillon, B. T. Gänsicke, T. R. Marsh, M. L. Pretorius, J. Southworth & P. H. Hauschildt, *An irradiated brown-dwarf companion to an accreting white dwarf*, **Nature**, 2016, 511, 203.

and there are advanced manuscript versions for Chapters 3 and 4:

1. J. V. Hernández Santisteban, C. Knigge, M. L. Pretorius, M. Sullivan & B. Warner, *The Space Density of Post–Period Minimum Cataclysmic Variables*, **MNRAS**, in preparation
2. J. V. Hernández Santisteban, C. Knigge, D. Altamirano, A. Archibald, C. Bassa, J. Hessel, R. P. Breton, J. Patterson, J. Greiner & J. Matthews, *HST ultraviolet observations of the accretion state of PSR J1023+0038*, **MNRAS**, in preparation

Signed:.....

Date:.....

Acknowledgements

The last four years have been a fantastic period in my life. I have grown, both as a person as an astronomer, in great part by the invaluable help of friends and family over two continents. I have been fortunate to travel the world and meet amazing people at conferences and workshops. Here, I would like to thank most of the people that were involved during my PhD.

First, I would like to thank my supervisor Christian Knigge, for his incredible patience and will to teach me how to become an astrophysicist. He took a chance by accepting me as his student during our serendipitous meeting in Palermo back in 2011. Our meetings (even during my surprise 30th birthday party) and endless scribbles in the boards have shown me the path to become a better scientist. I also appreciate the freedom to pursue projects of my own, in occasions dragging him into them (uh... Opticam)! I cannot thank you enough for everything. A true inspiration for days ahead...

I would like to acknowledge all my friends and colleges at the Astronomy department. You have been an infinite well of laughter, good times, pub crawls, astrofootball, nerf wars, silly paper discussions and more importantly, a source of light at times when my PhD woes were too weary. Thanks to everyone including Sam, Rob, Aarran, Sadie, Boon, Adam, Regis, Georgios, Maxi, Magui, Szymon as well as my office mates throughout the years: Retha, Jess, Stew, James, Cfro and Judith.

To my family, back in Mexico and beyond. Your support has been crucial and our meetings throughout the world have been incredibly fun and rewarding. Thank you Adriana, Venancio, Adolfo, Adrián and my two grandparents Elda y Arnulfo.

Last but not least, I would like to thank and acknowledge the eternal support of my wife, Teresita. My journey in the past six years is not complete without you. Our time in this island has shaped who we are, as individuals and as a couple. You have written this thesis with me as well as shared the struggles and joys of it. Couldn't have done it without you. From the bottom of my heart, thank you!

Finally, I would like to thank the Consejo Nacional de Ciencia y Tecnología (CONACyT-México) and the University of Southampton, for their financial support via studentships. Also, I acknowledge the Royal Astronomical Society for their support on my academic visit to New York, USA. This research has made use of NASA's Astrophysics Data System Bibliographic Services. All plots in this thesis have been made with PYTHON and MATPLOTLIB (Hunter, J. D. 2007).

To Life, the Universe and Everything...

Chapter 1

Accreting Compact Binary Systems

> *"If we succeed, in this manner, in accounting for the changes observed on the relative situation of the two stars of a double star, we shall fail in proving them to form a binary system; but, in lieu of it, we shall gain two other points, of equal value to astronomers."*
>
> - William Herschel (1803), *on the discovery of Castor's binary nature*

Most of the stars in our Galaxy are known to be part of double or multiple systems (Duquennoy & Mayor 1991). As a result, their study has developed into one of the richest and most active research areas in astrophysics. Up to 50% of these binary systems have orbital periods (P_{orb}) short enough for mass transfer to occur, many of them containing compact objects such as white dwarfs, neutron stars or black holes (Chapter 2 in González Martínez-País et al. 2014). These *compact interacting binaries* are believed to be linked to several open questions in astrophysics, such as outcomes of common envelope events (Ivanova et al. 2013), progenitors of type Ia supernova(Yungelson & Livio 1998) and the make-up of the population of gravitational wave emitters (Paczyński 1967). The evolution of these systems is crucial for interpreting their influence on stellar (e.g. rates of cataclysmic events, mergers of compact objects, progenitors of γ-ray bursts) and galactic scales (e.g. chemical enrichment, diffuse γ-ray emission from Galactic centre). Furthermore, systems which contain a compact object can provide unique insights into the propagation of light and matter in the physics of extreme environments (e.g. the neutron star equation of state and strong gravity regime around black holes) which are not available in terrestrial experiments. They also emit radiation across a wide range of the electromagnetic spectrum, which makes them a prominent class of sources in observational surveys ranging from $\gamma-$rays to radio waves.

Perhaps the most important process that the mass transfer triggers is the formation of an accretion disc around the compact object. This structure provides the main source of luminosity in most accreting compact binaries, usually overwhelming the emission from the binary components. In recent years, much progress has been made in establishing the universality of disc accretion, for example by linking the observed variability time-scales of young-stellar objects, compact binaries and active galactic nuclei, across ten orders of magnitude in mass (e.g. Scaringi et al. 2015b). This common phenomenology (which also includes the rms-flux relationship (Uttley & McHardy 2001) and characteristic QPOs (Belloni et al. 2002)) suggests that disc accretion is a universal process, regardless of the nature of the accretor. Consequently, accreting compact objects (which are bright, numerous and nearby), are perfect laboratories for the study of accretion physics.

In this chapter, I will provide an overview of our current knowledge on accreting compact binaries, with particular focus on semi-detached systems (where the donor overflows its Roche lobe). The description of this binary set-up will provide a framework in which we can understand the general characteristics of white dwarf and neutron star accretors. I will also discuss the evolution and formation of such systems, concentrating on two specific sub-classes: cataclysmic variables and transitional millisecond pulsars.

1.1 The Zoo of Accreting Compact Objects

The zoo of accreting compact objects is large. Initially, the classification of these sources started as a phenomenological approach based on the observational properties of the objects. This approach is by no means perfect, so the resulting categories are not always consistent nor mutually exclusive. In addition, there exist many exceptions and outliers that defy easy classification. Nevertheless, the simplest and most useful way of classifying these objects is by the compact object, donor and accretion geometry, as exemplified in the diagram Figure 1.1.

White dwarf (WD) binaries are the most common type of compact interacting binary in the Galaxy. In general, these systems can be classified by the nature of their donor star and the manner in which they accrete. *Symbiotic stars* harbour a red giant that transfers mass to the WD via a wind loss (in most cases). In some symbiotic stars, the accreted material can form an accretion disc and show collimated jets during outbursts (Sokoloski 2003). *Cataclysmic variables* contain low-mass main sequence donors that transfer material to the WD by filling their Roche lobe. In most cases, this leads to the formation of an accretion disc that can be truncated depending on the strength of the magnetic field of the WD (Warner 1995). Finally, *AM CVn* systems are rare, short-period (5-65 min) binaries where the WD accretes from another degenerate object (most commonly a He WD) or semi-degenerate object (e.g. He star) via Roche-lobe overflow (Solheim 2010).

Accreting neutron stars (NS) and black holes (BH) are usually classified according to the mass of the companion. In general, high-mass X-ray binaries (HMXBs) and low-mass X-ray binaries (LMXBs) are mostly those systems where the donor has a mass of $\gtrsim$10 $M_\odot$and $\lesssim$1 $M_\odot$, respectively (Charles & Coe 2006). This classification by donor mass also provides insight into the accretion regime onto the compact object. In LMXBs, the donor star overflows its Roche lobe leading to the formation of an accretion disc around the compact object. In contrast, donors in HMXBs are found in longer orbits around the compact object. In these systems, the compact object often accretes from the stellar wind of the donor star (as in the symbiotic stars).

Furthermore, the main-sequence lifetime of the donor is tied to the overall lifespan of these systems. Thus, HMXBs are short-lived, with lifetimes of $\sim 10^5 - 10^7$ yr while LMXBs, with their less massive companions, are much longer lived ($\sim$ 1 Gyr). This explains why HMXBs are usually found in the Galactic plane or in the Large Magellanic Cloud, where a burst of star-formation occurred $\sim$ 100 Myr ago (Popov et al. 1998). In contrast, old LMXBs can reside much further above the Galactic plane and even in globular clusters.

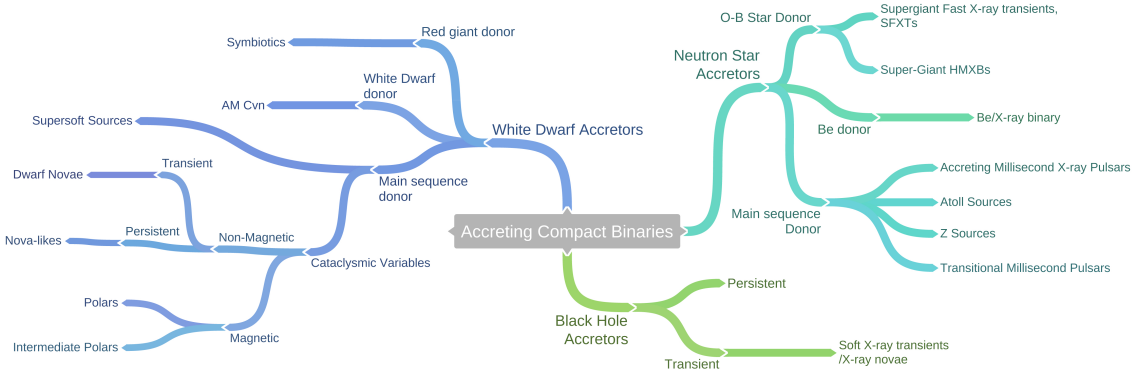

FIGURE 1.1: Accreting Compact Binary classification tree

1.2 Structure

Regardless of the nature of the compact accretor, semi-detached binary systems share a common geometry. In Figure 1.2, I present the basic set-up of such systems. They are composed of a compact object (primary component, sub-script 1) and a low-mass star/sub-stellar object (known as the companion or donor, sub-script 2). As they orbit around their common centre of mass, the donor star transfers material onto the primary. This material possesses enough angular momentum to avoid falling directly onto the compact object, instead settling in orbit around it. The viscous interactions between the accreted *particles* will lead to the formation of an accretion disc. In this following section, I will discuss the key aspects of this set-up in more detail.

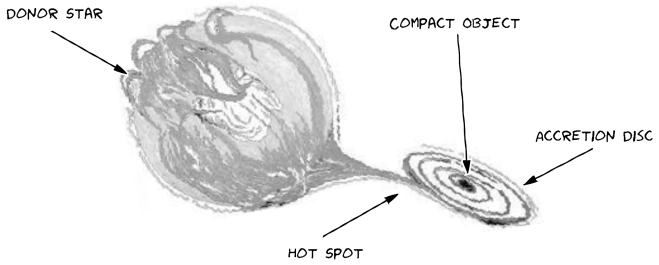

FIGURE 1.2: Accreting Compact Object schematic with main components of light source. Image adapted from Palermo's CVs workshop series.

1.2.1 The geometry

Semi-detached binary systems are generally well approximated by the so called Roche geometry (Kopal 1978). This geometry considers the orbits described by a test-particle in a gravitational potential of two more massive objects orbiting each other. In addition, both stars in the system are regarded as point masses, a generally valid assumption for centrally concentrated objects such as main-sequence stars and compact objects. In a Cartesian reference system, (x, y, z), where the origin coincides with the center of mass of the primary star, the donor star center of mass is fixed along the x-axis at an orbital separation a, as shown in Figure 1.3. The donor co-rotates with the binary system with an orbital period, P_{orb}, along the z-axis. This assumption is generally valid for close binaries since tidal synchronisation occurs in a shorter time scale than their main-sequence lifetime (Zahn 1975). Thus, the gravitational potential of the system is given by

$$\Phi_R = -\frac{GM_1}{(x^2+y^2+z^2)^{1/2}} - \frac{GM_2}{((x-a)^2+y^2+z^2)^{1/2}} - \frac{1}{2}\Omega_{orb}^2\left[(x-\mu a)^2+y^2\right], \quad (1.1)$$

where G is the gravitational constant, $\mu = M_2/[M_1+M_2]$ is the reduced mass, and $\Omega_{orb} = 2\pi/P_{orb}$ is the angular frequency of the system. The latter is related to the binary separation through Kepler's third law:

$$P_{orb}^2 = \frac{4\pi^2 a^3}{G(M_1+M_2)} \ . \quad (1.2)$$

This gravitational potential contains 5 critical point locations where the forces acting on a test mass are zero. These are known as Lagrangian points and shown in Figure 1.3. Of particular interest is the inner Lagrangian point, or L_1, situated along the axis of the orbital separation between both components. L_1 is a so-called *saddle point* in the potential surface i.e. where $\nabla\Phi_R = 0$. Thus, in the limit where the donor star fills its Roche lobe (the critical equi-potential surface that includes the L_1 point) material

located at L_1 forced gently towards the primary can flow and become gravitationally bound to the compact object. This process of Roche-lobe overflow (RLOF) thus leads to mass transfer from the Roche-lobe filling donor to the accretor.

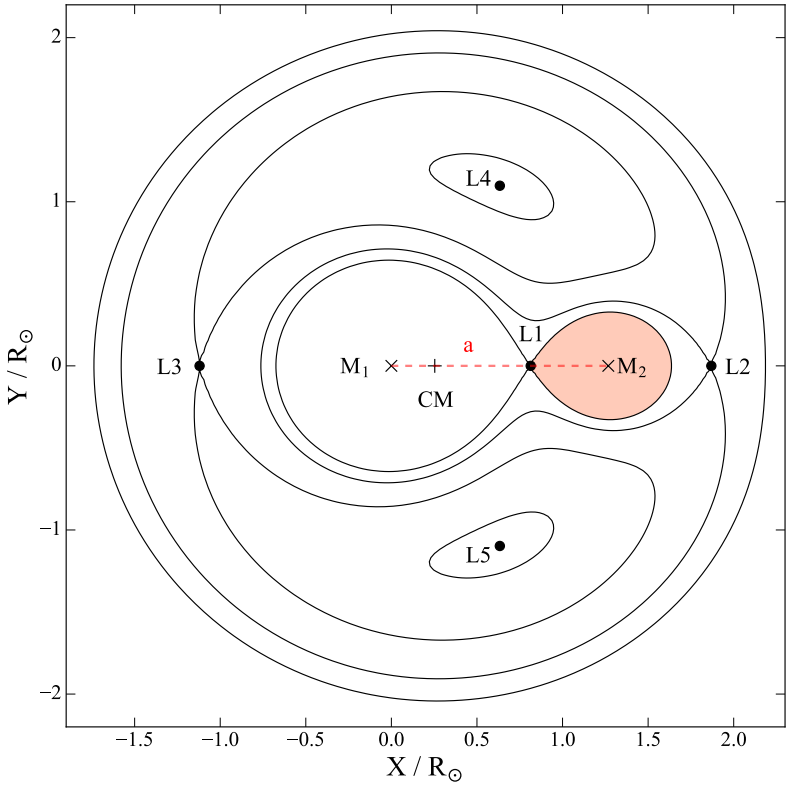

FIGURE 1.3: Roche equi-potential of a binary with $q = 0.25$. The five Lagrangian points ($L_{1...5}$, *circles*), the center of mass of each component ($M_{1,2}$, *hatch*), the common center of mass, CM, of the system (*cross*) are displayed for reference as well as the binary separation (a, *dashedline*).

As the donor star fills its Roche lobe, its geometry will deviate from spherical symmetry, instead resembling a tear-drop shape. However, it is often useful to approximate the donor as a spherical model. This is done by defining the *volume-averaged* radius, R_L, such that $V_2 = 4\pi R_L^3/3$, where V_2, is the volume of the donor. Thus the average density of the donor star, $\langle \rho_2 \rangle$, is given by:

$$\langle \rho_2 \rangle = \frac{M_2}{\frac{4}{3}\pi R_L^3} \ , \tag{1.3}$$

It is possible to calculate the volume of the Roche lobe numerically and construct analytic approximations for R_L as a function of a and the mass ratio, $q \equiv M_2/M_1$. The most simple approximation was proposed by Paczyński (1971):

$$\frac{R_L}{a} = 0.462 \left(\frac{q}{1+q} \right)^3 \quad 0.1 \lesssim q \lesssim 0.8, \tag{1.4}$$

However, a more widely used formula, due to its validity over the full range of q (to better than 1%), was proposed by Eggleton (1983):

$$\frac{R_L}{a} = \frac{0.49q^{2/3}}{0.6q^{2/3} + \ln\left(1+q^{1/3}\right)} \quad , \qquad 0 < q < \infty \quad . \tag{1.5}$$

A very useful relation can be obtained by combining Kepler's law (Equation 1.2) with Equation 1.4 (Paczyński's Roche-lobe approximation) to obtain the so-called period-density relationship:

$$\langle \rho_2 \rangle \simeq 110 P_{orb,h}^{-2} \quad \text{g cm}^{-3}, \tag{1.6}$$

where $P_{orb,h}$ is the orbital period in hours. This relationship allows us to obtain crucial insights. Lets define an approximate mass-radius relationship for a low-mass main sequence star given by $R/R_\odot = K(M/M_\odot)^\zeta$. If we adopt $K \simeq 1$ and $\zeta \simeq 1$, then we can find a mass-period relationship $M/M_\odot \simeq 0.1 P_{orb}$ (e.g. Echevarria 1983; Knigge 2011a). This simple exercise shows that low-mass main sequence stars have densities where they can easily fill their Roche-lobes for orbital periods $\lesssim$ 10 hr. Any system with longer P_{orb}, must contain a slightly evolved secondary in order to fill its Roche-lobe at the same given mass. Observationally, however, determining the mass and radius of individual components is challenging. Usually, we rely on dynamical information to recover these physical parameters. These observables are often obtained by the measurement of semi-amplitudes of radial velocity curves, $K_{1,2}$, from spectral features associated with each binary component (such as absorption or emission lines on the atmosphere of the stars). The radial velocity semi-amplitude for the system about the centre of mass in a circular orbit is given by

$$K_{1,2} = \frac{2\pi}{P_{orb}} a_{1,2} \sin i \quad , \tag{1.7}$$

where $a_{1,2}$ are the distance from the centre of mass to the centre of the each binary component (so $a = a_1 + a_2$) and i is the inclination of the orbital plane of the system with respect to the observer. Due to the close proximity of both components ($P_{orb} \lesssim 10$ hr), the orbit will be circularised and tidal forces bring the donor star into co-rotation (Tassoul & Tassoul 1992). This is a good approximation for all the systems described in this thesis. We can combine Equation 1.7 with the definition of the centre of mass, $a_{1,2} = M_{2,1}a/(M_1 + M_2)$, as well as Equation 1.2, to obtain the so-called *mass function*:

$$f_{1,2} = \frac{M_{1,2}^3 \sin^3 i}{(M_1 + M_2)^2} = \frac{P_{orb} K_{2,1}^3}{2\pi G} \quad . \tag{1.8}$$

The mass function establishes an absolute minimum to the mass of the compact accretor, in the limit where $i = 90°$ and $M_2 = 0$ and vice-versa for the donor. Obtaining a dynamical estimate (rather than just a limit) on the component masses requires estimates of both K_1 and K_2 (which immediately yields $q = K_1/K_2$) plus an estimate of the system inclination. If an independent estimate of the mass ratio is available (e.g.

from eclipses, superhumps or the method outlined below), only one of the radial velocity amplitudes is needed, of course.

An independent estimate for the mass ratio of the system can be obtained from the fact that the donor is a synchronously rotating Roche-lobe filling object. This unique relationship relates the rotational broadening of the absorption lines of the secondary with the donor's radial velocity (Horne et al. 1986). Since the donor is tidally locked, its projected rotational velocity, $v \sin i$, is given by

$$v \sin i = (K_1 + K_2)\frac{R_2}{a} \quad . \tag{1.9}$$

Since the donor is also filling its Roche-lobe, it is possible to combine Equations 1.9 and the fact that $q = K_1/K_2$ to obtain:

$$\frac{K_2}{v \sin i} = \left[(1+q)\frac{R_L}{a}\right]^{-1} \quad . \tag{1.10}$$

Therefore, the mass ratio can be uniquely determined by measuring $v \sin i$ and K_2 from observations.

1.2.2 Accretion

Accretion onto a compact object is one of the most efficient ways to extract energy from matter. The maximum available accretion luminosity, L_{acc} is given by:

$$L_{acc} = \frac{G\dot{M}M_1}{R_1} \quad , \tag{1.11}$$

where $\dot{M}$ is the mass accretion rate. To first order, this allows us to quantify the output luminosity as a function of the properties of the compact objects. Scaled to typical values for accreting compact binary systems, this yields:

$$\begin{aligned} \text{WD:} \quad L_{acc} &= 4.18 \times 10^{32} \left(\frac{\dot{M}}{10^{-10}}\right)\left(\frac{M_{WD}}{M_\odot}\right)\left(\frac{10^9 \text{cm}}{R_{WD}}\right) \text{ erg s}^{-1} \quad , \\ \text{NS:} \quad L_{acc} &= 4.18 \times 10^{35} \left(\frac{\dot{M}}{10^{-10}}\right)\left(\frac{M_{NS}}{M_\odot}\right)\left(\frac{10^4 \text{cm}}{R_{NS}}\right) \text{ erg s}^{-1} \quad , \end{aligned} \tag{1.12}$$

where $\dot{M}$ is given in units of $\text{M}_\odot$ yr^{-1}. For BHs, however, it is not clear that Equation 1.11 is valid due to a lack of a hard surface. A fraction of the in-falling material will not be able to release its associated kinetic energy before proceeding to fall inside the event horizon, located at the Schwarzschild radius $R_{sh} = 2GM_1/c^2$ (Abramowicz & Fragile 2013), where c is the speed of light. The uncertainty associated to this process

can be parametrised as an efficiency, η, of the L_{acc} given by

$$L_{acc} = \frac{2\eta G\dot{M}M_1}{R_{sh}} = \eta\dot{M}c^2 \quad . \tag{1.13}$$

In the limiting case where all material releases its energy at the event horizon then $\eta = 1$. However, BHs have typical values of $\eta \sim 0.1$.

Equation 1.12 shows that the luminosity depends directly on the mass transfer rate and the nature of the accretor. However, at high luminosities, the rate of the in-falling material (assumed to be fully ionised hydrogen) can be regulated by the same luminosity it generates. The gravitational force experienced by the in-falling material is given by:

$$F_{grav} = \frac{GM_1(m_p + m_e)}{R_1^2} \approx \frac{GM_1(m_p)}{R_1^2} \quad , \tag{1.14}$$

where $m_{p,e}$ is the mass of the proton and electron, respectively. The luminosity generated by the accretion process will impart an outward force, F_{rad}, due to the radiation pressure the photons exert on the accreting material. For an isotropic radiating field, F_{rad} is given by:

$$F_{rad} = \frac{\sigma_T L}{4\pi R^2 c} \tag{1.15}$$

where σ_T is the electron cross-section (Thomson). In the limit where $F_{rad} \simeq F_{grav}$, the accretion onto the compact object can be restricted and even interrupted (if accretion luminosity is the only source). The limiting case where $L_{rad} = L_{grav}$, is known as the Eddington limit (Eddington 1926) and corresponds to a luminosity of

$$L_{edd} = \frac{4\pi G M_1 m_p c}{\sigma_T} \simeq 1.3 \times 10^{38} \frac{M_1}{M_\odot} \text{ erg s}^{-1} \quad . \tag{1.16}$$

This limit is derived assuming fully ionised material, therefore electron scattering dominates the opacity of the flow. However, if the material is neutral or partially ionised, radiation pressure can act on strong resonance lines with radiation pressures up to ~ 2000 times stronger (e.g. line-driven winds, Gayley & Owocki 1994). Therefore, L_{edd} represents the maximum luminosity at which we can expect radiation pressure to stop accretion.

Hence, this also sets an upper limit on the mass accretion rate onto the compact object, $\dot{M}_{edd}$. Neutron star systems can reach $L_{edd} \sim 1.8 \times 10^{38}$ erg s^{-1} (for a canonical NS mass of 1.4 M$_\odot$) with plausible values of mass transfer rates ($\dot{M} \sim 10^{-8}$ M$_\odot$ yr^{-1}), particularly during episodes of high mass transfer. On the other hand, white dwarfs would require extremely high mass transfer rates ($\dot{M} \gtrsim 10^{-4}$ M$_\odot$ yr^{-1}) to achieve these luminosities, so they are typically accreting at highly sub-Eddington rates.

1.2.2.1 Accretion disc

Material that leaves the donor through the L1 point has too much specific angular momentum to fall directly onto the WD. Instead, the gas will quickly settle in a circular Keplerian orbit around the accretor, with the same specific angular momentum it had when it left the L1 point. The distance of this orbit from the accretor is called the *circularisation radius* (Frank et al. 2002), R_{circ}, and is given by

$$\frac{R_{circ}}{a} = \left(\frac{R_L}{a}\right)^4 (1+q) \quad . \tag{1.17}$$

As material accumulates near R_{circ}, dissipative processes (such as friction and shocks) will transform some of the kinetic energy of the gas into heat, which is eventually radiated away. This loss of energy causes most of the material to move inwards, with its angular momentum being taken up by a small fraction of the material that moves outwards. This drift of material towards the compact accretor is much longer than the timescale in which radiative cooling can lose the energy. Therefore, the material will lose as much energy as possible for its angular momentum, settling into a minimal energy configuration, a circular orbit with a Keplerian velocity, v_K, given by

$$v_K = \sqrt{\frac{GM_1}{r}} \quad . \tag{1.18}$$

Thus, the material will slowly drift in concentric circular orbits towards the primary, in what is known as an *accretion disc*.

The simplest accretion disc is one that is optically thick and geometrically thin (Shakura & Sunyaev 1973; Frank et al. 2002). The structure of such a disc depends on the assumptions on the internal viscosity of the plasma, ν of the accreting material. The viscosity, due to the conditions of the gas (molecular viscosity) expected in accretion discs, is far too small to drive the viscous dissipation and angular momentum transport. However, there are reasons to expect the flow to be in a turbulent state which may change the viscous properties of the disc. It is possible to describe viscosity as a function of a characteristic speed and length i.e. the turnover velocity and the size of the turbulent eddies. In an accretion disc, the maximum possible values for these two scales are the local sound speed, c_s, and the disc thickness, H. Thus, ν is given by:

$$\nu = \alpha c_s H \quad , \tag{1.19}$$

where we would expect $\alpha \lesssim 1$, and is known as the *α-prescription* (Shakura & Sunyaev 1973). Observationally, typical values can range from $\alpha \simeq 0.02 - 0.1$, depending on the local plasma conditions.

For an optically thick disk, every annulus of gas is assumed to emit as a blackbody. Therefore, the effective temperature distribution as a function of radius, $T(R)$, can be shown to be independent of α (Pringle 1981), and is given by

$$T(R) = \left\{ \frac{3GM_1\dot{M}}{8\pi R^3\sigma} \left[1 - \left(\frac{R_1}{R} \right)^{1/2} \right] \right\}^{1/4} \quad , \tag{1.20}$$

where σ is the Stefan-Boltzmann constant. Therefore, we can estimate the luminosity emitted by the disc, L_{disc} by integrating over both sides of the disc, so

$$L_{disc} = 2\int_{R_{min}}^{R_{max}} 2\pi R T(R) dR = \frac{GM_1\dot{M}}{2R_{min}} = \frac{Lacc}{2} \quad , \tag{1.21}$$

while the other half of L_{acc} is released at the surface of the compact accretor in the form of a *boundary layer* (see Section 1.2.2.3).

The spectral energy distribution (SED) of the disc can be calculated if we approximate that every ring of material emits as a blackbody with an effective temperature given by Equation 1.20. Therefore, the overall SED of the disc is the superposition of the emission from all rings, as shown in Figure 1.4. Thus, the monochromatic flux, F_ν, emitted by the disc is given by (Frank et al. 2002)

$$F_\nu = \frac{4\pi h\nu \cos i}{c^2 D^2} \int_{R_{min}}^{R_{max}} \frac{R dR}{e^{h\nu/kT(R)}} \quad , \tag{1.22}$$

where h is the Planck constant, D the distance of the system, R_{max} and R_{min} the minimum and maximum radii of the disc, respectively. The spectrum will deviate from a blackbody, forming a plateau made from the peaks of all the superimposed blackbodies, following a power-law $F_\lambda \propto \lambda^{-7/3}$. This plateau, however, only forms when the disc is sufficiently large, typically for $R_{out}/R_{in} \gtrsim 100$. Furthermore, this spectrum is idealised since it does not account for the atmosphere of the disc itself, which could lead to significant flux discrepancies in the detailed calculation of the spectrum.

1.2.2.2 Outbursts

Many accreting systems undergo outbursts, where the brightness of the system can increase by several orders of magnitude. Among accreting white dwarfs, systems belonging to the dwarf nova sub-class exhibit regular outbursts that span between 2-8 mag at optical wavelengths (e.g. Coppejans et al. 2016). Arguably the best interpretation of this behaviour is provided by the disc instability model (DIM) (Smak 1971; Osaki 1974; Lasota 2001; for a recent review).

The plasma in the disc is thermally stable as long as the local cooling rate (Q_-) can match the local heating (Q_+). This local thermal equilibrium is shown schematically

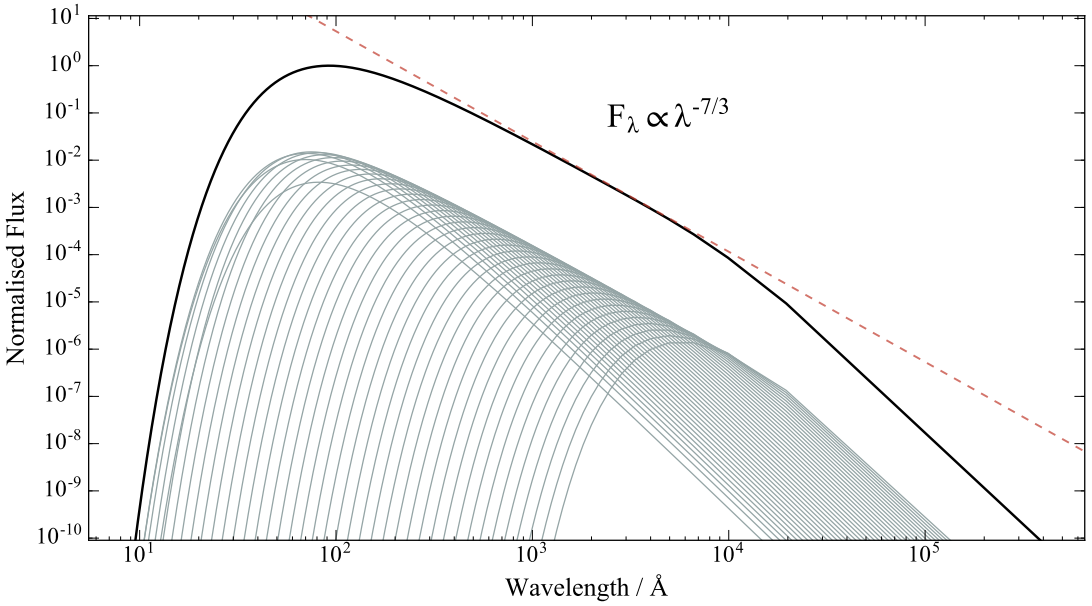

FIGURE 1.4: Spectrum of a steady-state accretion disc for $R_{out}/R_{in} = 100$. Each individual ring of matter (gray lines) contributes to the emission of the overall spectrum (dashed blue line). A power-law with spectral index of $-7/3$ is shown as a reference for the plateau.

in the $\Sigma - T_{eff}$ diagram in Figure 1.5 as the black solid line, where Σ is the surface density and T_{eff} the effective temperature. In the event of any perturbations, e.g. a local increase of Σ, the gas will try to restore thermal equilibrium by moving along the curve, therefore increasing the local T_{eff}. This condition of thermal equilibrium is valid because the radiative cooling timescale is much shorter than the viscous heating timescale (produced by the increase in Σ). The gas will cope with any changes as long as $Q_- > Q_+$. This condition is met in two stable configurations in the $\Sigma - T_{eff}$ plane, where

$$\frac{dT_{eff}}{d\Sigma} > 0 \quad . \tag{1.23}$$

Under certain conditions, perturbations in the disc lead the plasma to move between these stable configurations, leading to a loop in this plane - a *limit cycle*.

As the material from the companion accumulates in the disc, it will increase the local Σ (and therefore T_{eff} to maintain thermal equilibrium) until it reaches a critical surface density, Σ_{max}. The disc, mainly composed of hydrogen, will be partially ionised and in certain regions close to its ionisation temperature $\sim$ 6500 K. Any local changes in the temperature or density of the plasma can around this critical value trigger a sudden ionisation transition between these two states (Smak 1971). At this point, the material will try to move along the thermal equilibrium curve, reaching the unstable region, where $Q_- < Q_+$. Since the change in T_{eff} is much faster than in Σ, the system will move in T_{eff} (in a $\sim$ vertical line) until it reaches thermal equilibrium. Therefore, this thermal instability is triggered and the material will settle in a stable configuration

in the upper branch. Since the Σ remains almost constant, Q_- is efficient enough to bring thermal equilibrium which the gas responds by lowering its density, moving the downwards the stable solution. This process will continue (since in the upper branch $Q_- > Q_+$) until the surface density reaches a critical Σ_{min}, quickly returning the disc to the lower branch of the $\Sigma - T_{eff}$, in a similar way as the transition described earlier. This limit cycle process is considered locally at any given radius of the disc. However, in order for the DIM to work it needs to be a global process. The assumption in the model is that this instability can trigger a runaway process and propagate (as a "burning front") through the disc dissipating energy and mass. As the front moves, the material quickly drops below Σ_{min} and returns back to a quiescent disc. In order to guarantee that the local state changes turn into global ones, DIM calculations need to assume that α is lower in the low state ($\alpha_{cool} \sim 0.02$) than in the high state ($\alpha_{cool} \sim 0.1$) (Lasota 2001). The recurrence time between outbursts will be $\propto P_{orb}$ from Equation 1.2, since

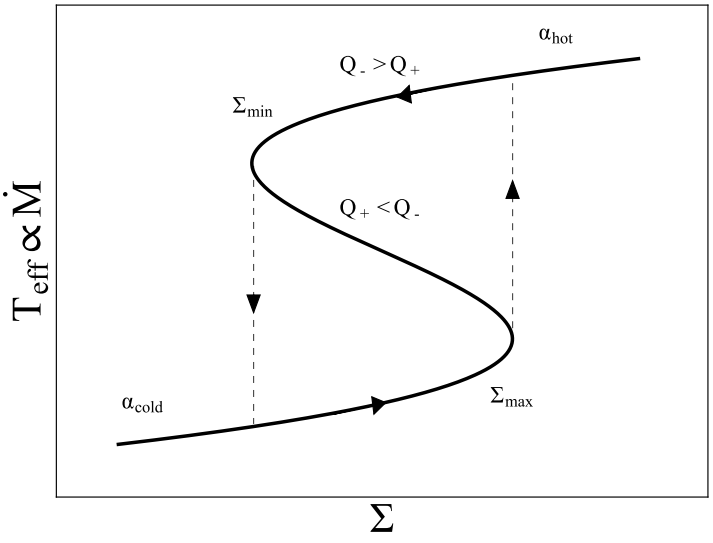

FIGURE 1.5: The surface density, Σ and effective temperature, T_{eff} schematic of the disk instability model. The arrows point the direction of the local conditions in the disc during an outburst.

at each P_{orb} one could accommodate a larger accretion disc and therefore will require a longer time to build up enough mass to trigger the thermal instability. This trend is observationally observed in the population of dwarf novae due to recent long-cadence surveys such as the Catalina Real-Time Survey (Breedt et al. 2014; Coppejans et al. 2016; Otulakowska-Hypka et al. 2016).

1.2.2.3 Boundary layer

The material carried inwards by the accretion disc will eventually reach the compact object, releasing $1/2L_{acc}$ which is stored in the kinetic energy of its Keplerian rotation.

In some cases, a WD or NS can be magnetised enough that matter will be channelled towards the poles via strong magnetic fields. I consider this scenario in Section 1.4.2.1. However, most accreting white dwarfs possess low magnetic field strengths ($B_{WD} < 10^6$ G), and the accretion flow will remain undisturbed by the field lines (since the gas pressure is greater than the magnetic pressure). Therefore, the material will have to slow down from its Keplerian value to match the rotation of the compact object or be ejected. This region is known as the boundary layer. The spectral energy distribution of the boundary layer will vary depending on the local properties of the gas. If the boundary layer is optically thick, the bulk of the energy will emit close to blackbody radiation with characteristic temperatures high enough to emit in the extreme-ultraviolet or soft X-rays; on the contrary, if it is optically thin, the radiation will be produced as thermal bremsstrahlung primarily in hard X-rays (Frank et al. 2002).

1.2.2.4 Nova eruption

The accreted material that reaches the WD surface will compress and increase the temperature ($T \sim 10^8$ K) of the outer layers. The accumulation of material can eventually trigger H-burning in the envelope of the WD. The stability of the H-burning material, however, is dependent on the $\dot{M}$, M_1 and the composition of the accreting material (Shen & Bildsten 2009). A combination of these conditions can lead to two main scenarios: *steady H-burning* (observed as super-soft X-ray sources, *SSS*, Kahabka 2002) or a thermonuclear runaway explosion, the so-called *nova eruptions* (e.g. Truran 2002). A SSS can achieve a steady H-burning layer as long as $\dot{M} \approx (1-4) \times 10^{-7}$ M$_\odot$ yr^{-1} for $M_1 = 0.7 - 1.4$ M$_\odot$, achieving luminosities of $10^{36} - 10^{38}$ erg s^{-1}. For lower $\dot{M}$, only a fraction of the accreted material will ignite (Truran 2002). The WD outer layers quickly expand (> 100 R$_\odot$) and a large part of the envelope is ejected as a wind (Hachisu & Kato 2006). This mechanism accounts for the observed properties in the light curves of nova explosions, characterised by quick exponential rise and a power-law decay back to quiescence.

1.3 Accreting White Dwarfs

Interacting binaries where a low–mass star fills its Roche lobe and transfers mass onto a white dwarf are often referred to as *cataclysmic variables* (hereafter CVs, see reviews by Warner 1995; Hellier 2001). These systems have been observed and classified for over a century due to their intrinsic brightness and variability and their frequent outbursts. Nevertheless, their binary nature was independently proposed only decades later by Smak (1971) and Warner & Nather (1971). In this section, I will provide an overview of the characteristics of the two main components in CVs and review the theory of their evolution.

White Dwarfs

The primary component in CVs is formed from the core of the initially more massive star in the binary system. Typically this is a carbon/oxygen WD with a thin hydrogen atmosphere. Systematic studies of WD masses in CVs have found a significantly larger average mass, $\langle M_{WD} \rangle \simeq 0.8$ M$_\odot$ (Knigge 2006; Zorotovic et al. 2011), when compared to isolated WDs, $\langle M_{WD} \rangle \simeq 0.659 \pm 0.003$ M$_\odot$ (Kepler et al. 2015). This apparent mass gain during the CV phase might provide evidence for the relevance of CVs as type Ia supernova progenitors (Yungelson & Livio 1998). Measurements of WD masses in post-common envelope systems, pre-CVs and CVs have found an increasing trend (Savoury et al. 2011) as well as being supported by detailed calculations of ejecta masses during nova eruptions (Newsham et al. 2014). In contrast, heavy elements have been observed in nova ejecta suggesting mixing of elements coming from the WD core and interpreted as evidence for erosion (Hachisu & Kato 2006). Additionally, evidence for erosion in systems like T Pyx, where the ejecta mass is higher than the accreted material between nova events (Patterson et al. 2016).

The high conductivity associated with electron degeneracy means that WD interiors are isothermal. This internal thermal energy reservoir is trapped inside the gaseous atmosphere (which acts as a thermal shield) and lies on top of the degenerate core. Therefore, the cooling of the WD occurs slowly, regulated by its luminosity (Fontaine et al. 2001; Camenzind 2007). However, in an interacting binary, the continuous accretion onto the WD will heat its outer layers, increasing the effective temperature, T$_{\rm eff}$. Consequently, the WD temperature can provide us with an estimate of the system's mass transfer rate (Townsley & Bildsten 2003; Townsley & Gänsicke 2009; Pala et al. 2015). These estimates are usually done for systems in quiescence, where the light from the WD is less contaminated by the bright optical and UV disc by fitting synthetic atmosphere spectra and where it might reflect the long-term average $\dot{M}$. This important measurement allows us to probe directly the evolutionary state of a given system and consequently test its angular momentum loss.

Donor stars

The donors in CVs are low-mass stars (≤ 1 M$_\odot$) ranging from spectral type G to L/T (5,000−2,000 K). They are subject to a continuous mass loss that essentially drives the donor down the main-sequence throughout the evolution of the system. As a result, the donor is pushed slightly out of thermal equilibrium and therefore slightly oversized for its mass. Early on, observations revealed inconsistencies between their radius and that of their main-sequence analogues (Echevarria 1983; Knigge 2006; Littlefair et al. 2008). The degree of bloating of the donor can then be used as an evolutionary tracer of the system i.e. a measurement of the mass transfer, $\dot{M}_2$ (Knigge et al. 2011). Therefore, proper characterisations of the donor can allow us to test the secular evolution of CVs.

Moreover, the synchronisation of their spin with the binary orbit means that these stars are rapid rotators. This modifies the star's internal structure which, in turn, can affect the magnetic activity near the surface (Smith 1979; Mohanty & Basri 2003) and lead to increased atmospheric circulation (as observed in brown dwarfs, Showman & Kaspi 2013). Indeed, Roche tomography has allowed us to observe star spots on the surface of donors in a few bright systems (e.g. Watson et al. 2007). In addition, the donor is exposed to irradiation by the hot WD and accretion disc, which might further enhance the degree of bloating.

Despite their importance, accurate characterisation of CV donors has been challenging. The main problem arises in the identification of atmospheric features associated with the donor against the much brighter WD and accretion disc. In addition, the lower surface temperature pushes the donor's blackbody peak towards longer optical wavelengths ($>$ 7,000 Å) and into the near-infrared (NIR, $1 - 2.5$ μm).

1.3.1 Secular Evolution

The observed orbital period distribution of CVs, shown in 1.6 , shows three key features: a) a bimodality due to a lack of systems between $\sim 2-3$ hr, the so-called *period gap*; b) a strong cut-off at $P_{orb} \lesssim 80$ min, known as the *period minimum*; c) a lack of systems at orbital periods $\gtrsim$ 12 hr. Theoretical models of CVs have been broadly successful in explaining these via the so-called *standard model*. However, it has become clear in the past decade that there are several significant shortcomings of the standard model in explaining the overall population of CVs (e.g., Knigge 2011b). In the following sections,

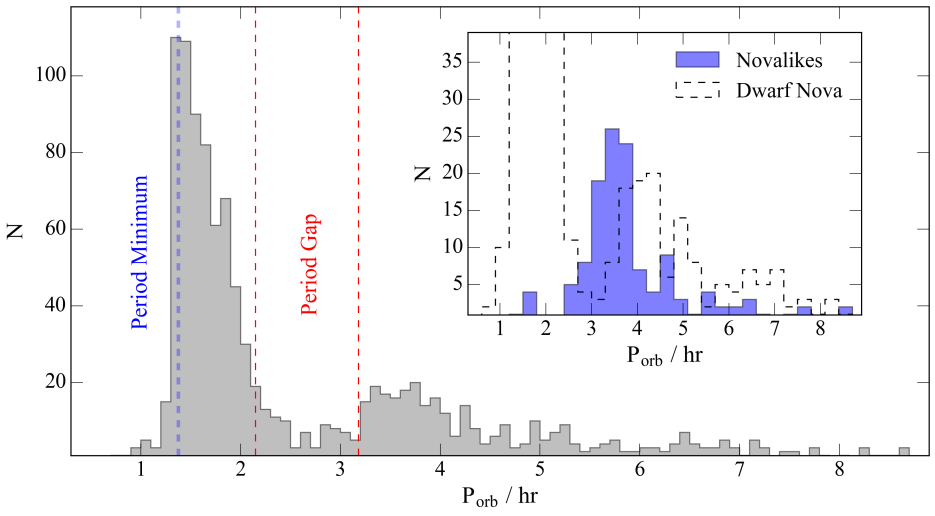

FIGURE 1.6: Orbital period distribution of CVs taken from Ritter & Kolb (2003) Catalogue v23. The period gap is estimated to be between 2.15-3.18 hr (red lines) and the period minimum (blue line) around 82.4±0.7 min (Knigge et al. 2011). Inset shows the distribution of dwarf novae and nova-likes.

I will describe the standard model and the current observational status of the field.

1.3.1.1 The standard model for CV evolution

Accreting compact binaries where RLOF occurs requires that $R_2 = R_L$. In order to achieve this equality, either R_2 has to increase, or R_L has to decrease. In systems such as CVs and LMXBs, the donors are mostly main sequence stars so their radii will not expand unlike evolved stars, where their radius increases on their nuclear timescale, τ_{nuc}[1]. So, to even initiate and then sustain mass transfer, the R_L needs to shrink down to the donor surface. In order to assess the requirements for a shrinking R_L, lets consider the total angular momentum of the system, J, given by

$$J = M_1 M_2 \left(\frac{Ga}{M_T}\right)^{1/2}, \tag{1.24}$$

where $M_T = M_1 + M_2$. Therefore, the rate of change of angular momentum, $\dot{J}$, is obtained by logarithmically differentiating Equation 1.24 to obtain

$$\frac{\dot{J}}{J} = \frac{\dot{M}_1}{M_1} + \frac{\dot{M}_2}{M_2} + \frac{1}{2}\frac{\dot{a}}{a} - \frac{1}{2}\frac{\dot{M}_T}{M_T}. \tag{1.25}$$

In a conservative mass transfer scenario, where all the mass lost by the donor ($\dot{M}_2 < 0$) is accreted by the primary i.e. $\dot{M}_T = \dot{M}_1 + \dot{M}_2 = 0$), we can calculate the rate of change of the donor's radius by combining Equations 1.4 and 1.25:

$$\frac{\dot{R}_L}{R_L} = \frac{2\dot{J}}{J} - \frac{2\dot{M}_2}{M_2}\left(\frac{5}{6} - q\right). \tag{1.26}$$

Since most CVs and LMXBs have $q < 5/6$, then we require a mechanism for angular momentum loss (AML), $\dot{J} < 0$ to maintain mass transfer from the donor i.e. to be able to contract the radius of the star to match its Roche-lobe radius (e.g. see Paczynski 1976; King 1988).

The systemic loss of angular momentum, $\dot{J}$, is provided by two main mechanisms. The first, is due to gravitational wave radiation (GR, Landau & Lifshitz 1971):

$$\dot{J}_{GR} = -\frac{32}{5}\frac{G^{7/2}}{c^5}\frac{M_1^2 M_2^2 M_T^{1/2}}{a^{7/2}}, \tag{1.27}$$

which acts throughout the full evolution of the system. GR is an efficient AML mechanism only at small orbital separations. However, early measurements of mass transfer rates at longer $P_{orb} \gtrsim 3$ hr suggest values exceeding those generated by GR alone (e.g.

[1] Time scale on which the star will exhaust its supply of nuclear fuel if it keeps burning it at the current rate. For a main sequence star, the fusion of hydrogen into helium will exhaust its reservoir in $\tau_{nuc} = \frac{0.007 M_\odot c^2}{L_\odot} \approx 10^{11}$ yr

Patterson 1984). Thus, an extra AML mechanism was required. The most accepted candidate is the *magnetic braking* mechanism of the donor star.

Low-mass stars drive an ionised wind that co-rotates with the magnetic field lines up to the Alfvén radius, where the gas ram and magnetic field pressures become roughly equal. This out-flowing material exerts a spin-down torque that gradually slows down the star. Since the donor is forced to rotate synchronously with the binary orbit, the net effect is the removal of angular momentum from the system. The true nature of the dynamo that generates this magnetic field, and hence the strength of the spin-down, remains uncertain (e.g. Wright & Drake 2016). In binary evolution calculations, empirically-motivated prescriptions are typically used, such as the parametrisation developed by Verbunt & Zwaan (1981) and Rappaport et al. (1983):

$$\dot{J}_{MB} = -5 \times 10^{-29} k_2 f^{-2} M_2 R_2^4 \Omega_{orb}^3 \left(\frac{R_2}{R_\odot} \right)^{\gamma-4} \quad , \tag{1.28}$$

where $k_2 \simeq 0.1$ for low-mass stars, $f \simeq 1.78$, as calibrated from observations of G-type stars (Skumanich 1972; Smith 1979) and typical values for the power-law index, γ, are between 3-4. Thus, the total AML is then given by:

$$\dot{J} = \dot{J}_{GR} + \dot{J}_{MB}. \tag{1.29}$$

This simple picture allows us to trace and explain the main features of CV evolution. We can divide it into five main stages or populations: pre-CVs, long-period CVs, the period gap, short-period CVs and period bouncers.

1.3.1.2 Pre-CVs

In order for a MS-MS binary to become a CV, a combination of initial orbital properties are required (Goliasch & Nelson 2015; Nelemans et al. 2016). First, the initial binary separation must not be so large that the more massive star will never fill its Roche lobe. Second, if the orbital separation is too small, a merger inevitably will take place after the primary fills its Roche lobe. Finally, the separation must be large enough to allow for a WD core to form before the onset of mass transfer. If these conditions are satisfied, the more massive star in the system (which will eventually become the WD) will eventually fill its Roche lobe and initiate mass transfer as it evolves up the red-giant branch (RGB) or asymptotic giant branch (AGB). At this point, a combination of enhanced mass transfer (due to stellar winds from the evolved donor or pulsation instabilities) can lead to an unstable RLOF (Ivanova et al. 2013). This process is dynamically unstable and will thus proceed on a dynamical timescale, $\tau_{dyn} \sim \sqrt{R^3 (GM)^{-1}}$. This runaway process will engulf the secondary star in the atmosphere of the red giant star. The resulting very important and short-lived phase is known as the *common envelope phase* (Paczynski 1976; Ivanova et al. 2013; for a recent review). The frictional energy produced as the

secondary star orbits inside the envelope of the primary will lead to either the removal of the envelope or the merger of both stars (Nelemans et al. 2016). As the envelope leaves the system, it will carry away a lot of angular momentum, which in turn, will shrink the orbit. In this picture, a WD+main sequence binary will be formed with orbital periods of $\lesssim 1$ d, e.g Zorotovic et al. (2011). These systems are called post-common-envelope binaries (PCEBs), and include the population of future CVs, the so-called pre-CVs.

1.3.1.3 Long-period CVs and the period gap

PCEBs will continue to shorten their orbit through the removal of angular momentum due to GR and magnetic braking. Eventually, the R_L catches up with the stellar radius, initiating a second phase of RLOF. As mass transfer proceeds, the donor loses mass in a timescale defined by $\tau_{\dot{M}_2} \simeq M_2/\dot{M}_2$. The donor will respond to the mass loss by contracting in order to achieve thermal equilibrium in a thermal timescale, $\tau_{KH} = GM_2^2/R_2L_2$. In CVs, however, we have the situation where $\tau_{KH} \sim \tau_{\dot{M}_2}$. As the donor evolves down the evolution track, its radius shrinks just not as quick as to maintain a main-sequence equilibrium radius. Therefore, donors are slightly bloated in comparison to an isolated main-sequence star of the same mass (Knigge 2006).

The donor, however, adjusts its radius in response to mass loss in a timescale $\tau_{adj} \simeq 0.05\tau_{KH}$ (Stehle et al. 1996). Thus, this property allows the systems to quickly converge in a roughly unique track despite the varied initial conditions in a pre-CV phase. As a consequence, donors follow a tight mass–radius relationship, providing a unique measurement of $\dot{M}_2$ and hence the AML at any given point in the evolutionary track (Knigge 2006; Knigge et al. 2011).

As already mentioned, the distribution of CVs as a function of orbital period shows a distinct lack of systems between 2-3 hr, commonly referred as the period gap (Robinson et al. 1981), shown in Figure 1.6. Rappaport et al. (1983) proposed that the upper edge of the period gap was associated with a sudden drop of lAML, due to a disruption of the magnetic braking mechanism. The mass of the donors around ~ 3 hr corresponds roughly to the transition where the star becomes fully convective ($M_2 \sim 0.35$ $M_\odot$for isolated stars and $M_2 \sim 0.2 - 0.3$ $M_\odot$for mass-losing donors, Chabrier & Baraffe 1997; Knigge et al. 2011; respectively). It is thought that the dynamo that generates the magnetic field originates in the interface between the radiative core and the convective envelope (known as the tachocline). As this interface disappears, the magnetic braking mechanism is suddenly suppressed (Reiners & Basri 2007). The sudden drop in AML causes the bloated donor to relax closer to its main-sequence radius, thus ceasing mass transfer. Observational evidence for this discontinuity in the AML of the system has been observed independently by constructing the $M - R$ relationship of CV donors (Patterson 1984; Knigge 2006) and in young open clusters e.g. the Hyades (Douglas et al. 2014). Therefore, any binary will be observed crossing the period gap as detached

white dwarf+main sequence binaries (with spectral type in the range M4-M6, Zorotovic et al. 2016). Eventually, the orbit will shrink enough to allow the Roche lobe to catch up with the donor radius again, enabling the onset of mass transfer. Hence, the system re-appears as a CV at ~ 2 hr, with the donor at its equilibrium (main-sequence) radius. In fact, it can be shown that the size of the gap depends on the degree of bloating of the donor above the gap. Since $M_2 \propto R_L^3 P_{orb}^{-2}$ from Equation 1.6, we can obtain the ratio of radius R_+/R_- at a constant M_2:

$$\frac{R_+}{R_-} = \left(\frac{P_{orb,-}}{P_{orb,+}}\right)^{-2/3} = \left(\frac{2.15 \pm 0.03}{3.18 \pm 0.04}\right)^{-2/3} \simeq 1.3 \tag{1.30}$$

where $+$ and $-$ represent the values above and below the period gap, respectively. The values of the gap locations were taken from Knigge (2006). Therefore, by finding the edges of the gap in orbital period space, it can be shown that donors just above the gap are $\sim 30\%$ larger than a main sequence star of the same mass (Knigge 2006).

1.3.1.4 Short-period CVs and the period minimum

In the standard model, systems below the period gap will continue to evolve mainly through gravitational wave radiation, at a significantly slower rate than above the period gap (due to the cessation of magnetic braking). The rate of change of P_{orb} can be related to the donor mass transfer rate by logarithmically differentiating Equation 1.6:

$$\frac{\dot{P}_{\rm orb}}{P_{\rm orb}} = \frac{3\zeta - 1}{2}\frac{\dot{M}_2}{M_2} \tag{1.31}$$

where ζ is the mass-radius index of the donor along the CV evolution track ($\dot{M}_2/M_2 = \zeta^{-1}\dot{R}_2/R_2$). This explicit dependence on the internal structure of the donor (through ζ) allows us to track the system response at shorter orbital periods. For any value of $\zeta > 1/3$, the system will evolve towards shorter orbital periods.

Initially, the donor remains close to thermal equilibrium once it emerges from below the period, i.e. $\zeta = 0.88$ (Chen & Kipping 2016). However, as evolution progresses to shorter periods, the $\tau_{\dot{M}_2}$ increases more slowly than τ_{KH} so the donor becomes more and more bloated, i.e. ζ decreases. In fact, eventually mass transfer must push the mass of the donor below the H-burning limit ($\sim$0.072 $M_\odot$, Chabrier & Baraffe 1997).. Since there is no generation of internal energy in this regime, sub-stellar objects are never in thermal equilibrium and have $\zeta \lesssim 0$ (Chabrier et al. 2009; observationally constrained to $\zeta \simeq -0.044$, Chen et al. 2016). Somewhere during this transition (which happens close to the sub-stellar regime), the donor must cross the critical value of $\zeta < 1/3$. This implies a reversal of the system towards longer orbital periods.

Observationally, this leads to two clear predictions for the distribution of CVs shown in Figure 1.6. First, there must exist a sharp cut-off at short orbital periods, known

as the *period minimum*, $P_{\rm min}$. Second, as systems approach this period minimum the intrinsically long timescale to evolve through it will accumulate systems around it (as $\zeta \rightarrow 1/3$ then $\dot{P}_{orb} \rightarrow 0$).

The existence of this *period minimum spike* was, for a long time, a great discrepancy between theory and observations. However, the era of large synoptic surveys, such as the Sloan Digital Sky Survey (SDSS, York et al. 2000) aided the community to dramatically increase the number of characterised systems from 472 (v7.0) up to $\sim$ 1600 (v7.23 in 2016) in just over a decade (Ritter & Kolb 2003), with at least a comparable number of candidate systems awaiting classification (Breedt et al. 2014). This, in turn, revealed the existence of the accumulation of short orbital period systems (Gänsicke et al. 2009), as seen in Figure 1.6.

1.3.1.5 Period Bouncers

Systems that evolve past the period minimum will experience an increase in orbital period; these systems are commonly known as *period bouncers*. As with systems emerging from the bottom edge of the period gap, the evolution of period bouncers is thought to be mainly driven by gravitational wave radiation. The low mass transfer rate in these systems ($\dot{M} \lesssim 10^{-11}$ M$_\odot$ yr^{-1}), induced by the slow AML naturally produces long-lived systems with evolutionary timescales $\tau = J/\dot{J}_{GR} \gtrsim 2$ Gyr. Theoretical estimates thus predict the predominance ($\sim$ 70%) of period bouncers over the entire CV population (Kolb & de Kool 1993; Howell et al. 1997). Observationally, however, the intrinsically low luminosity of these systems and their long outburst recurrence times (given the low $\dot{M}$) provide natural conditions for surveys to have missed them entirely (Breedt et al. 2014). Nevertheless, deeper and larger synoptic surveys, combined with spectroscopic and photometric follow-up have produced a few short-P_{orb} systems that are strong candidates for harbouring sub-stellar donors (Littlefair et al. 2008; Aviles et al. 2010; Patterson 2011; Kato & Osaki 2013), as shown in Figure 1.7. However, the number of systems observed as period bouncers still seems to be lower than predicted by the standard model of CV evolution, even when accounting for selection effects (Pretorius et al. 2007).

1.3.2 Discrepancies

Despite the success of the standard model in accounting for the broad properties of the orbital period distribution of CVs, many open problems remain. One of the main uncertainties in the evolution of CVs is the strength of AML due to magnetic braking (Knigge et al. 2011; Schreiber et al. 2016). Semi-empirical models suggest that, in order to reproduce the observed distribution of CVs, it is required to decrease the AML for low-mass stars relative to the widely used prescription, RVJ83, by Verbunt & Zwaan

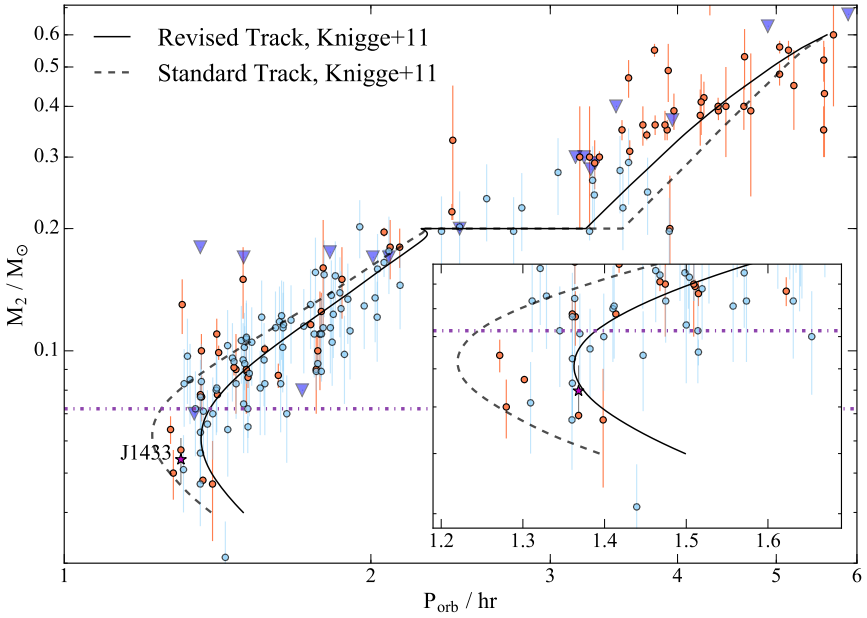

FIGURE 1.7: Donor mass as a function of orbital period in CVs. Measurements for the mass (circles) and upper limits (triangles) are shown, taken from the Ritter & Kolb (2003) Catalogue v23. Masses estimated via superhumps are shown in green (Knigge 2006). The CV presented in this thesis, SDSS J1433+1011 and its new mass estimate is shown as a star. The hydrogen burning limit ($M_H = 0.072$ M$_\odot$), is shown as the dotted line. Inset shows a zoom into the period minimum and period bouncer region.

(1981); Rappaport et al. (1983). Despite the convenient parametrisation, this treatment of magnetic braking is neither unique nor fully applicable across the whole range of masses all the way down to sub-stellar objects (for a compendium of magnetic braking recipes, see Appendix A in Knigge et al. 2011).

In Figure 1.8, I show a rough comparison of various magnetic braking laws from the literature, as implemented in the evolution of a CV. The main point to take from this figure is the wide range of AML strengths between all these physically motivated recipes. In reality, observations of CVs argue in favour of a law similar to RVJ83 in order to reproduce the CV track. However, the most recent calibration for magnetic braking in low-mass stars (Matt et al. 2015) predicts ~ 2 orders of magnitude lower AML than is required to fit the CV track. This highlights a fundamental flaw in our understanding (and hence interpretation) of magnetic braking and CV evolution. In addition, below the period gap the amount of AML required has been found to be ~ 2.6 higher than pure GR (Knigge et al. 2011). In fact, it has been shown that fully convective M-dwarfs display significant magnetic activity in the form of flares (Hilton 2011), and the same is true for brown dwarfs in the form of auroral activity (Hallinan et al. 2015). More recently, evidence of fully convective stars displaying solar-type activity might invalidate the theory of a dynamo generated at the tachocline entirely (Wright & Drake 2016).

Besides the lack of period bouncer systems relative to the overall population, binary

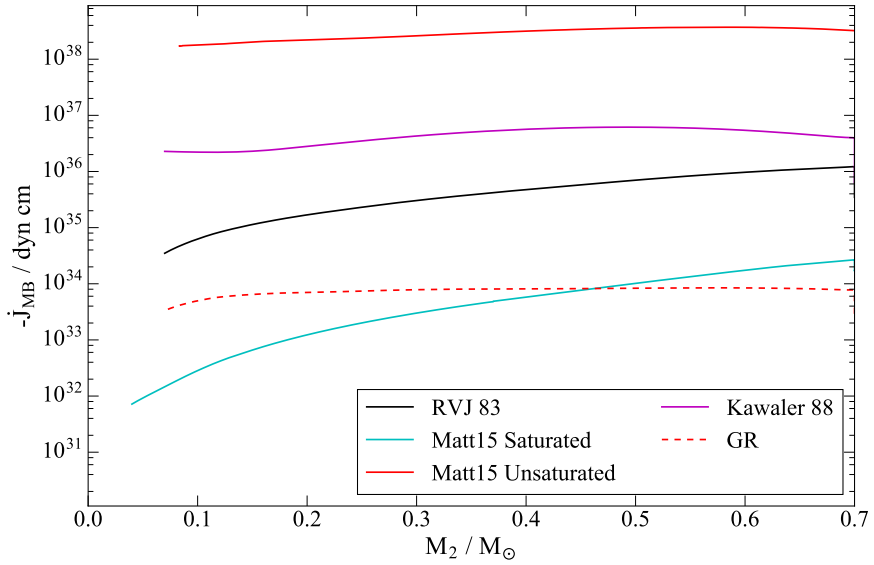

FIGURE 1.8: Comparison of magnetic braking recipes in the literature. I have used the stellar evolution code MESA (Paxton et al. 2011) to evolve a CV with different magnetic braking laws: RVJ83 - (Rappaport et al. 1983), Kawaler88 - (Kawaler 1988) and both saturated and unsaturated laws from MATT15, Matt et al. (2015). The AML from gravitational radiation – GR – is shown for comparison.

population synthesis also predicts a higher number of systems in the Galaxy than observed. In particular, problems arise when studying the present-day CV population. However, the models are strongly dependent on the birth rate of primordial systems (linked to the star formation history of the Galaxy, in most cases assumed as constant), the efficiency of the common envelope phase (still largely unknown), and the AML mechanisms that drives the evolution of the CV phase. Theoretical estimates for the mid-plane space density, $\rho_0 \sim 10^{-5} - 3 \times 10^{-4}$ pc^{-3} (de Kool 1992; Kolb 1993; Politano 1996), are typically an order of magnitude higher than values given by observational studies, $\rho_0 \sim 4 \times 10^{-7} - 5 \times 10^{-5}$ pc^{-3} (Hertz et al. 1990; Shara et al. 1993; Patterson 1998; Warner 2001; Cieslinski et al. 2003; Schreiber & Gänsicke 2003; Pretorius & Knigge 2012). On the other hand, selection biases and incompleteness of the samples may hinder our ability to locate the missing population observationally (Pretorius et al. 2007). Recent detailed binary population synthesis studies suggest, however, space densities closer to observational values (Goliasch & Nelson 2015). Despite this progress, the distribution of WD masses in CVs ($\langle M_{WD} \rangle \simeq 0.8$ M$_\odot$ (Zorotovic et al. 2011)), with virtually no candidates for low-mass He WDs) remains in direct contradiction to population synthesis model predictions (e.g. Goliasch & Nelson 2015).

1.4 Accreting Millisecond Pulsars

A neutron star (NS) is the compact remnant of a massive star ($M_\star = 6 - 20$ $M_\odot$) after a core-collapse supernova (Janka et al. 2001; Woosley & Janka 2005; Camenzind 2007; Lorimer 2008). The violent explosion leaves behind a very fast rotating compact object, with radius $R_{NS} = 8 - 14$ km and mass $M_{NS} = 1.2 - 2.4$ $M_\odot$. NSs were serendipitously discovered as bright and fast radio pulsars (Hewish et al. 1968), despite being first theorised by Baade & Zwicky (1934) three decades earlier. Since then, NSs have become one of the most active research areas in astrophysics. They are incredible laboratories for studying extreme physical regimes of high densities and strong gravitational fields. So far, we know of over 2000 NSs, mainly from radio and X-ray observations.

The diversity of NSs is as wide as they are numerous. They are found isolated in the Galaxy as rotation-powered pulsars, or X-ray sources, but also in binary systems. Many of them show a misalignment between the magnetic and rotation axis which produces coherent pulses in their radio emission whenever the light beam crosses our line of sight (as exemplified in Figure 1.9). In many cases, they are part of interacting binary systems where X-ray pulsations are produced by matter channelling onto the magnetic poles (Patruno & Watts 2012). These systems can undergo energetic outbursts, being discovered every year as high-energy transients. These accretion-powered NSs can be extremely bright, achieving luminosities of $L_X \sim 10^{38}$ erg s^{-1}, close to the Eddington limit (e.g. Yan & Yu 2015) and in extreme cases, observed as super-Eddington sources (e.g. eltra-luminous X-ray sources, Bachetti et al. 2014).

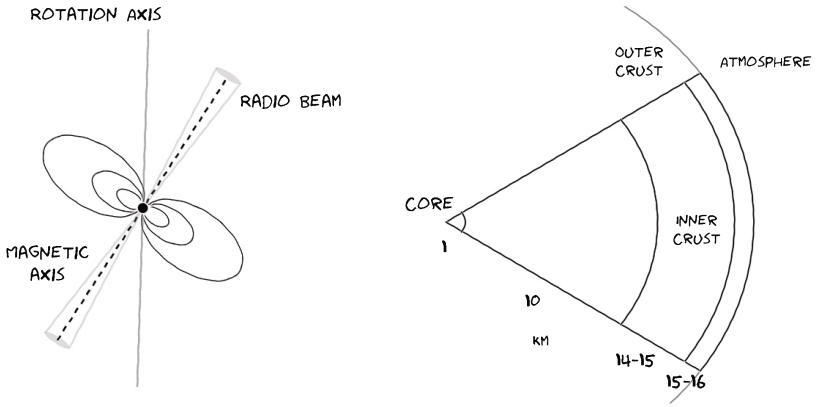

FIGURE 1.9: Schematic of the magnetosphere (left) and cross-section (right) of a rotating neutron star.

Accretion onto the pulsar is thought to be responsible for the large population of fast-spinning NSs, known as millisecond pulsars (MSPs). This was motivated by the discovery of MSPs as rotation-powered NSs in binary systems (Fruchter et al. 1988b) as well as accretion-powered NSs in LMXBs (e.g. SAX J1808.4-3658, Wijnands & van der Klis

1998). Below, I will review the formation and evolution of rotation- and accretion-powered NSs in more detail. Also, I will examine the connection between these two regimes in the context of the recently discovered *missing link* systems.

1.4.1 Rotation powered pulsars

After the supernova that formed them, pulsars radiate away their rotational energy by pumping energy into the surrounding plasma. This *spin-down luminosity* can be estimated by approximating the neutron star as a rotating magnetised object, which will radiate energy, E, as a dipole at a rate given by the Larmor formula:

$$-\dot{E} = \frac{32\pi^4}{3c^2} P_{\rm spin}^{-4} \left[B R_{NS}^3 \sin\phi \right]^2 , \tag{1.32}$$

where B is the magnetic field, $P_{\rm spin}$ is the spin period and ϕ is the angle between the rotation axis and the magnetic dipole. Moreover, pulsars are observed to slow down, and current radio telescope facilities allow us to measure the rate at which the spin period changes, $\dot{P}_{\rm spin}$. So, it is possible to estimate the amount of rotational energy generated by the braking of the pulsar as

$$\dot{E}_{\rm rot} = -4\pi^2 I \dot{P}_{\rm spin} P_{\rm spin}^{-3}, \tag{1.33}$$

where I is the NS moment of inertia. It is clear that the observed spin-down luminosity is generated by extracting rotational kinetic energy from the pulsar. Therefore, by equating Equation 1.32 and Equation 1.33, we can estimate the strength of the surface magnetic field, B, from observable quantities as

$$B > 3.2 \times 10^{19} \left(P_{\rm spin} \dot{P}_{\rm spin} \right)^{1/2} \quad . \tag{1.34}$$

The rate at which the pulsar slows down can be described as

$$\dot{P}_{spin} \propto P_{spin}^{2-n} \quad , \tag{1.35}$$

where n is known as the braking index (and it follows from Equations 1.32 and 1.33 that $n = 3$). If we assume that the magnetic field does not decay throughout the life of the pulsar (therefore the braking index is constant) and the initial spin period is much smaller than the observed $P_{\rm spin}$, we can determine a characteristic spin-down time-scale (or age, τ) by integrating Equation 1.35:

$$\tau = \frac{P_{\rm spin}}{2\dot{P}_{\rm spin}} \quad . \tag{1.36}$$

These quantities ($P_{\rm spin}$, $\dot{P}_{\rm spin}$, B and τ) allow us to classify the pulsar population in a meaningful way. In Figure 1.10, I show the $P_{\rm spin}$-$\dot{P}_{\rm spin}$ diagram for the latest compilation

of known pulsars from the Australian Telescope National Facility (ATNF). This plot allows us to dissect the NS population into distinct groupings and trace their evolutionary paths. The initial supernova produces a high surface magnetic field (B$> 10^{12}$ G) and very fast rotating NS. Many of these objects are observed as young pulsars ($\tau \lesssim 10^5$ yr) and are usually associated with supernova remnants e.g. Crab or Vela pulsars. However, the strong torque exerted by the magnetic field quickly extracts energy from the neutron star, slowing the pulsars ($P_{\rm spin} \gtrsim 1$ s). As it evolves, the pulsar will be displaced towards the *death line*, where the combination of low B and long $P_{\rm spin}$ will eventually shut-down the acceleration of particles, causing the suppression of electromagnetic radiation. This natural evolution for pulsars can explain the accumulation/dearth of objects before/after the death line, as observed in Figure 1.10. However, in the last decades, more sensitive large all-sky radio surveys have revealed a large (and previously unexpected) population of old millisecond pulsars (MSPs).

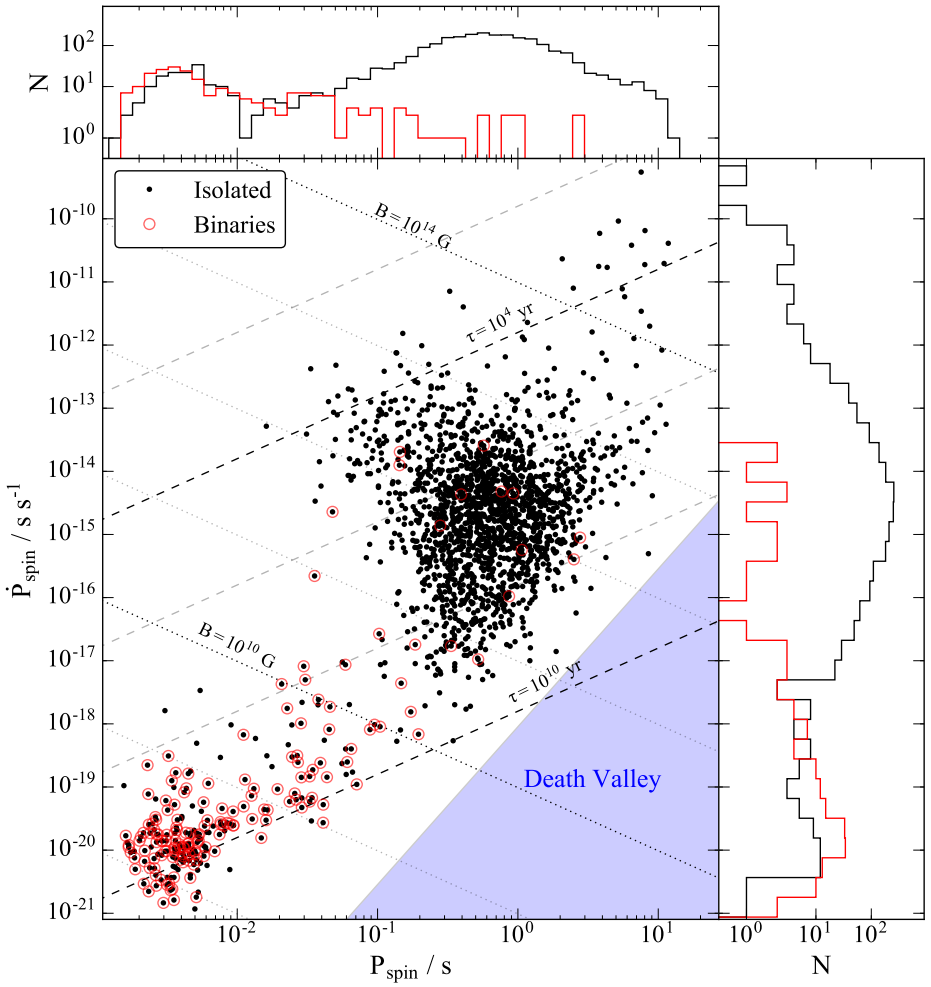

FIGURE 1.10: $P_{\rm spin}$-$\dot{P}_{\rm spin}$ of known radio pulsars. Lines of constant magnetic field (B) and characteristic age (τ) are shown. Histograms in the top and right panel show the fraction of isolated (*black*) and pulsars in binary systems (*red*). Data taken from ATNF pulsar database[3](v1.54, Manchester et al. 2005).

MSPs are old systems ($\tau \simeq 1 - 10$ Gyr) with fast spin periods ($P_{\rm spin} < 8$ ms) and low magnetic fields ($B < 10^{10}$ G). About half of them are found in binary systems, as shown in Figure 1.10. The companions to these MSP binaries can be quite diverse, as exemplified in Figure 1.11. Their population includes different types of WDs. Most of them harbour low-mass He WDs ($\sim 43\%$ of all systems), while only a small fraction host CO WDs as companions (only 11 MSPs-CO WD binaries are known to date). Meanwhile, the rest of these systems can contain other non-degenerate companions, such as low-mass main sequence stars ($M_2 \lesssim 0.2$ $M_\odot$) and ultra-light brown-dwarfs/planets ($M_2 \leq 0.03$ $M_\odot$). These are often referred to as *redbacks* and *black widows*, respectively (Roberts 2013), for reasons that will now be explained.

1.4.1.1 A world of spiders

Intense research has followed since the first discovery of the millisecond pulsar, PSR 1957+20, as part of a binary system (Fruchter et al. 1988b). Their long and irregular eclipses lead to the conclusion that dense material (outside the Roche-lobe surface of the donor) is being ejected from the system, most likely stripped from an evaporating, very low mass companion ($M_2 < 0.02$ $M_\odot$ Fruchter et al. 1988a;b). Further monitoring of theses sources revealed more systems with unusual close orbits ($P_{\rm orb} < 1$ d) , implying very energetic interactions between the donor and the accelerated particles in the pulsar wind. This cannibalistic nature prompted the name *black widows* for those systems. The number of confirmed black widow systems has increased up to 35 since the discovery of PSR 1957+20, up to half of which are found inside globular clusters (Roberts 2013).

The discovery of PSR J1023+0038 provided evidence for a new class of systems, *redbacks*. These share many common traits with black widows, with the main difference being that their companions are low-mass stars ($M_2 \sim 0.2$ $M_\odot$). In contrast to the black widows, these systems remained mostly undetected until the launch of *Fermi* Gamma-ray Space Telescope (Abdo et al. 2013). Follow-up observations of unidentified *Fermi* sources have so far revealed 18 new redback systems, all shown in Figure 1.11.

Finally, a new addition to the spider family is the recent discovery of systems with orbital periods > 5 days, capable of accommodating an evolved red giant star, known as *huntsman* systems. The best example of these is 1FGL J1417.7−4407 (Strader et al. 2015), where initial mass determinations pointed towards a massive NS ($1.77 < M_1 < 2.12$ $M_\odot$) and a companion mass of $M_2 = 0.33 \pm 0.3$ $M_\odot$. Follow-up radio observations have since revealed a 2.2 millisecond pulsar in this system. 1FGL J1417.7−4407 may represent the precursor to the presence of systems harbouring a He WD as a companion (Camilo et al. 2016).

[3] http://www.atnf.csiro.au/people/pulsar/psrcat

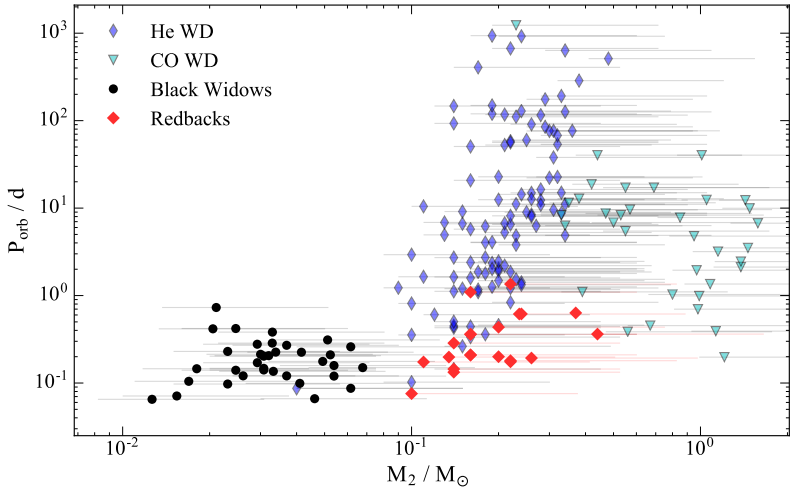

FIGURE 1.11: Donor mass distribution of accreting pulsars and P_{orb}. The quoted mass is obtained by assuming an inclination of $i = 60°$, while the error bars represent the range from the minimum mass ($i = 90°$) to $i = 40°$. Data taken from ATNF (Manchester et al. 2005) and A. Patruno database[5]

1.4.1.2 Formation Channels

The evolution of NS systems follows a similar path to that described for accreting white dwarfs (Section 1.3.1). It is mainly driven by the loss of angular momentum (via gravitational radiation and magnetic braking). Despite these similarities, the neutron star at its center is a major energy source, and its effects are seen when analysing the overall distribution of systems. In particular, the timescales required to reach the small observed values of donor masses (as exemplified in Figure 1.11) are larger than the age of the Universe if the only source of AML were gravitational radiation emission. Clearly, if we are to reproduce the observed population, we require mechanisms that accelerate the evolution. The most obvious physical concepts that have to be added to this standard model for NS systems are the energetic pulsar wind that strikes the companion, as well as the strong irradiation of the donor.

Since the discovery of the first black widow system, the energetic pulsar wind has been invoked as a mechanism to evaporate the companion (van den Heuvel & van Paradijs 1988). The ultimate consequence of this, the total evaporation of the companion, can naturally explain the population of isolated MSPs (Phinney et al. 1988). Observational evidence for such outflow arising from the ablated companion has been observed as extended eclipses by intervening material in both redbacks and black widows (e.g. Archibald et al. 2009).

Recent detailed calculations including the effects of the pulsar wind can produce a continuous distribution of redback and black widow systems. This evolution is particularly sensitive to the initial conditions of the system, such as the mass of the companion

and the initial period. However, when feedback from the energetic pulsar wind is accounted for, it is possible to accelerate the evolution and ablate the companion faster (Benvenuto et al. 2015). This produces a natural progression between systems of donor masses ~ 0.2 $M_\odot$(redbacks) and black widow systems ($<\sim 0.02$ $M_\odot$). Consequently, all black widow systems represent an evolutionary stage just before turning into an isolated MSP (Benvenuto et al. 2014; 2015). The combination of evaporation efficiency and orbital separation might explain the existence of distinct evolutionary paths for redbacks/black widows and MSP-He WD binaries (Jia & Li 2015).

Alternatively, Chen et al. (2013) proposed that black widow and redbacks systems are part of two distinct evolutionary populations. As they evolve, the degree of ablation of the companion is a function of the efficiency of the pulsar wind. This can be explained by the angle at which the pulsar wind hits the donor, which determines the amount of the spin-down luminosity that is absorbed. This mechanism reproduces the bi-modal distribution of donor masses observed in binary MSPs, shown in Figure 1.11.

King et al. (2003; 2005) propose that the over-abundance of black widow systems in globular clusters is due to dynamical interactions. In the dense cores of globular clusters, close encounters between single stars and binary systems are relatively common. In such an encounter, it is usually the lowest mass object that is ejected, while the two more massive stars emerge as a tight binary system. Thus a 3-body encounter between a low-mass star ($\gtrsim 0.1$ $M_\odot$) and a MSP binary system containing its original He WD companion will typically lead to the ejection of the He WD. The remaining binary system then becomes visible as an MSP if the donor fills its Roche lobe due to angular momentum loss or nuclear expansion.

Another route that may complement the previous scenarios is the accretion-induced collapse scenario (AIC). Smedley et al. (2015) explored the possibility that these systems are the descendants of very massive (~ 1.37 $M_\odot$) and rapidly rotating WDs that collapsed to a neutron star after a CV phase. The sudden release of energy when the NS forms, causes the orbit to increase and the donor to detach. The cessation of accretion allows the pulsar wind to resume and ablate the companion. These systems are predicted to lie well within the parameter space occupied by the known redbacks.

1.4.2 Accretion powered neutron stars

The high magnetic fields in MSPs, and indeed in all pulsars ($B > 10^8 - 10^9$ G), will dominate the dynamics far enough from the NS to prevent the accretion flow from reaching the surface directly. There are then three characteristic length scales that will determine the accretion geometry onto the NS.

1.4.2.1 Accretion onto magnetised objects

We can define the *magnetosphere* of a NS as the volume where the magnetic field can strongly influence the accretion flow. The infalling gas onto the NS will be able to approach until an equilibrium between the ram and magnetic field pressures is reached. For a spherically symmetrical flow, this will happen when:

$$\frac{B^2(r)}{8\pi} = \rho v^2(r) \quad , \tag{1.37}$$

where ρ is the density of the accreted gas. Assuming a dipole field for the neutron star ($B(r) = \mu r^{-3}$, where $\mu = BR_1^3$ is the magnetic moment of the pulsar) and taking the free-fall velocity ($v^2 = 2GM_1 r^{-1}$) for the gas, we can then estimate the radius of the magnetosphere, commonly known as the Alfvén radius, as (e.g. Ghosh & Lamb 1979; Lamb & Ghosh 1991):

$$r_A = \left(\frac{\mu^4}{2GM_1\dot{M}}\right)^{1/7} \simeq 3.2 \times 10^8 \dot{M}_{17}^{-2/7} \mu_3 0^{4/7} \frac{M_1}{M_\odot}^{-1/7} \text{cm}, \tag{1.38}$$

where $\dot{M}_{17}$ is in units of 10^{17} g s^{-1}, the μ in 10^{30} G cm^3.

The rotating dipole magnetosphere will preserve closed field lines as long as these can rotate with the NS. However, some field lines extend so far out from the object that they would have to be rotating faster than the speed of light to keep up. Any field lines beyond this characteristic radius, known as the *light cylinder*, will be distorted and extend outwards as open field lines. The radius of this light cylinder is given by

$$r_{lc} = \frac{cP_{\text{spin}}}{2\pi} \quad . \tag{1.39}$$

Material in Keplerian orbit close to the NS can latch onto the magnetic field lines and consequently accrete onto the surface as long as its angular velocity matches that of the NS. This defines the *corotation radius*, where the centrifugal force will balance the gravitational force, is given by

$$r_{co} = \left(\frac{GM_1 P_{\text{spin}}^2}{4\pi^2}\right)^{1/3} \quad . \tag{1.40}$$

1.4.2.2 Accretion regimes

The interplay between the pressure of the magnetic field and the accretion flow allows for three distinct accretion regimes: radio pulsar, propeller and channelled accretion. In particular, the location of the inner radius of the disc, r_{in}, is a parameter that can explain and provide insight into the characteristics of the accretion inflow (and outflow) from the system. Furthermore, every accretion regime can be associated with a characteristic

L_X, set by the mass accretion rate needed to penetrate the magnetosphere, as shown in Figure 1.12. When $r_{in} > r_A$ (shown in the left panel), the ram pressure from the accretion flow is not sufficient to allow accretion directly onto the compact object, hence the pulsar wind can easily clear material from the inner regions close to the compact object. Therefore, the NS can be observed as a rotation-powered pulsar.

At higher mass transfer rates (and/or weaker magnetic fields) the gas is able to penetrate the magnetosphere. However, if the gas does not have the required pressure to reach the corotation radius, i.e. $r_{co} < r_{in} < r_A$ (shown in the middle panel), the fast rotating magnetosphere creates a centrifugal barrier that prevents the material from latching onto the field lines and instead expels the accreted matter, acting as a *propeller* (Illarionov & Sunyaev 1975; Patterson 1994).

The third regime occurs when material from the disc can reach r_{co} (shown in the right panel). Its Keplerian velocity can then match that of the co-rotating magnetosphere and latch onto the field lines, so that material is channelled onto the magnetic poles of the NS. The energy released in this regime is often observed as X-ray pulsations on the spin period of the NS.

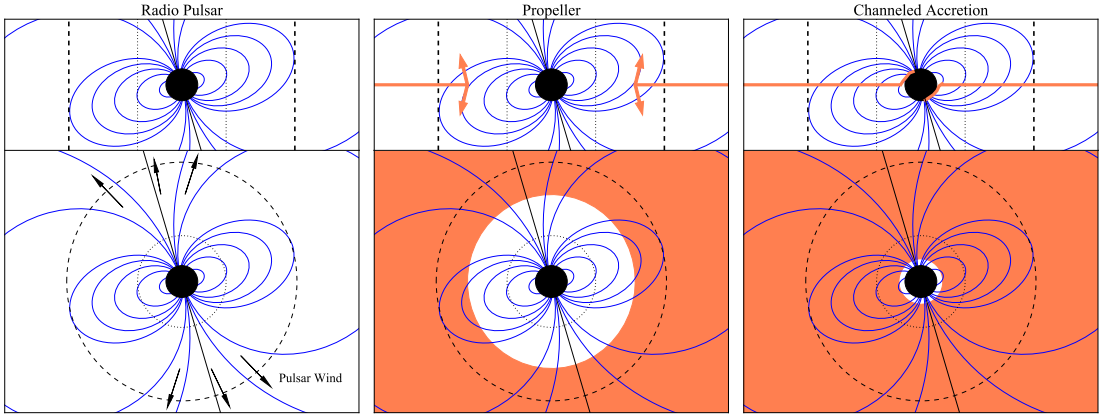

FIGURE 1.12: Diagram of accretion modes onto a magnetised compact accretor. The accretion disc (coral) can penetrate at different radii in the magnetosphere (r_A, dashed line) and reach the corotation radius (r_{co}, dotted line). The magnetic field lines (blue lines) and magnetic axis (black line) are shown for reference. Adapted from A. Archibald presentation at "The Zoo of Accreting Compact Objects", Leiden, 2015.

1.4.3 Recycling Scenario

How can we understand the large population of rapidly spinning millisecond pulsars that possess very low magnetic fields with long characteristic ages? The current paradigm, supported by observational evidence, involves the rejuvenation of the NS spin via accretion in a binary system, the so-called *recycling scenario* (Alpar et al. 1982; Bhattacharya & van den Heuvel 1991; Srinivasan 2010; for a recent review). This scenario

was later supported by the discovery of accreting millisecond X-ray pulsars (AMXPs, Wijnands & van der Klis 1998), providing confirmation of LMXBs as progenitors of isolated MSPs. Furthermore, the most recent evidence for the connection (and evolutionary link) between LMXBs and MSPs, was observed in a new population of systems that can transition between AMXP and radio MSP. Hence, we can use these latter systems to understand this unique evolutionary phase.

In binary systems, where a NS possesses a low-magnetic field, r_A can be located inside r_{co}, thus allowing material to accrete efficiently onto the NS surface. In this transition region, an exchange of angular momentum will take place as the gas stops rotating as a Keplerian disc and attempts to latch onto the magnetic field. The difference between their angular momenta will determine whether the NS spins up or spins down (Patruno & Watts 2012). The amount of gas accreted during a LMXB phase has been shown to provide enough sustained torque to reproduce the spin periods observed in AMXPs (Tauris & Savonije 1999). The increasing $P_{\rm spin}$ will push r_A outwards until it extends to r_{co} allowing an equilibrium period, P_{eq}, to be obtained by the NS (Illarionov & Sunyaev 1975).

The recycling process can, in principle, spin NSs up to the break-up frequency $\sim$ 1500 Hz. However, observationally, most MSPs seem to have $P_{\rm spin}$ in a narrow range (200-500 Hz), with the current record holder, J1748-2446ad having $P_{\rm spin}$= 725 Hz (Hessels et al. 2006). As the Roche-lobe overflow phase terminates, the newly recycled MSP may go through a spin-down process as the accretion disc empties, removing angular momentum from the spun-up pulsar. This process may help explain the slower $P_{\rm spin}$ distribution of radio MSPs (Tauris 2012) when compared to MSPs in binary systems, as shown in Figure 1.13. It has been suggested that the upper limit of the spin frequency is set during the decouple stage between the accretion disc and the magnetosphere. As the mass transfer rate drops below a certain threshold, the Alfvén radius will be pushed outside the light cylinder, stopping accretion onto the NS. During this short transition, the NS undergoes a propeller regime. The material being ejected by the propeller will carry away angular momentum, thus spinning down the NS (Tauris 2012). Alternatively, gravitational wave emission has been proposed as a mechanism to remove angular momentum from the system, thus reducing the final recycled $P_{\rm spin}$ (Bildsten 1998; Chakrabarty et al. 2003).

1.4.4 Transitional Millisecond Pulsars

The discovery of systems that switch between accreting and radio pulsar states, known as *transitional millisecond pulsars* (tMSP), may well represent the evolutionary *missing link* between LMXBs and MSPs. Their existence is thus a vindication of the recycling scenario. It is only in the last decade that we have been able to monitor systems long enough to observe such transition.

To date, there are three confirmed sources belonging to the tMSP category: M82-I (Papitto et al. 2013b), PSR J1023+0038 (Archibald et al. 2009) and XSS J122704859 (de Martino et al. 2010; Hill et al. 2011; Roy et al. 2014). In particular, PSR J1023+0038 was the first redback system to be discovered, as well as the first seen to switch between states in both directions. This shows that the process of turning-off the accretion in a LMXB is not a sharp one, requiring multiple transitions (Tauris 2012). Since PSR J1023+0038 is a subject of this thesis, I will provide a more detailed account of its properties in Chapter 4.

The direct connection between disc-accreting sources and spun-up MSPs is further strengthened when comparing the distribution of AMXP spin periods and those of non-accreting radio pulsars (redbacks and black widows), as shown in Figure 1.13. Despite the relatively small number of systems, these two distributions have been found to be similar, suggesting an evolutionary connection between them (Tauris 2012; Papitto et al. 2014b).

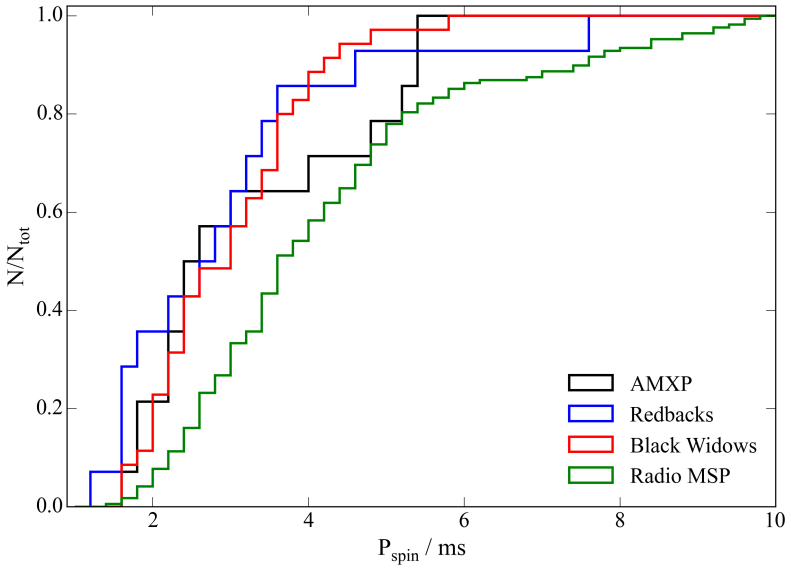

FIGURE 1.13: Spin period distribution of millisecond pulsars.

These systems are characterised by multi-wavelength emission that can vary on timescales of ∼weeks and years, spanning six orders of magnitude in luminosity. Regardless, the three confirmed tMSPs share several key observational features, as follows.

1.4.4.1 Observational Phenomenology

Linares (2014) has divided the observational characteristics of tMSPs into three distinct states, separated by their X-ray luminosity, L_X:

- Pulsar state, $\sim 10^{31} < L_X < 4 \times 10^{32}$ erg s^{-1}: The system at these luminosities is observed as a redback system, in which millisecond radio pulsations are observed. The radio pulse exhibits variable eclipses, with increasing duration at lower frequencies (e.g. PSR J1023+0038, Archibald et al. 2009). The location of the eclipse in pulse phase is variable between observations. This suggests that the pulsar wind is carrying a significant outflow, most likely from the ablation of the companion. During this state, there is no evidence for an accretion disc, suggesting that the pulsar wind inhibits any accretion onto the pulsar. The donor, visible in optical and NIR wavelengths, presents ellipsoidal modulation (with the star underfilling its Roche-lobe) as well as a reflection effect driven by the irradiation of the secondary due to the highly energetic pulsar wind (McConnell et al. 2015). The X-ray emission shows a modulation on the orbital period, and low-level γ-ray emission is also observed.

- Disc state, $4 \times 10^{32} < L_X < 10^{34}$ erg s^{-1}: In this state, the system is observed in an LMXB phase, characterised by the formation of an accretion disc that dominates the optical and UV emission. The enhanced mass transfer suppresses the radio pulsations (while residual radio emission is still observed). In X-rays and some optical bands, the lightcurves show peculiar transitions lasting $\lesssim$ 500s, with changes in luminosity of factors of ∼2-3 (Linares et al. 2014b; Bogdanov et al. 2015; Archibald et al. 2015). As a consequence, histograms of the count rate values for these lightcurves reveal clear bimodal distributions in X-rays as well as at UV and optical wavelengths, known as *low* and *high* modes(Shahbaz et al. 2015). In high mode, the system shows X-ray pulsations (at the $\sim 10\%$ level), while in the low mode the pulsations disappear. These coherent X-ray pulsations, suggesting channelled accretion onto the surface of the NS, occur at X-ray luminosities ~ 100 times fainter than in any AMXPs. There is no apparent periodicity controlling the mode switching. Occasional flares lasting ∼minutes also occur during this state. The γ-ray luminosity (in the $\sim 0.1 - 300$ GeV range) exceeds L_X by a factor of ~ 5. The radio emission presents a flat-spectrum consistent with a compact jet similar to other NS-LMXBs. However, all known and suspected tMSPs seem to be over-luminous at radio wavelengths when compared to their corresponding L_X (Deller et al. 2015). The optical and infrared spectrum is dominated by the underlying irradiated companion and the accretion disc with double-peaked lines of HI and HeI of FWHM$\sim$ 1000 km s^{-1} (Coti Zelati et al. 2014).

- Outburst state, $10^{34} < L_X < 10^{37}$ erg s^{-1}: Only M28-I has been observed in a full outburst (Papitto et al. 2013b) that lasted a few months before switching to a quiescent state. The X-ray spectrum presents a broad Fe Kα line, the signature of a reflection component from a truncated disc. The system also showed evidence of channelled accretion via X-ray pulsations on the spin period as well as type-I X-ray bursts. No γ-ray emission is observed during this state. As with the accreting state, there is no evidence for radio pulsations.

Chapter 2

SDSS J143317.78+101123.3

or how to transition from star to brown dwarf

"Life is pleasant. Death is peaceful. It's the transition that's troublesome."

- Isaac Asimov, *Fantastic Voyage II: Destination Brain*

I would like to acknowledge R. Breton for useful discussions and advice on light curve modelling. The main parts of this chapter have been published in Nature as Hernández Santisteban et al. (2016).

SDSS J143317.78+101123.3 (SDSS J1433+1011 hereafter) was discovered as a WD-dominated CV with strong emission lines (Szkody et al. 2007). The presence of WD features in the optical spectrum usually points to a low mass accretion rate. WD-dominated systems are therefore good period bouncer candidates. Later on, fast photometric observations with ULTRACAM (Dhillon et al. 2007) and detailed eclipse modelling was used to determine the system parameters, revealing the presence of a very low-mass donor $M_2 = 0.059 \pm 0.003$ $M_\odot$ in this system (Littlefair et al. 2008; Savoury et al. 2011). Independent measurements of radial velocities obtained from Hα (for the WD, Tulloch et al. 2009) and near-infrared J-band spectroscopy (for the donor, Littlefair et al. 2013) provided tentative evidence for a sub-stellar donor in the system (SpT=L2$\pm$1).

Therefore, the unequivocal detection of a brown dwarf could serve as a proxy to classify period bouncers. However, it is difficult to detect the light of the donor directly. Furthermore, all the donors in these systems should have reached the sub-stellar regime. Few in-depth studies of the donors have targeted the NIR (e.g. Ishioka et al. 2007), where the sub-stellar donor is expected to have the largest contribution. Only in a handful of cases has a direct detection been achieved e.g. PHL 1445 (McAllister et al. 2015), SDSS J1433+1011 (Littlefair et al. 2013; Hernández Santisteban et al. 2016) and WZ Sge (Harrison 2016).

In this Chapter, I will present simultaneous optical and NIR time-resolved spectroscopic observations of SDSS J1433+101133. This wide wavelength coverage allowed me to perform a detailed characterisation of the donor, as well as a direct mass measurement of the brown dwarf companion. Light-curve modelling allowed me to retrieve the albedo and heat circulation efficiency in the donor's atmosphere. I will also present Doppler tomography of the accretion disc in the system. Finally, I will discuss the importance of my findings in the context of binary evolution and the physics of (sub-)stellar atmospheres.

2.1 Observations

The data used in this chapter were taken with X-Shooter (Vernet et al. 2011) at the Very Large Telescope (VLT) in Cerro Paranal, Chile. This instrument provides simultaneous medium resolution spectroscopy ($R \sim 4000$) in three independent bands: UVB (300-520 nm), VIS (500-1000 nm) and NIR (1000-2550 nm). The observations were divided into five observation blocks, using the $1.3\times11''$, $1.2\times11''$ and $1.2\times11''$ slits and 274, 286, 300 s exposure times for UVB, VIS and NIR bands, respectively. All spectra were taken in nodding mode to allow for an optimal sky subtraction in the NIR. After every observation block, a late B-type star was observed at a similar airmass to allow for correction of telluric features. Spectra of spectro-photometric standard as well as of wavelength calibration lamps, are taken daily at the VLT to allow precise calibration. The observation log is presented in Table 2.1.

Object	Date (UTC)	MJD begin	MJD end	No. of images
SDSS J1433+1011	Apr 04 2010	55290.18841513	55290.38067120	48
SDSS J1433+1011	Jul 24 2010	55401.99279378	55402.04480039	16
SDSS J1433+1011	Jul 25 2010	55402.98303118	55403.03503726	16
Hip 080227 (B9 V)	Apr 04 2010	55290.25195021		2
Hip 066454 (B8 V)	Apr 04 2010	55290.32369541		2
Hip 072154 (B9.5 V)	Apr 04 2010	55290.39302201		2
Hip 072154 (B9.5 V)	Jul 24 2010	55402.05783440		2
Hip 080227 (B9 V)	Jul 25 2010	55402.04612046		2

Table 2.1: Observation log of SDSS J1433+1011 and telluric standards.

2.1.1 Data Reduction

The data were debiased, flat-fielded and wavelength calibrated by using the X-Shooter pipeline (v. 2.2, Modigliani et al. 2010). The UVB and VIS arm were extracted and flux calibrated with the flux standard stars taken daily at the VLT. Sky subtraction was performed in the NIR arm by pairing consecutive images in AB–AB sequence. When using the X-Shooter pipeline, the resultant spectra contained an artificial feature not

accounted for by the pipeline around 2.1 μm, as clearly seen in the upper panel of Figure 2.1. Therefore, I constructed a custom instrument response in order to calibrate all NIR spectra by using the telluric standard spectra closest in time to each observation block. In the NIR, B-type stars follow the Rayleigh-Jeans tail of a black-body distribution (given that their effective temperatures of ∼10,000 K peak at optical or near-UV wavelengths). The telluric 1D spectra were extracted with the pipeline before any flux calibration. Subsequently, I divided the raw spectra by a black-body of the appropriate temperature and forced it to match the 2MASS $J-$band photometry. From this noisy empirical instrument response, I created a smooth response by fitting the continuum with a spline function of 7th order to two different regions (1000-1800 nm and 1800-2500 nm). Finally, these two sections were merged into a continuous function and used as the 1D response file in the X-Shooter pipeline to reduce the science spectra. As shown in the bottom panel of Figure 2.1, the 2.1 μm feature is not present in the flux-calibrated spectra of the telluric. Afterwards, the telluric features in the VIS and NIR spectra were corrected using MOLECFIT (Kausch et al. 2014). Finally, the mid-exposure times of all spectra were corrected to a barycentric reference frame.

A potential problem with the flux calibration in the dataset are slit losses. In order to minimise its effect, all observations were performed with seeing $\sim 0.8 - 1.0$ arcsec and the slit was oriented with the parallactic angle. The flux standards were taken with a 5 arcsec width, in order to properly assess the slit losses and are accounted when constructing the instrument response. I have used the phase 3 data products as a reference for the combined spectra to estimate the flux scale error to be $\sim 2\%$.

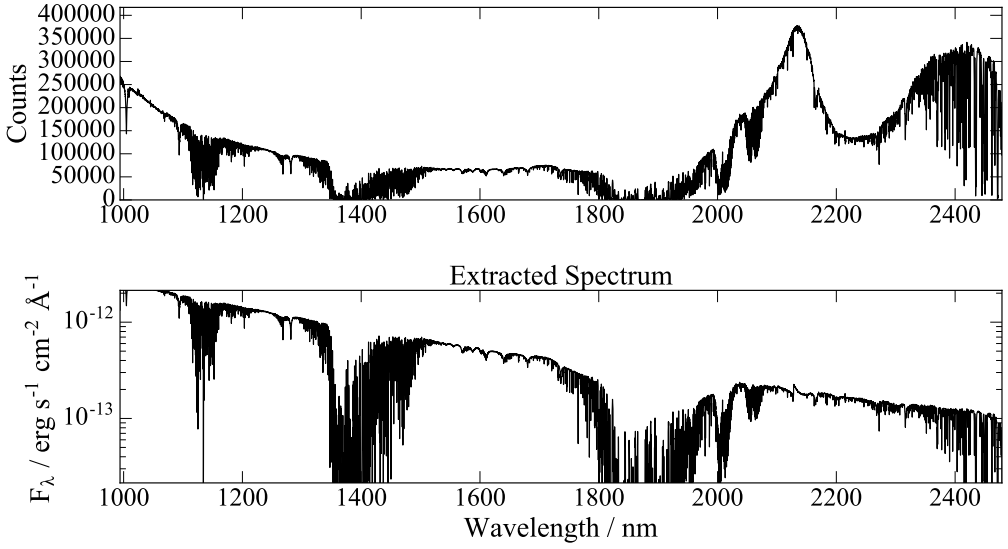

FIGURE 2.1: X-Shooter NIR response calibration. *Upper panel:* The extracted 1D spectra for the telluric standard. The very clear feature around 2.1 μm dominates. *Bottom panel:* Flux calibrated spectra of the telluric standard by using the empirical instrument response.

2.2 Photometry

I performed synthetic photometry on the flux-calibrated spectra of the three arms using Sloan filters (u',g',r',i',z') for the optical and Bessel filters (J, H, K) for the NIR. The resulting light curves, shown in Figure 2.2, are transformed to AB magnitudes and shifted for clarity. The optical region reveals a deep eclipse and the hot-spot bump at $\phi \sim 0.9$, similar to previous observations (Littlefair et al. 2006). The primary eclipse becomes shallower with increasing wavelength. In the NIR bands, the light curves show a clear double (ellipsoidal) modulation, produced by the distorted shape of the donor (see Section 2.4.3 for more details).

2.3 Spectral Energy Distribution

The spectral classification of the donor star can be used as a direct measure of the evolutionary status of a CV. More specifically, a measurement of its $T_{\rm eff}$ and $\log g$ can be compared directly to theoretical or semi–empirical models. The NIR is the most suitable region for isolating the "pure" donor spectrum, since we expect it to contribute roughly 40% of the out-of-eclipse light in J and 50% in H and K bands (Knigge et al. 2011). However, in order to assess and characterise the donor, it is still necessary to measure the contributions of the WD and the accretion disc.

2.3.1 A revised temperature for the WD

The SED of the WD in SDSS J1433+1011 is expected to peak at UV wavelengths, since $T_{\rm eff}= 12,700 \pm 1500$ K (Savoury et al. 2011). Based on the ultraviolet data obtained by the Galaxy Evolution Explorer (GALEX, Martin et al. 2005), the system produces NUV (1692 -3006 Å) and FUV (1340-1806 Å) fluxes of $3.94 \pm 0.4 \times 10^{-16}$ erg s^{-1} cm^{-2} Å^{-1} and $8.1 \pm 1.0 \times 10^{-16}$ erg s^{-1} cm^{-2} Å^{-1}, respectively[1]. The donor's contribution in the UV flux is negligible due to its low effective surface temperature. However, the accretion disc can reach the surface of the WD and its SED may peak in the UV. In order to establish the possible contribution of the accretion disc, I calculated the expected fluxes of a standard optically thick and geometrically thin disc (see Section 1.22). I constructed the SED using typical values for a system at the period minimum: $\dot{M} \sim 3 \times 10^{-11}$ M$_\odot$ yr^{-1}(Knigge et al. 2011; taken from the revised CV evolutionary track,), $R_{in} = R_{WD} = 0.00962$ R$_\odot$, $R_{out} = 0.331$ R$_\odot$(Savoury et al. 2011) and scaled to match the contribution in the optical from the light curve modelling. Then, I performed synthetic photometry with the GALEX filters and compared the fractional contribution to the observed fluxes. I found a contribution in the NUV of $\sim$ 16% and $\sim$ 6% in the FUV. Although these

[1]There is also *Swift*-UVOT archival data for the system that provides similar UV flux estimates of UVW1= $5.10 \pm 0.08 \times 10^{-16}$ erg s^{-1} cm^{-2} Å^{-1} and UVW2= $8.69 \pm 0.42 \times 10^{-16}$ erg s^{-1} cm^{-2} Å^{-1}.

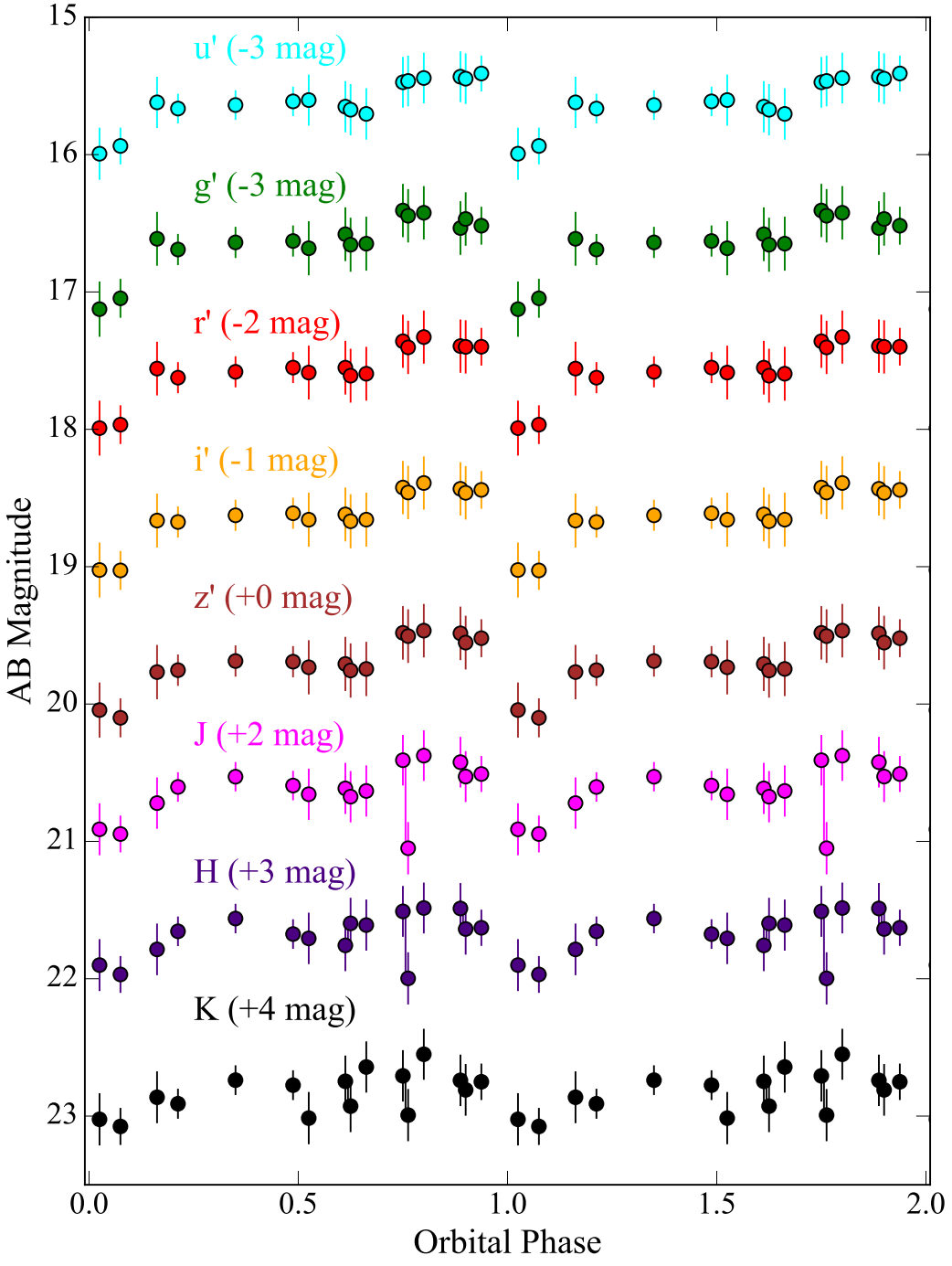

FIGURE 2.2: Optical and near-infrared synthetic photometry for SDSS J1433+1011. Each light curve has been scaled for display purpose (indicated for each filter in parentheses).

contributions are small, particularly in the FUV, they will introduce a systematic error in the measurement, overestimating the WD temperature. However, for simplicity, I have assumed that GALEX UV measurements will trace only the SED of the WD.

Using these data, I determined an improved WD $T_{\rm eff}$ by fitting a WD atmosphere

model (Hubeny & Lanz 1995) to the GALEX UV fluxes, using χ^2 as the goodness of fit parameter. This parameter is used to evaluate a model, f_n described by parameters $\bar{\theta}$ against a set of observations, x_n, y_n with their respective uncertainties σ_i[2]. Thus, it is defined as:

$$\chi^2 = \sum_{n=1}^{N} \frac{[y_n - f_n(x_n, \bar{\theta})]^2}{\sigma_i^2} \quad . \tag{2.1}$$

We can define the quantity $\chi^2_\nu = \chi^2/K$, where $K = N - M$ are the degrees of freedom (number of datapoints, N, and M, number of free parameters). In general, we can evaluate the quality of a specific model to reproduce the data (within its uncertainties) using χ^2_ν. If a fit results in a $\chi^2_\nu > 1$ it is considered a bad fit, whereas $\chi^2_\nu < 1$ is considered as an overfit (Andrae et al. 2010). In practice, if one considers that the model *truly* represents the data, then one can adjust the errorbars by adding a systematic factor (additive, $\sigma_i^2 + \sigma_s^2$, or multiplicative, $(f\sigma_i)^2$) so the fit converges at $\chi^2_\nu = 1$.

I have assumed the WD radius and surface gravity, $R_{WD} = 0.00958\ R_\odot$and $\log(g) = 8.5$ respectively and the distance of the system, $d = 226$ pc (Savoury et al. 2011). The 1σ confidence values were obtained by scaling the uncertainties so $\chi^2_{nu} = 1$. The result, presented in Figure 2.3, is an updated estimate of $T_{WD} = 13200 \pm 400$ K[3]. This value is consistent with a previous estimate obtained via eclipse modelling (Savoury et al. 2011), for which the UV data was not available at the time.

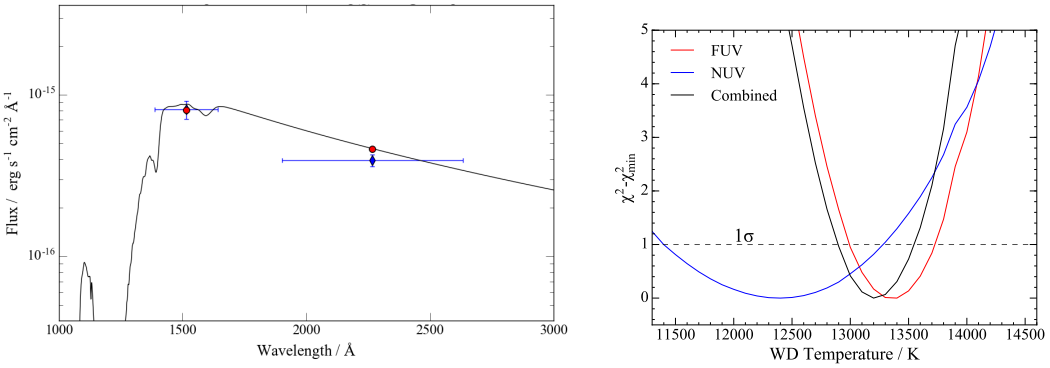

FIGURE 2.3: Effective temperature of the WD. *Left:* The fit shows the photometric FUV and NUV values obtained by GALEX (blue points) and the WD synthetic spectra. *Right:* The $\Delta\chi = \chi^2 - \chi^2_{min}$ for the combined fit and its associated 1σ level (dashed line).

[2]This method implies that the measurement errors are Gaussian and independent.

[3]Although the statistical error is small on T_{WD}, the systematic error due to the contribution of the disc and degeneracies between WD models will dominate the error budget. I performed a sanity check on the results of Section 2.4.3 due to the effect of the possible range of WD temperature, using the lower and upper limits of (Savoury et al. 2011) values. The overall effects manifest as an offset in the flux scale of the donor signal of the order of $\sim 10\%$ and do not change the overall conclusions of this chapter.

2.3.2 The SED model

In order to fit the accretion disc and the contribution for the donor, the model makes the following assumptions. First, the WD is fully visible at all phases except in eclipse. In the particular exposures around the primary eclipse, I took into account the fraction of time during which the WD is occulted (assuming $f_{wd} = 0$ during eclipse). Second, the contribution from the accretion disc and hot spot were modelled as a simple power law:

$$f_{PL} = a \cdot f_J \cdot \left(\frac{\lambda}{\lambda_J}\right)^{\alpha} \quad , \tag{2.2}$$

where a is the fractional contribution from the total flux, α is the power law index and f_J is the J band average flux, centred at λ_J. I used a fixed power law index of $\alpha = -7/3$, since the optically thick accretion disc plateau extends up to the infrared. This assumption is further strengthened by the measurement of the outer accretion disc radius in Section 2.5.3.

In order to asses the contribution of the donor, as well as determining its spectral type, SpT, I used an empirical spectral sequence selected from the IRTF Spectral Library[4] (Cushing et al. 2005) and BDSS[5] Library (McLean et al. 2003) in a spectral range from M6-L8. In order to use a homogeneous set of objects in the fitting process, every template must be scaled properly.

Since stellar radii measurements for brown dwarfs are quite uncertain, I used the Barnes-Evans empirical relation (Barnes & Evans 1976; Beuermann 2006) to scale every template accordingly. This relation assumes a unique track of surface brightness against spectral type for low-mass stars allowing us to infer R_{BD} for each template. As a sanity check, I constructed a SpT-M_{Ks} and compared the empirical sample using published distances, compiled by the Brown Dwarf Archive[6]. In addition, I compared my sample with the updated track fits from Dupuy & Liu (2012). As seen in Figure 2.4, some of the objects deviate significantly from the relation. Further literature review on the individual objects demonstrated that all of these systems have recently been identified as binaries. Therefore, I excluded them from the final empirical sequence. The spectral sequence as well as the temperature calibration are compiled in Appendix A. Therefore, every brown-dwarf template was multiplied by the scaling factor, b, given by:

$$b = \left(\frac{R_2}{d_2} \cdot \frac{d_{BD}}{R_{BD}}\right)^2 \quad , \tag{2.3}$$

where $R_2 = 0.109 \pm 0.003$ $R_\odot$ is the geometrical radius of the Roche–filling donor (Savoury et al. 2011), R_{BD} the radius of the template star and its corresponding distance, d_{BD}. The absolute flux calibration and the precise geometric constrains given by

[4]Infrared Telescope Facility: http://irtfweb.ifa.hawaii.edu/~spex/IRTF_Spectral_Library/
[5]Brown Dwarf Spectroscopic Survey: http://www.astro.ucla.edu/~mclean/BDSSarchive/
[6]For an up–to–date database: www.browndwarf.org

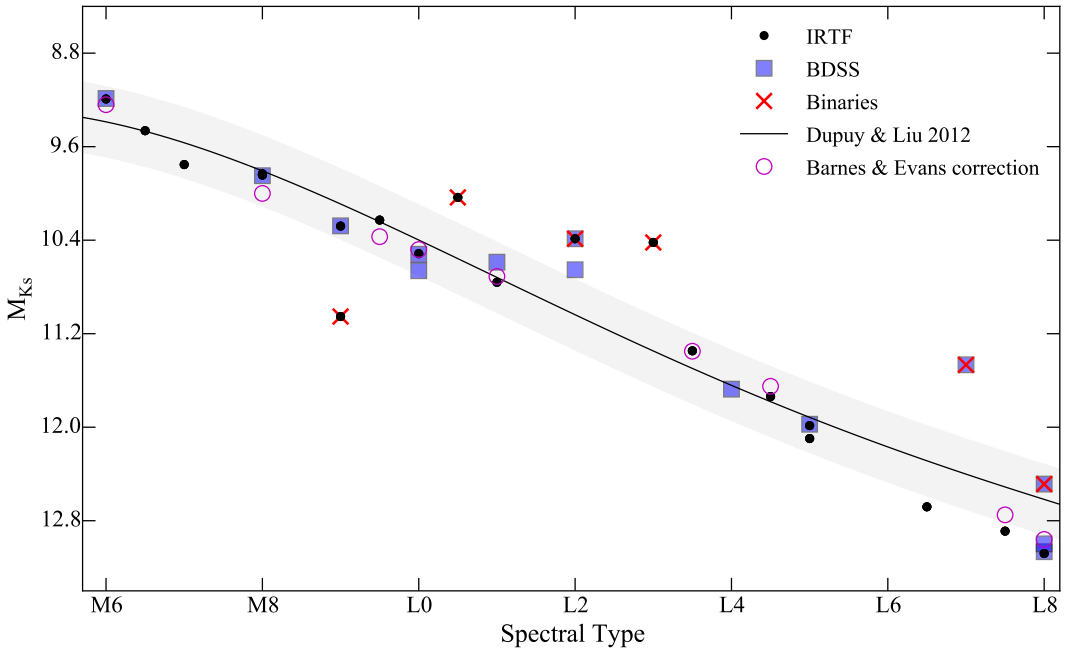

FIGURE 2.4: Absolute Magnitude in K_s band as a function of spectral type for our brown dwarf sample. Templates from IRTF (*circles*) and BDSS (*squares*) are shown. Systems found out to be binaries are crossed out. Dupuy & Liu (2012) (*dashed line*) and the rms = 0.3 for M and L objects (*shaded gray*) are shown for comparison purposes.

the eclipse modelling (Savoury et al. 2011), allowed me estimate a realistic contribution of a given SpT in the system. Therefore, I maintained the normalisation parameter b fixed in the SED fit in order to avoid degeneracies with the power-law contribution.

Finally, the full SED of the system, f_{total}, is modelled by the sum of each component's contribution:

$$f_{total} = f_{WD} + f_{PL}(a, \alpha) + b \cdot f_{BD} \quad . \tag{2.4}$$

In order to increase the signal to noise (particularly in the NIR), I constructed an average spectrum of the UVB and NIR arms. Then, I rebinned it to the template to a linear wavelength sampling scale (0.6 Å/pix) and the emission lines (hydrogen Paschen and Brackett series and HeI) were masked to ensure the fit traced only the donor star and WD features. Finally, I performed an overall fit using a least-squares method to minimise χ^2, used as the goodness–of–fit parameter. The only free parameter in this fit was the normalisation of the power-law i.e. the accretion disc/hot spot contribution. I ran this fit for every different spectral type in order to obtain the best SpT that fitted the average spectrum. The table of results is shown in Table 2.2. I found that the average spectrum is consistent with a brown dwarf of SpT=L0±1. Although the errors are formally very small, as seen from the χ^2_ν values for the fits, the uncertainty quoted corresponds primarily to the intrinsic scatter of ±1 SpT of the template sequence. Given that the full decomposition of the system's SED with the best fit model is presented in Figure 2.5.

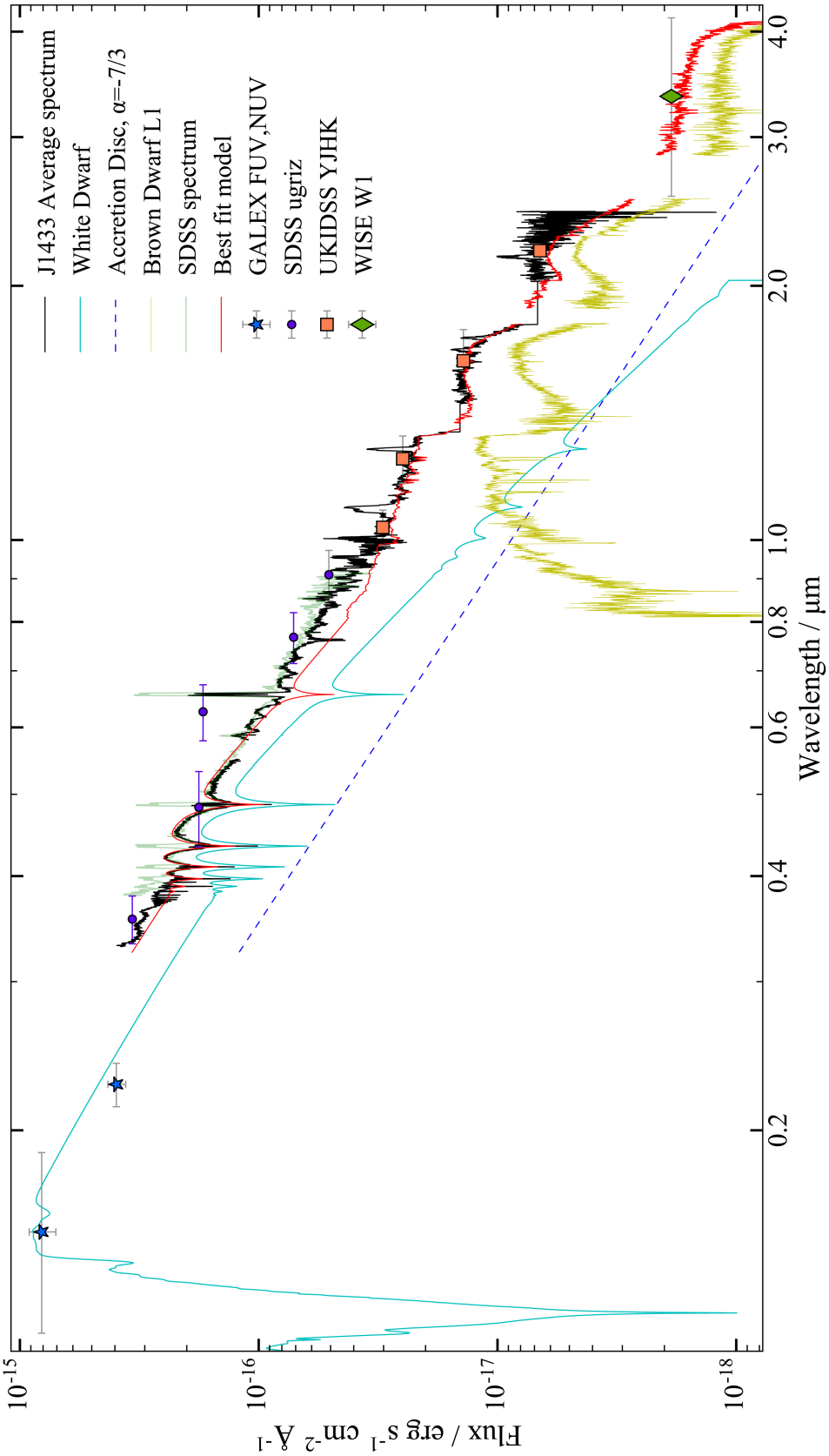

FIGURE 2.5: Spectral energy distribution of SDSS J1433+1011.

SpT	χ^2 (8634 dof)	$\chi^2 - \chi^2_{min}$	χ^2_ν	a	Template
M6	229647.72	221005.73	26.57	0.000	Gl 406
M6.5	152589.54	143947.55	17.66	-0.000	GJ 1111
M8	52521.93	43879.93	6.08	-0.000	Gl 752B
M8	61304.85	52662.86	7.09	0.000	LP 412-31
M9	12451.38	3809.38	1.44	0.334	LHS 2065
M9.5	13915.03	5273.03	1.61	0.330	BRI B0021-0214
L0	8642.00	0.00	1.00	0.372	LHS 2924
L1	8734.46	92.46	1.01	0.425	2MASS J14392836+1929149
L3.5	26971.10	18329.10	3.12	0.523	2MASS J00361617+1821104
L4.5	53496.22	44854.22	6.19	0.578	2MASS J22244381-0158521
L5	51279.96	42637.96	5.93	0.572	2MASS J15074769-1627386
L6.5	70027.67	61385.68	8.10	0.598	2MASS J15150083+4847416
L7.5	78979.53	70337.53	9.14	0.609	2MASS J08251968+2115521
L8	79704.56	71062.56	9.22	0.610	DENIS-P 025503.3-470049.0

TABLE 2.2: Model comparison for best brown dwarf template

2.4 The Donor

In order to further characterise the donor spectrum, I applied a similar fitting process to the one previously described. More specifically, I independently subtracted at each orbital phase the contribution of the WD and the accretion disc fitting only to the UVB range. This fit was then extrapolated to the NIR and subtracted from the observed NIR spectra, yielding a phase-resolved set of *pure*-donor spectra.

2.4.1 Line identifications

Next, I constructed a high S/N donor spectrum by Doppler-shifting the spectra at each phase into the donor's rest frame, using the orbital parameters found in this chapter, and coadded all the available spectra. The result is shown in Figure 2.6. As expected, it revealed clear absorption lines from the secondary star throughout the full NIR spectrum. The broad H_2O molecular bands are clearly present, giving the characteristic global shape of a brown dwarf spectrum. In addition, narrow absorption features are visible in the J band, particularly due to KI, SiI and NaI lines; all of these are clearly broadened due to the high rotational velocity of the donor, $v \sin i$. All these lines are expected in a sub-stellar object with a late-M or early L spectral type (Kirkpatrick et al. 1999; Cushing et al. 2005). The H-band (middle panel of Figure 2.6) is dominated by the broad hydrogen lines from the accretion disc, with slight evidence for FeH molecular bands at 1.95 μm. Due to the low S/N in the K-band (bottom panel of Figure 2.6), the CO band heads are difficult to identify, but there is tentative evidence for the absorption at 2.29352 μm.

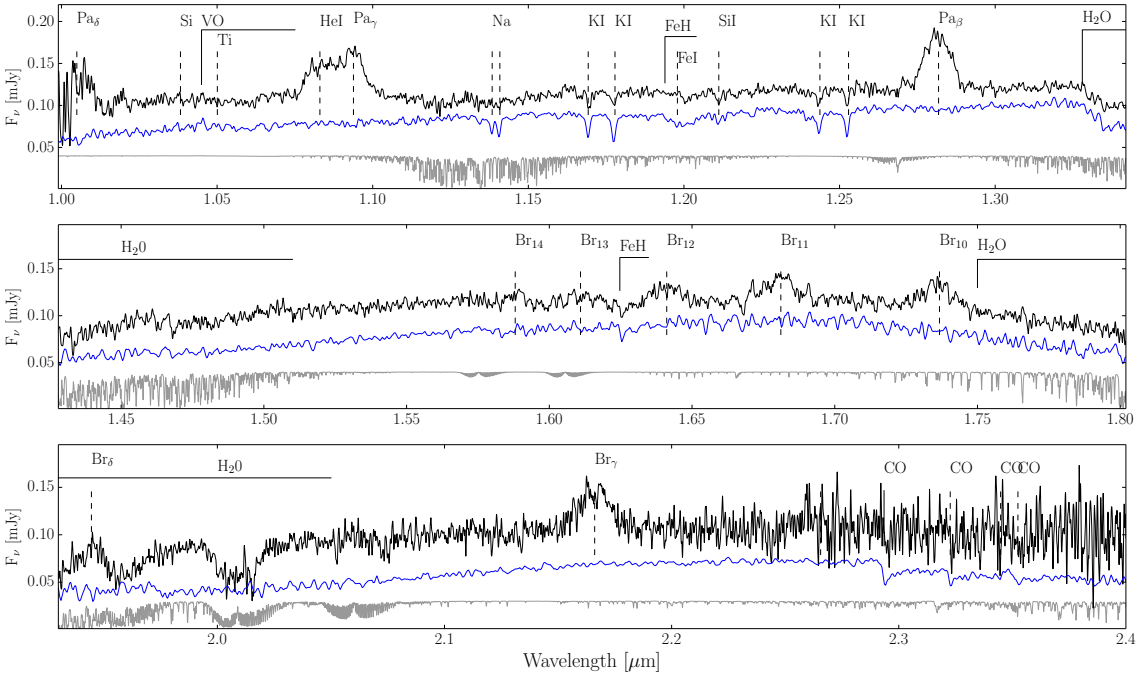

FIGURE 2.6: NIR Average Spectrum of SDSS J1433+1011 in the donor's rest frame. Each spectrum (*black*) was shifted to the donor's rest frame using the K_2 from Savoury et al. (2011), then coadded and median filtered using a 7 pixel box. The donor's absorption lines and molecular bands are identified in the spectrum. HI (Paschen and Brackett series) and HeI emission lines arising from the disc are present throughout the full NIR range. A L1 template spectrum (*blue*) of the best fit brown dwarf and telluric absorption (*gray*) spectrum is shown for reference and offset for clarity.

2.4.2 Dynamics

Close inspection of the NIR spectra revealed modulations of several absorption lines in phase with the donor, as seen in the trailed spectra in Figure 2.7. As shown in the previous section, theses lines arise from the atmosphere of the donor, hence it is possible to retrieve the donor's semi-amplitude, K_2, from these data.

The exposure time of each individual spectrum is equivalent to $\Delta\phi \sim 0.1$ in orbital phase. Thus orbital smearing can significantly alter the line profile of the donor across the orbit, as exemplified in Figure 2.8. Overall, the line will be affected by three processes: orbital smearing, rotational and instrumental broadening. In order to retrieve the rotational velocity, one needs to carefully account for the other two.

For this, I used a high-resolution template spectrum ($R \sim 20,000$, or 15 km s^{-1}) of the closest SpT of the donor, a L0 template (2MASS J0345432+254023, McLean et al. 2007) and focused on the KI 1.243 and 1.252 μm region. This wavelength range is least affected by telluric features and sky lines and should provide the cleanest measurement of K_2. The spectral resolution in the template is small enough ($\sim$15 km s^{-1}) compared to the rotational broadening expected from the tidal synchronisation of the donor ($\sim$ 99 km s^{-1}), that any contribution to the broadened lines will not be of any significance.

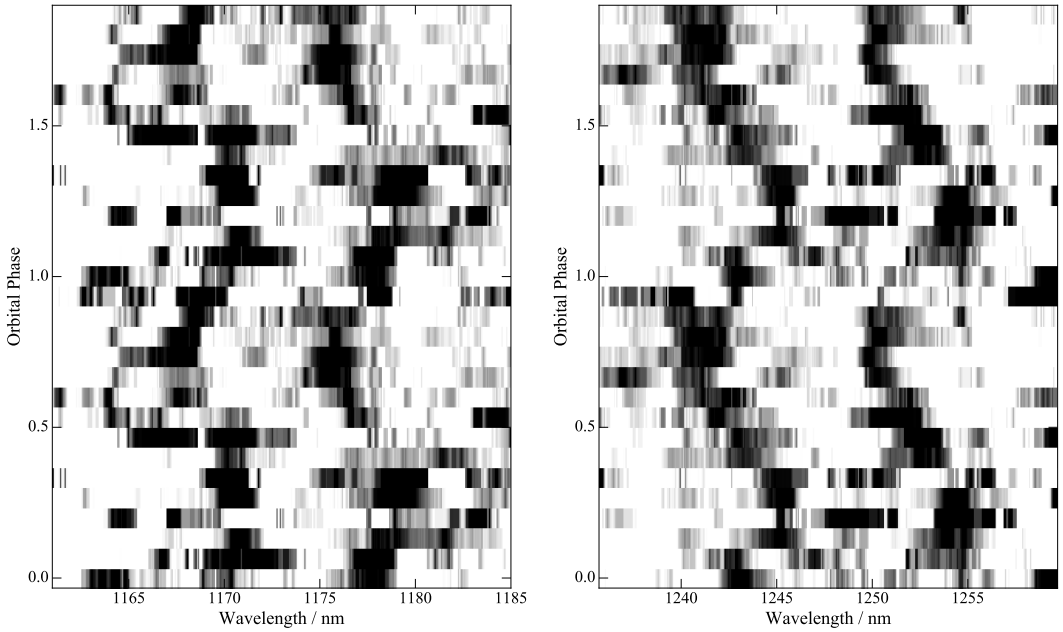

FIGURE 2.7: Trail spectra of absorption lines of the donor. *Left:* the KI doublet 1.1169 and 1.1177 μm. *Right:* the KI doublet 1.2436 and 1.2528 μm

Rotational broadening was accounted for by convolving each template with a Gray profile (Gray 2008) and a linear limb-darkening coefficient of $\mu = 0.6$ (Claret et al. 2012). Orbital smearing was then simulated by constructing an average profile from 15 spectra spaced across the phase range covered by each individual exposure. The template spectra was shifted the corresponding radial velocity to sample the observed exposure in orbital phase. The average of these spectra then provided a unique profile at each orbital phase taking orbital smearing into account. Each template was then convolved with a Gaussian profile ($R \sim 4,000$, or ~ 75 km s^{-1}) to match the resolution of the instrument. Finally, the model spectra was re-sampled to the data wavelength range and dispersion. As seen in Figure 2.8, the dominant observational effect is due to orbital smearing.

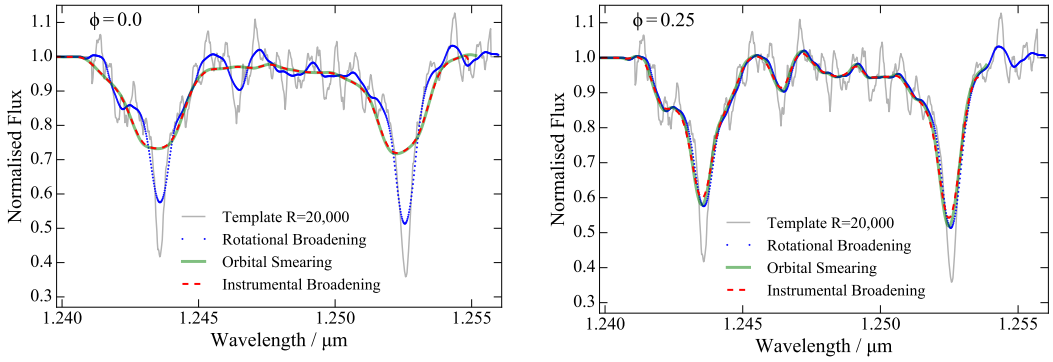

FIGURE 2.8: Profile simulation of KI 1.243 and 1.252 μm at orbital phases 0.0 (*left*) and 0.25 (*right*) after applying rotational broadening of $v \sin i = 100$ km s^{-1}, orbital smearing and instrumental broadening (for $R = 4000$).

Both the templates and observed donor spectra were continuum-normalised by fitting a straight line to the median flux values outside the regions of interest, which were devoid of absorption lines. I then performed a grid search in which the template spectra were fit to the observed donor spectra at all orbital phases. This fit involved three free parameters: rotational broadening, $v \sin i = 50$ to 200 km s^{-1}, systemic velocity $\gamma = -100$ to 100 km s^{-1}, and the donor semi-amplitude $K_2 = 350$ tp 650 km s^{-1}; all three were covered in 5 km s^{-1} steps. At every point in the grid, I reconstructed a spectra for every orbital phase that our data set covered. This allowed me to fully use the information in every spectra. The fit results are shown in Figure 2.9. The best solution is found to be $K_2 = 499 \pm 15$ km s^{-1}, the rotational broadening of the donor is $v \sin i = 131 \pm 46$ km s^{-1}, and the systemic velocity is $\gamma = -42 \pm 8$ km s^{-1}. The K_2 and $v \sin i$ values are consistent with previous estimates of Savoury et al. (2011) and (Littlefair et al. 2013). However, the systemic velocity is significantly different from that estimated by Tulloch et al. (2009) from Hα, 75 ± 10 km s^{-1}. The quoted 1σ confidence intervals were obtained by projecting the confidence ellipses over every parameter.

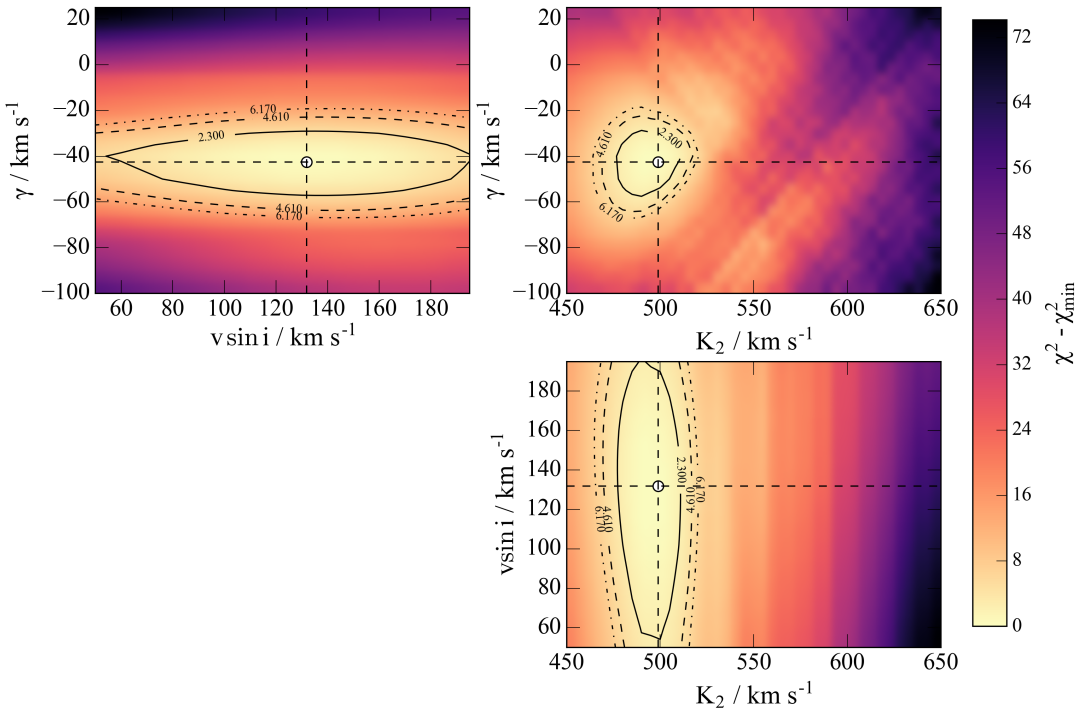

FIGURE 2.9: $\Delta\chi^2$ space for the orbital parameters of the donor in SDSS J1433+1011. The contours show the 1, 2 and 3-σ confidence levels. The χ^2_{min} is marked as a circle.

2.4.3 Irradiation of the donor

Littlefair et al. (2008) found that the radii of CV donors were $\simeq 10\%$ larger than the model predictions. One possible mechanism to explain this discrepancy (an enhanced mass transfer at short orbital periods) is bloating of the donor's atmosphere due to

irradiation from the WD and/or inner disc. The irradiation essentially blocks the outgoing internal energy, causing the star to bloat. In sub-stellar models, irradiation of hot Jupiters suggests that photospheric temperatures can be increased by an order of magnitude compared to isolated objects, with significant effects on the planet's radius and atmospheric structure (Arras & Bildsten 2006). Similar effects may occur in higher mass brown dwarfs (Hubeny et al. 2003), where tentative evidence has been observed in post–common envelope binaries (such as WD+BD systems, Casewell et al. 2013). The incident flux is processed in the day-side of the donor's atmosphere, increasing the photospheric temperature. This can be observed as an apparent earlier type spectrum at $\phi = 0.5$ than at inferior conjunction. Therefore, it is possible to observe temperature variations at distinct phases by using spectral classification techniques as proxies for temperature.

A robust and widely used method to measure the spectral type of BDs is via NIR water band indices which change monotonically with SpT for late-M to T-type stars (McLean et al. 2003). I used a slightly modified index (defined as $H_2O^a = \langle F_{\lambda=1.318\mu m}\rangle / \langle F_{\lambda=1.340\mu m}\rangle$ ratio with a 5 nm width) to avoid noisy areas, mainly due to bad telluric removal, and emission lines. Due to the low S/N of the individual spectra, the telluric removal created artefacts in the spectra. I identified these regions and masked them before shifting each spectrum to the donor's rest frame. Afterwards, I obtained the median flux in each small band when grouping the data of all spectra inside one of the eight orbital phase bins. In this way, I could propagate the errors without compromising the number of data points inside each water-band (since individual water-band measurements consisted of 9 pixels). Errors were estimated by bootstrapping 1000 copies of the original spectra and performing the procedure described above for each copy. The results are shown in the middle panel of Figure 2.10. The water-band light curve shows a modulation as a function of orbital phase. The average spectral type is ∼L1 type when observing the night-side of the donor (consistent with the full SED fit) while an earlier SpT at ϕ =0.5. This shows that there is an increase in the local temperature of the donor as seen in the day-side facing the WD. An independent measurement of this difference in temperatures between the hemispheres can be obtained from their broad-band light curves. Taking the clean phase-resolved donor spectra, I performed synthetic photometry over the J-band, masking any emission lines (by linearly interpolating over the masked region). The resulting light curves show a clear double modulation, caused by the combination of the distorted Roche-lobe filling shape (ellipsoidal) and the temperature difference between the two sides of the donor (irradiation), as shown in the bottom panel of Figure 2.10.

The combination of these two measurements allows me to recover the most likely temperature distribution across the donor. I used the eclipse modelling software ICARUS[7] (Breton et al. 2012) to generate synthetic spectra of the irradiated donor. For this, I once again employed the empirical brown dwarf template sequence described in 2.3.2

[7] https://github.com/bretonr/Icarus

and in Appendix A. I favoured the use of empirical templates over state-of-the-art BD atmosphere models (such as CIFIST2011–2015, Allard et al. 2012; Baraffe et al. 2015), since these models do not fully replicate the spectroscopic features used as empirical calibrators of spectral type (and therefore temperature), in particular, the water band ratios[8].

Each model in ICARUS is characterised by two parameters: the irradiating luminosity absorbed by the donor, and the intrinsic luminosity it would produce in the absence of irradiation. The calculations assume that all of the irradiating flux absorbed at a given point on the surface of the donor is re-emitted locally; any effect of the fast rotation of the donor on the temperature distribution is neglected (which could affect the atmospheric dynamics, Showman & Kaspi (2013)). For each parameter pair, I calculated the resulting temperature distribution across the donor and predicted the observed spectrum at each orbital phase. I then performed synthetic photometry on the models and calibrated them on AB magnitudes. In order to calculate the water-band ratios at each phase, every model spectrum was shifted to the rest-frame of the system.

The generation of phase-resolved synthetic spectra made the evaluation of parameter space in the light-curve modelling computationally expensive. In order to keep the computational cost under control, I performed a grid search on a pre-computed set of models to obtain the best-fit parameters that simultaneously described the broad-band photometry and water-band light curve data by minimising the goodness-of-fit parameter:

$$\chi^2 = \sum \left(\frac{R_i - R_{model,i}}{\sigma_{R,i}} \right)^2 + \sum \left(\frac{m_j - m_{model,j}}{\sigma_{m,j}} \right)^2 \quad , \tag{2.5}$$

where R_i and $\sigma_{R,i}$ are the water band ratio and its 1σ error; m_j and $\sigma_{m,j}$ are the broadband J-band AB magnitudes and its 1σ error; $R_{model,i}$ and $m_{model,j}$ are the model water-band ratio and magnitude, respectively. The absorbed irradiating and intrinsic luminosities are not directly observable, but they determine the day-side and night-side temperatures, respectively, which are observable. The χ^2-landscape generated was used to estimate the average day- and night-sides of the donor (making use of Equations B.8 and B.9, respectively) along with their uncertainties by using a Markov Chain Monte Carlo method (MCMC, using the Metropolis-Hastings algorithm). In this, I adopted uniform priors for both parameters, defined as:

$$\begin{aligned} T_{\rm day} &\sim U(1600 : 3000) \\ T_{\rm night} &\sim U(1600 : 3000) \end{aligned} \tag{2.6}$$

The results are shown in Figure 2.11. I find $\langle T_{\rm night} \rangle = 2344^{+11}_{-10}$ K and $\langle T_{\rm day} \rangle = 2401^{+7}_{-7}$ K, with a maximum difference between the hottest and coolest parts of the surface being

[8] A new set of sub-stellar atmosphere models were published after the initial calculations presented in this chapter. I verified that the calibration between my empirical sequence and the theoretical models were consistent. I made used of only the photometric estimates that returned similar values of the results presented in this chapter.

~ 200 K. Errors quoted represent the 1σ confidence levels on the marginal distributions. Since the code allows me to separate the internal and irradiated component, I was able to find the total intrinsic luminosity of the donor by integrating $F_{int,j}$ over all the surface elements. This gives a total internal energy output (without the effects of irradiation) of $L_{int} = 3.1 \pm 0.1 \times 10^{-4} L_{\odot}$.

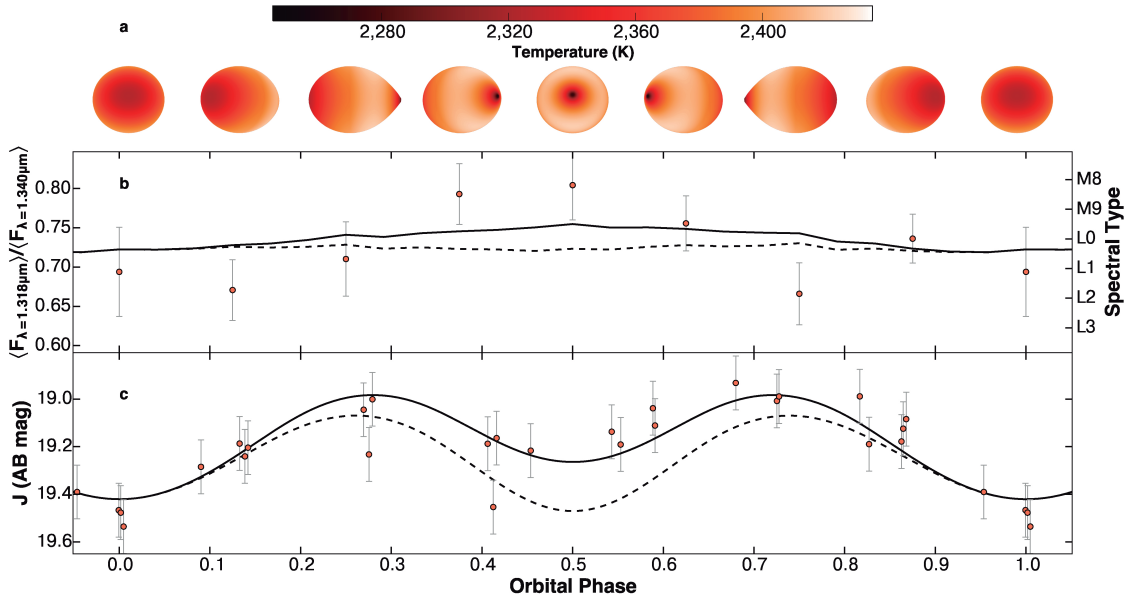

FIGURE 2.10: Ellipsoidal and irradiation effects associated with the substellar donor in SDSS J1433+1011. *Top* : Temperature distribution of the atmosphere of the donor as a function of phase. *Middle*, 1.3-μm water-band depth measurements (circles) with the best-fit model (solid line) and a model with no irradiation source (dashed line) for comparison. *Bottom*, time-resolved J-band photometry (circles) after subtracting the contributions from the white dwarf and the accretion disc. Lines represent the same models as in the middle panel. Error bars in b and c represent 1σ confidence intervals.

It is important to note the small statistical error on the individual parameters, which may possibly be underestimated. Errors on the individual measurements of the spectra were folded through via bootstrapping in the fitting procedure, therefore, systematic errors might arise from two other sources: the flux calibration (discussed in Section 2.1.1) and the calibration of the empirical sequence. These two effects will change the overall flux scale and therefore change the derived surface temperature of the donor. However, the observed difference between the day-side and night-side fluxes is statistically significant and allowed me to estimate the reprocessing efficiency of the donor[9]. This efficiency is usually parametrised via the bolometric (Bond) albedo, A_B, which is the fraction of the incident irradiation flux that is not reprocessed, but reflected back into space. This is possible since the irradiation source and binary parameters are known from eclipse modelling (see Section 2.3.1). The bolometric luminosity emitted by the WD,

[9]Errors on the absolute flux scale will influence this difference in a minor way since both sides of the donor's effective temperature are correlated through the empirical templates.

$L_{WD} = 2\pi\sigma R_1^2 T_{WD}^4 = 2.65 \pm 0.16 \times 10^{-3}\ L_\odot$, is spread across the day-side of the donor, producing an irradiating flux of

$$F_{\mathrm{irr},j} = \frac{4\pi R_{\mathrm{WD}}^2 \sigma T_{\mathrm{WD}}^4}{4\pi d_j^2} A_{\mathrm{proj},j}(1 - A_B) \ , \tag{2.7}$$

on a given surface element j, where d_j is the distance of the surface element to the WD. $A_{\mathrm{proj},j} = A_j \cos(\chi)$ is the projected area of the surface element on the donor, where χ is the angle between the normal of the surface and vector pointing to the irradiating source. In order to estimate the values of the albedo numerically, I used the Markov-chains of $F_{\mathrm{irr},j}$ generated in the global fit and then used the known system parameters to estimate A_B from Equation 2.7. I imposed a restriction on the physically allowed values of the albedo, so $0 \leq A_B \leq 1$. I found an upper limit at 2σ of $A_B < 0.54$, as shown in Figure 2.11. This low value is consistent with measurements found in hot Jupiters in this atmospheric temperature regime (Perez-Becker & Showman 2013), as well as with low-mass stars in accreting white dwarf binary systems (Barman et al. 2004).

2.4.4 Circulation efficiency

The measurement of the albedo, as usually interpreted, provides the efficiency of the atmospheric winds to transport energy from the day to the night side. If the time scale for this lateral transport carried by the winds is smaller than the time scale to reach local radiative equilibrium, then energy will be redistributed across the surface of the sub-stellar object. On the contrary, if local radiative equilibrium is faster, then the object will reprocess the energy and the maximum temperature difference would be observed between hemispheres (Perez-Becker & Showman 2013). In practice, it is expected that the two time-scales might be comparable, so both lateral transport and local reprocessing might be occurring simultaneously. As shown inFigure 2.10, SDSS J1433+1011 fits the data acceptably, suggesting that redistribution is inefficient in the atmosphere of the donor.

However, it is possible to expand the model in order to quantitatively constrain the fraction of the irradiation flux that is transported laterally. The modified energy balance equations for each individual surface element now assumes that a certain fraction of the incident flux is redistributed equally across the entire surface of the object. Then, the average day-side temperature is given by:

$$\sigma\langle T_{\mathrm{day}^4}\rangle = \frac{\sum_{j,\mathrm{day}} F_{\mathrm{int}_j}}{\sum_{j,\mathrm{day}} A_j} + \epsilon(1 - A_B)\frac{\sum_{j,\mathrm{day}} F_{\mathrm{irr}_j} A_j}{\sum_{j,\mathrm{day}} A_j} \ , \tag{2.8}$$

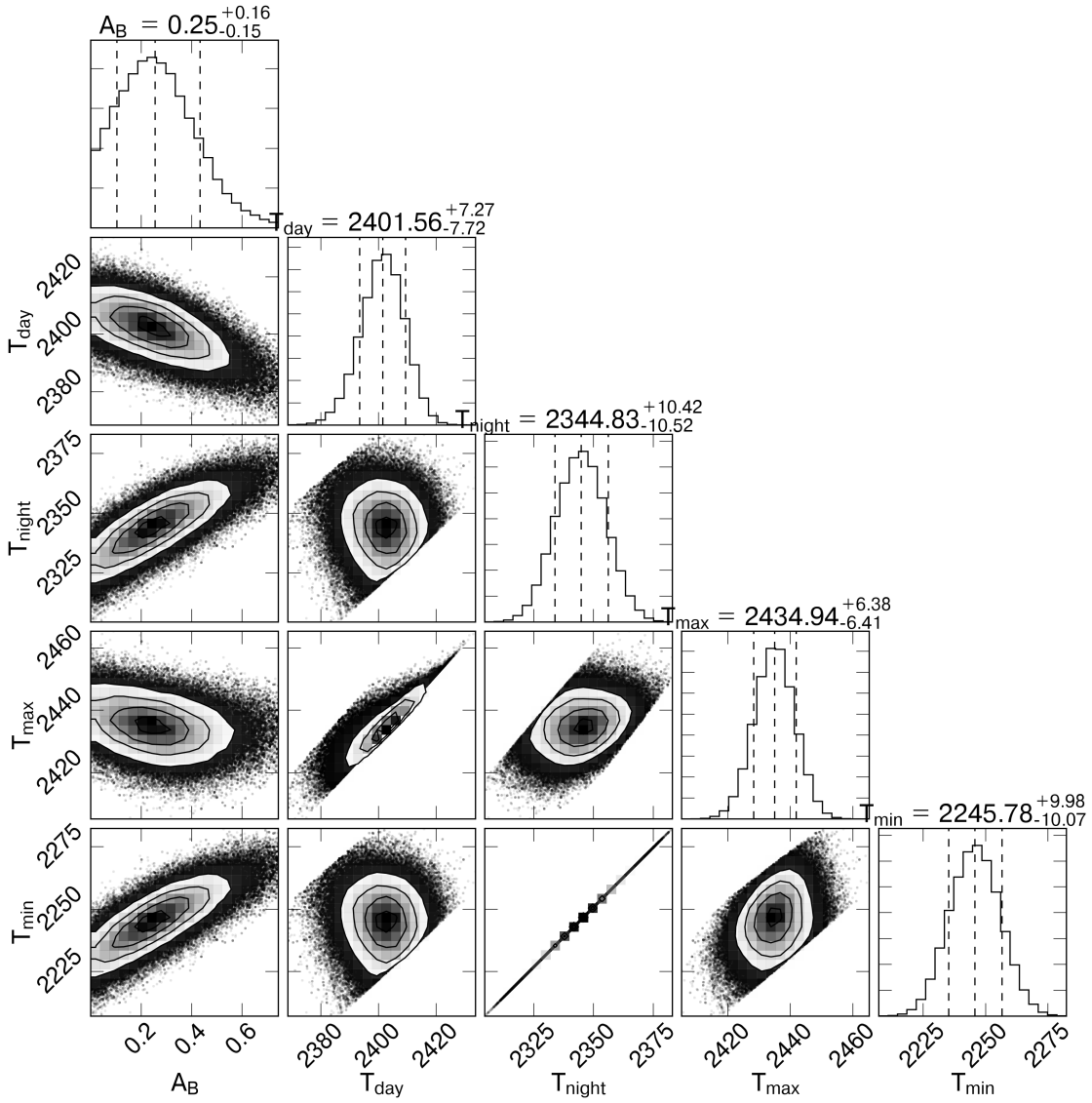

FIGURE 2.11: Posterior probability distributions for atmospheric parameters T_{night}, T_{day} and Bond albedo A_B in SDSS J1433+1011. The contours show 0.5, 1, 1.5 and 2σ. For the individual parameter the marginal distributions are shown as histograms with the 0.5 percentile and the 1-σ (*dashed lines*).

where ϵ is the redistribution efficiency i.e the fraction of the irradiating flux that is reprocessed non-locally. Conversely, for the night-side, we have:

$$\sigma\langle T_{\text{night}^4}\rangle = \frac{\sum_{j,\text{night}} F_{\text{int}_j}}{\sum_{j,\text{night}} A_j} + (1-\epsilon)(1-A_B)\frac{\sum_{j,\text{night}} F_{\text{irr}_j} A_j}{\sum_{j,\text{night}} A_j} \quad . \tag{2.9}$$

By subtracting Equation 2.8 from Equation 2.9, it is possible to find the difference in flux between each side (an observable quantity directly from the fitting procedure in previous sections):

$$\sigma\langle T_{\text{day}^4}\rangle - \sigma\langle T_{\text{night}^4}\rangle = \sigma\left(\langle T_{\text{day}^4}\rangle - \sigma\langle T_{\text{night}^4}\rangle\right)|_{\epsilon=0} - \epsilon(1-A_B)\frac{\sum_{j,\text{day}} F_{\text{irr}_j} A_j}{\sum_{j,\text{day}} A_j} \quad , \tag{2.10}$$

where $\left(\sigma\langle T_{\rm day^4}\rangle - \sigma\langle T_{\rm night^4}\rangle\right)|_{\epsilon=0}$ is the flux difference of the equivalent model without any redistribution (i.e. $\epsilon = 0$) obtained in Section 2.4.3. Finally, I estimated the redistribution efficiency needed to reproduce the observed day-side and night-side temperature difference. I evaluated the parameter space by performing a MCMC procedure, which produced a family of allowed solutions as a function of A_B and ϵ, shown in Figure 2.12 as the red contours. In general, the reprocessing efficiency as well as the albedo are constrained to be low, with a 2σ upper limit of < 0.54, on both parameters. In the limit of $\epsilon = 0$, we recover the A_B distribution presented in the previous section.

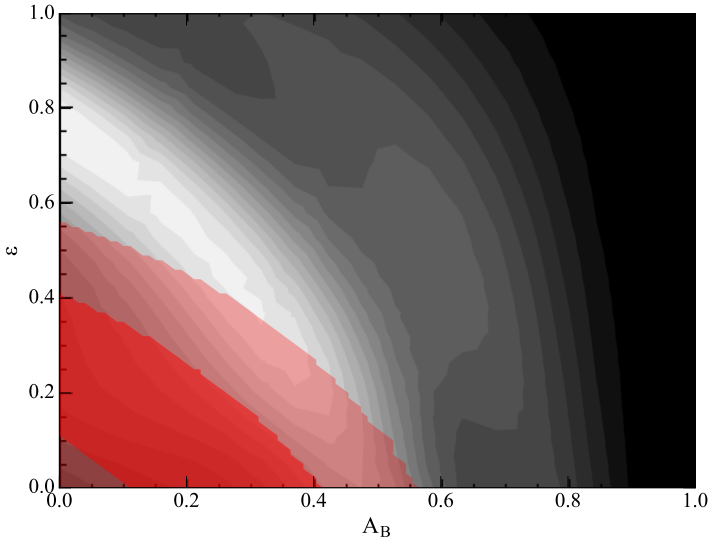

FIGURE 2.12: Redistribution efficiency limits for the irradiated sub-stellar donor. Allowed family solutions of redistribution efficiencies as a function of Bond albedo are shown. The red contours represent the 1 and 2-σ confidence levels. The grey-scale contours represent the distribution for irradiated planets, reproduced from Cowan & Agol (2011).

The results described above are consistent with previous studies of extremely irradiated hot-Jupiters, whose energy budget is dominated by the irradiation produced by the host star. For example, Cowan & Agol (2011) found a 1σ upper limit of $A_B < 0.35$, by consistently analysing a sample of well-studied exo-planets (shown as greyscales in Figure 2.12). Similarly, the efficiency of heat redistribution was also found to be low. However, there are a few systems ($< 10\%$) where, in order to reproduce the observed day vs. night-side temperature difference, it is necessary to invoke high recirculation efficiencies (Cowan & Agol 2011).

2.5 The accretion disc

The SED of the accretion disc in SDSS J1433+1011 appears to be well described by a power law, as shown in Figure 2.5. However, on close inspection, the fit falls short around

$\sim$ 8000 Å. A possible explanation is that the disc SED contains a contribution from an optically thin region, possibly the hot spot. In order to test this idea, I built on the work by (Savoury et al. 2011), who were able to isolate the disk and hotspot contributions[10]. u/g and g/r flux ratios are shown in Figure 2.13 where I compare them to the flux ratios predicted by optically thin hydrogen slabs in local thermodynamical equilibrium (LTE). These were generated by SYNSPEC[11]. The grid of slab models was constructed by varying the column density, $\log(N/cm^{-2}) = 20 - 24$ in steps of $\Delta \log(N) = 0.5$, and the temperature of the plasma, $T = 4000 - 12000$ K in 1000 K steps. Then, I performed synthetic photometry on the resulting spectra in three different Sloan filters: u', g' and r'. Savoury et al. (2011) solutions for the hot spot and accretion disc move around their corresponding loci throughout the full orbit. At these densities and temperatures, however, the slab spectra produce a sharp Balmer jump in emission, not observed in the data. Although part of the emission around $\sim$ 9000Å can be accounted by the higher-order Paschen lines, the continuum still falls short between 7000-9000 Å, in conflict with the observed SED.

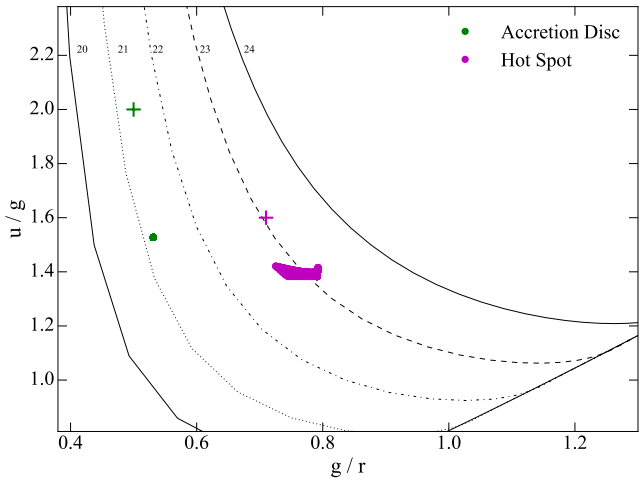

FIGURE 2.13: Flux ratios for the accretion disc and hot spot inferred from eclipse modelling. The colours represent the solutions for the accretion disc (*green*) and the hot spot (*red*). The *crosses* show the values calculated by (Littlefair et al. 2008) and the updated fit by (Savoury et al. 2011) (*circles*).

2.5.1 Disc lines

In order to analyse the optical emission lines of the accretion disc in SDSS J1433+1011, I subtracted the contribution of the WD and the power-law model from each spectrum. Then, I normalised to the continuum by fitting a 3rd degree polynomial to each UVB and

[10] The best-fit light curves for SDSS J1433+1011 were provided by S. Littlefair priv. comm.

[11] A sub-routine in IRAF. IRAF is distributed by the National Optical Astronomy Observatories, which are operated by the Association of Universities for Research in Astronomy, Inc., under cooperative agreement with the National Science Foundation.

VIS spectrum individually. The average optical spectrum, as well as line identifications, is presented in Figure 2.14. The WD subtraction allows a more detailed view of the emission line profiles of the disc, since most of them were buried beneath the broad WD absorption features. HI recombination lines dominate most of the spectra, along with weaker HeI features. All of these lines are broad and double peaked, with very narrow dips or absorption components in the core, well below the continuum level. Surprisingly, this narrow feature is also shared by CaII 3933 Å, ruling out an incorrect removal of the WD atmosphere as an explanation for the depth of these features. Therefore, I suggest these components are formed by absorption in the atmosphere of the accretion disc. This effect has been observed in other systems with high inclinations e.g. Friend et al. (1988).

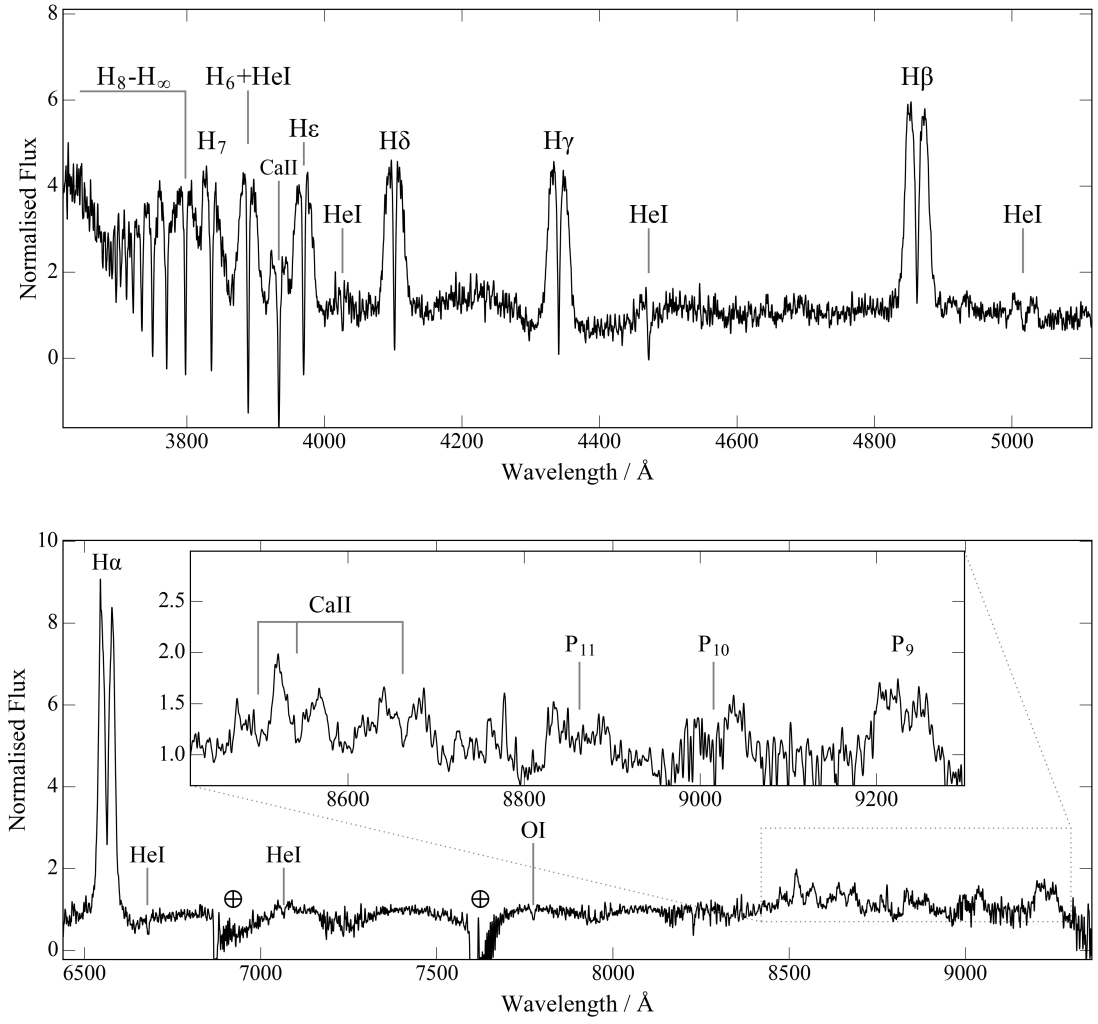

FIGURE 2.14: Average optical spectrum of the accretion disc lines in both X-Shooter arms UVB (*top*) and VIS (*bottom*). Telluric features are marked with ⊕.

2.5.2 The OI triplet

The neutral oxygen triplet (7771.9, 7774.2 and 7775.4 Å) has been observed in CVs showing a wide range of behaviours, from emission to absorption and, in some cases, a combination of both (Friend et al. 1988). In general, this feature is observed in outburst. In SDSS J1433+1011, the line is observed primarily in absorption and modulated on the orbital period on the phase of the primary, as shown in the trailed spectra plotted in Figure 2.15. The triplet is not individually resolved but blended into a single feature, reminiscent of the low-velocity absorption cores in Section 2.5.1. For high inclination systems, a combination of emission/absorption has been observed in systems such as Z Cam (Wade & Horne 1988) and V2051 Oph (Friend et al. 1988), a feature not observed in the case of SDSS J1433+1011.

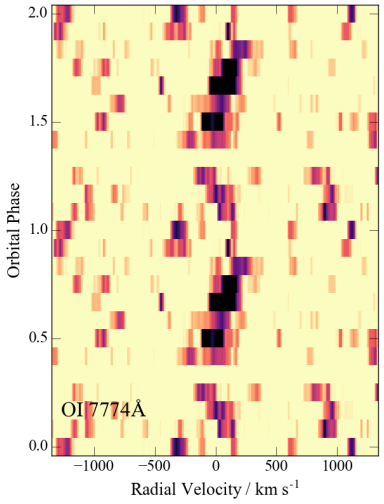

FIGURE 2.15: Trailed spectra of the OI triplet.

2.5.3 Doppler Tomography

Doppler tomography is a useful method to study the structure of the accretion disc by de-constructing the orbital variations of the emission lines (Marsh 1988; Boffin et al. 2001). I have performed tomography using the Spruit (1998) software [12] which is based on the maximum entropy method. I used only the highest signal to noise lines for this purpose: the lower order hydrogen Balmer lines and λ5015 HeI. Higher order Balmer lines were difficult to analyse due to their intrinsic width and proximity to nearby lines. An example tomogram is shown in Figure 2.16.

All tomograms reveal a similar emission pattern, a smooth structure of the accretion disc, with velocities between $\sim 650-1200$ km s^{-1}. Superimposed, there is additional emission arising from different regions of the velocity space. The hot spot is the brightest of these

[12] Version 2.3.1, http://www.mpa-garching.mpg.de/~henk

asymmetries, observed as the feature at V_x,$V_y \simeq$ (-600,+400) km s^{-1}, intersecting the ballistic trajectory. The hot spot is common in both HI and HeI. The emission of the disc's outer edge is consistent with the tidal-limited radius, $r_d(max)$, given by(Paczynski 1977):

$$\frac{r_d(max)}{a} = \frac{0.60}{1+q}, \quad 0.03 < q < 1 \quad . \tag{2.11}$$

For SDSS J1433+1011 parameters, the disc should have a radius of $r_d(max) = 0.331$ $R_\odot$. At this radius, the expected Keplerian velocity is $v = (GM_1/r)^{1/2} = 611$ km s^{-1}. This value is consistent with estimates from the Doppler tomography (due to the position of the hot-spot and the outer disc as seen in Figure 2.16) as well as via eclipse-modelling (650 km s^{-1}, Savoury et al. 2011). To emphasize this emission, I constructed an azimuthal average and subtracted it from each tomogram (shown as the right panel of Figure 2.16). Unfortunately, all tomograms show other clear and bright artefacts (seen as radial spikes and blobs) most likely due to the orbital smearing and phase under-sampling (Marsh & Horne 1988). This prevented me from reliably interpreting any other emission pattern from the tomogram.

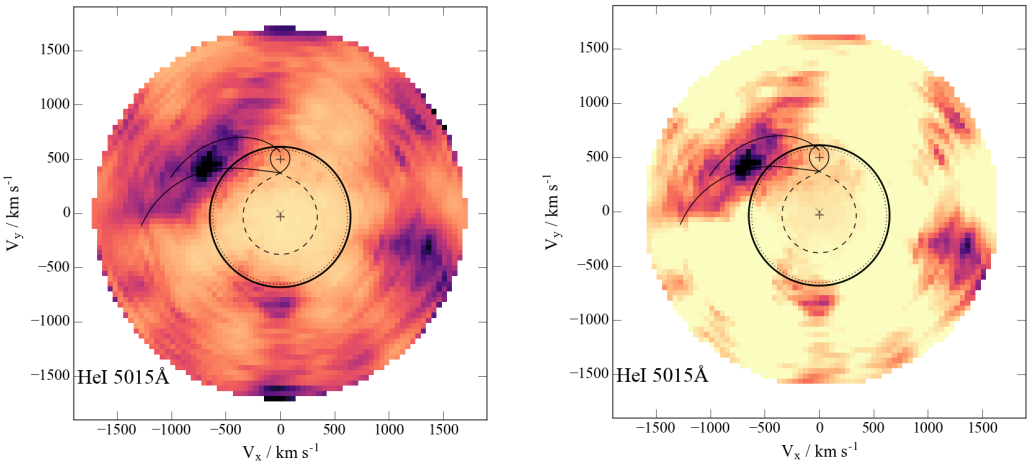

FIGURE 2.16: Doppler tomograms of HeI 5015 Å. The right box has been subtracted by the azimuthal average to enhance any asymmetries in the structure of the disc. The Roche lobe surface of the donor (continuous line) and the primary (dashed line) were calculated using the orbital parameters presented in Table 2.3. Also, the tidal-limited radii (*bold line*) and the 2:1 resonance (*dotted line*) are shown. The Keplerian and ballistic trajectories are marked as the upper and lower curves, respectively. The crosses (from top to bottom) are the velocities of the donor, the common center of mass and the primary star.

2.6 Orbital Parameters

The radial velocity measurement obtained in Section 2.4.2 allows me to determine the parameters of the system by using the mass functions (Equation 1.8). The measurements of both semi-amplitudes immediately yields the mass-ratio of the system:

$q = M_2/M_1 = K_1/K_2 = 0.068 \pm 0.008$. For this mass ratio, the occurrence of white-dwarf eclipses alone sets a lower limit on the inclination of $i > 80°$ (Chanan et al. 1976). We can then use the mass function of the secondary from Equation 1.8, $f_2 = P_{orb}\, K_1^3/(2\pi G) = M_2 \sin^3 i\, q^2/(1+q)^2$ to set a purely dynamical 2σ upper limit on the mass of the donor star, $M_2 < 0.071$ M$_\odot$. My estimate of $v \sin i$ also allows me to deter-

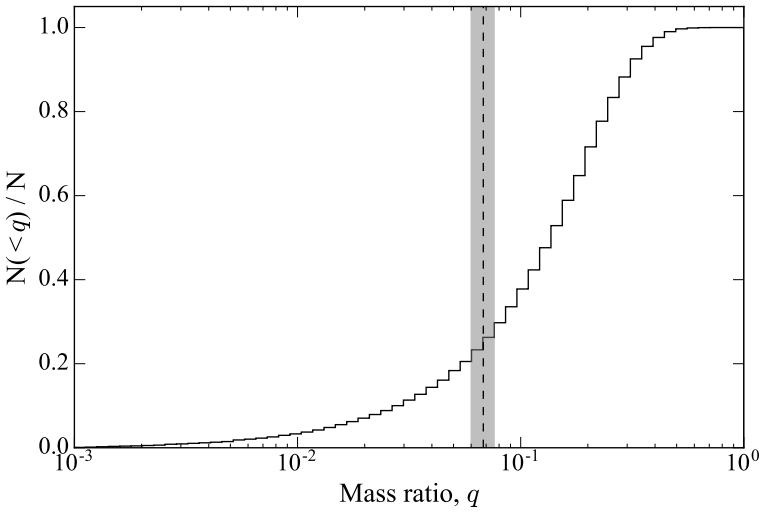

FIGURE 2.17: Mass ratio measurement via a) $K_2/v \sin i$ (black line) and b) K_2/K_1 (dashed line). Both measurements are consistent.

mine an independent measure of q, via Equation 1.10 and using the Roche-lobe radius approximation (Equation 1.5). In Figure 2.17, I show a cumulative distribution for the possible values for q, estimated via a Monte-Carlo simulation assuming Gaussian distributions for K_2 and $v \sin i$. Unfortunately, the large uncertainty on $v \sin i$=131 $\pm$ 46 km s^{-1} (heavily affected by orbital smearing) dominates the error budget. However, both values are consistent within the uncertainties as well as with the direct estimate from eclipse modelling, $q = 0.0661 \pm 0.0007$ (Savoury et al. 2011). Thus, it is possible to determine the values of the mass of both components by using the inclination measurement of $i = 84.36 \pm 0.05°$ Savoury et al. (2011). Errors were again estimated via a Monte Carlo simulation assuming all measurements are Gaussian distributed with a standard deviation equivalent to their respective error. The resulting dynamical parameter estimates for SDSS J1433+1011 are summarised in Table 2.3.

2.7 Discussion

In this chapter, I have presented time-resolved spectroscopic observations of SDSS J1433+1011. The clear NIR detection of the companion has allowed me to directly determine –for the first time– the sub-stellar nature of a donor in a CV. This discovery provides a validation of evolutionary models that suggested that donors could survive

Parameter	unit	Value			Reference
K_1	km s^{-1}	34	$\pm$	4	(Tulloch et al. 2009)
K_2	km s^{-1}	499	$\pm$	15	This thesis
q		0.068	$\pm$	0.008	This thesis
γ	km s^{-1}	-41	$\pm$	0.03	This thesis
i	$^\circ$	84.36	$\pm$	0.05	(Savoury et al. 2011)
$v \sin i$	km s^{-1}	131	$\pm$	46	This thesis
T_1	K	13,200	$\pm$	400	This thesis
T_2	K	2,400	$\pm$	10	This thesis
M_1	$M_\odot$	0.81	$\pm$	0.07	
M_2	$M_\odot$	0.054	$\pm$	0.007	
a	$R_\odot$	0.570	$\pm$	0.016	
R_L	$R_\odot$	0.105	$\pm$	0.004	

TABLE 2.3: Orbital parameters for SDSS J1433+101133.

the transition to the sub-stellar regime. Furthermore, the spectroscopic signal is in remarkably good agreement with that produced by field brown-dwarfs. I will now discuss these results in the larger context of CV evolution and of the physics of (sub-)stellar atmospheres.

2.7.1 Does a sub-stellar donor mean a period bouncer?

SDSS J1433+1011 lies in a very interesting part of the evolutionary track of CVs, close to where the period minimum has been empirically located at $P_{min} = 82.4 \pm 0.7$ min (Gänsicke et al. 2009). Despite the difficulty in establishing whether CVs in this region are pre- or post-bounce systems (where $\dot{P} \simeq 0$), one firm conclusion that arises from this work is that all period bouncers should have spectral types later $\gtrsim$L0 (also suggested in Knigge et al. 2011). However, harbouring a brown-dwarf donor does not guarantee that the system has become a period bouncer. The donor mass calculated in Section 2.6, clearly demonstrates that the donor has been a sub-stellar object for quite some time. Taking a typical mass transfer rate of $\sim 5 \times 10^{-11}$ $M_\odot$ yr^{-1}, the system has been a sub-stellar object for around ~ 400 Myr. Therefore, it would be crucial to find systems close to the sub-stellar regime in order to find where the exact transition occurs, e.g PHL 1445 (McAllister et al. 2015).

2.7.2 Evolved to or born as a sub-stellar donor?

The donor star in SDSS J1433+1011 must have successfully undergone the transition from the stellar to the sub-stellar regime. The alternative – that the secondary was born as a brown dwarf – is extremely unlikely. First, extreme mass-ratio binary systems containing very low-mass objects are intrinsically rare (Burgasser et al. 2007). The

observed distribution of stellar mass ratios favours binaries of either similar masses ($M \gtrsim 0.1$ M$_\odot$) or planetary companions ($M \lesssim 0.01$ M$_\odot$) with almost a complete void of brown dwarf companions, often referred to as the brown dwarf desert (see Fig. 5 in Grether & Lineweaver 2006). Limits to this brown dwarf fraction have been found to be $\lesssim 0.5 - 1.0\%$ as opposed to $11 \pm 3\%$ for solar-mass companions, at the same orbital separation (Grether & Lineweaver 2006). In principle, magnetic fields and turbulent fragmentation might produce proto-stellar cores down to 0.01 M$_\odot$ (Jumper & Fisher 2013). However, this scenario typically produces systems with high multiplicity. These are intrinsically unstable and will therefore most likely eject the smallest components i.e. brown dwarfs.

Second, the mass of the accreting white dwarf in J1433, $M_{WD} = 0.80 \pm 0.07$ M$_\odot$, is exactly in line with the mean white dwarf mass of known AWD systems. This mass is typical throughout the full orbital period distribution of CVs (Zorotovic et al. 2011), but is significantly higher than the average mass of isolated white dwarfs ($\langle M_{WD} \rangle \simeq 0.6$ M$_\odot$, Kleinman et al. 2013; Kepler et al. 2015). It is also higher than the mass of any known primary in a white dwarf-brown dwarf binary system (Nordhaus & Spiegel 2013).

Third, CVs born with sub-stellar donors would be expected to populate a wide range of orbital periods below P_{min} (Politano 2004). As such systems evolve, the donor will fill its Roche lobe below P_{min} and start evolving towards longer periods. Therefore, if this channel was dominant in creating CVs with sub-stellar companions, we should expect this population to cover a range of orbital periods less than P_{min}. BPS suggest, that at most, only a small fraction (3%) of all CVs should come through this channel. Recent evidence of systems just short of the period minimum, PHL 1225 (McAllister et al. 2015), SDSS J103533.03+055158.4 (Littlefair et al. 2008; Savoury et al. 2011) and SDSS J1433+1011 itself, have raised questions regarding this brown dwarf desert. However, all three systems are well within the scatter of P_{min}. If this scenario was dominant, we would expect to see systems well below $\lesssim 76$ min. However, we observe a sharp cut-off in the P_{orb} distribution e.g. Figure 1.6. Indeed, the only other CV with a sub-stellar donor and an orbital period well below P_{min} has been shown to be a low-metallicity object in the Galactic halo (Uthas et al. 2011), rather than a system born with a brown dwarf secondary. Thus, the donor in SDSS J1433+1011 appears to have evolved from a larger initial mass and survived the stellar to sub-stellar transition.

2.7.3 A test case for sub-stellar atmospheres

The possibility of retrieving the atmospheric parameters of donors in systems similar to SDSS J1433+1011, provides an opportunity for testing theoretical models of sub-stellar objects in a previously unexplored region of parameter space. In order to see this, Figure 2.18 shows the location of different types of sub-stellar and planetary objects in the

2D parameter space defined by their intrinsic flux and the irradiating flux they are subjected to (Showman 2016). In most hot Jupiters, the external irradiation overwhelms any internal heat flux (top left corner in Figure 2.18). In a similar way, the secondaries in black widow and redback systems are overwhelmed by the intense emission of the pulsar wind. Therefore, the emitted spectrum of the companion i.e. the energy balance in their atmosphere, is dominated by the external incident flux. On the other hand, the atmospheres of isolated brown dwarfs (L, T and Y dwarfs) or in wide binaries have also been subject to extensive study. All these objects lie in the bottom right corner of the diagram, with (close to-) null external irradiation. In between these two extreme parts of the diagram lie systems where both internal and external energy are comparable. At low energies, we have gas planets, such as Neptune and Jupiter, located far away from their host star. However, systems like SDSS J1433+1011, inhabit a unique corner of this parameter space shared with highly irradiated brown dwarfs and young hot Jupiters. In these systems irradiation is both strong and comparable to the intrinsic flux. Furthermore, the ability to measure albedos and heat redistribution efficiencies pro-

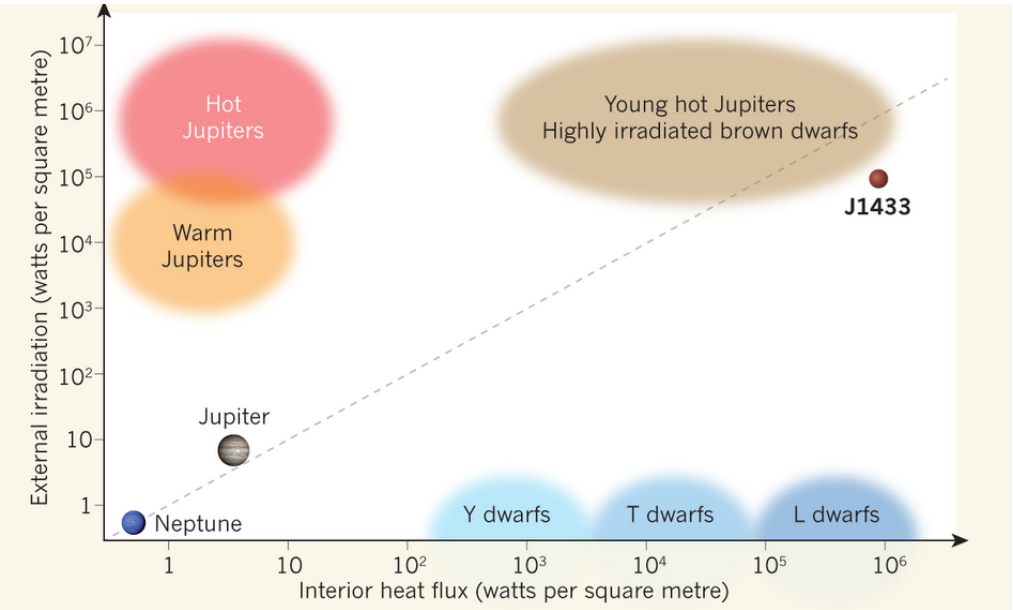

FIGURE 2.18: Parameter space of illuminated sub-stellar objects from Showman (2016). Dashed line represents where the internal matches the external irradiation.

vides opportunities for testing 3D circulation models (Perez-Becker & Showman 2013). Coupled with the unique prospect of obtaining detailed phase-resolved spectra and line profiles, this will permit quantitative tests of irradiated model atmospheres in a regime where these observables are expected to be quite sensitive to irradiation (Barman et al. 2004). Finally, donors in short orbital periods are rapid rotators (e.g. $v \sin i = 131 \pm 46$ km s^{-1}). The effects of the rotation may change the internal atmospheric dynamics and therefore may affect the heat distribution in sub-stellar objects (Showman & Kaspi 2013). By studying systems with a range of rotation speeds, we can empirically test this sensitivity.

Chapter 3

The Space Density of *Dead* Cataclysmic Variables

or how to find the missing ones

"Death's a capricious thing, innit?–Yes. Yes, she is."

- Neil Gaiman, *Sandman: The Doll's House*

I would like to acknowledge R. Pretorius and B. Warner for useful discussions and help with the Monte Carlo simulations. Also, I would like to thank M. Sullivan and S. Prajs for access to the PTF data and data reduction pipeline. Part of the work presented in the next chapter was published in Hernandez-Santisteban et al. 2016b...

The prediction that period bouncers should make up a large fraction (40-70%) of the CV population (Kolb & Baraffe 1999; Goliasch & Nelson 2015) and the lack of these systems in observational samples is one of the major discrepancies in CV evolution. As the donor star continues to lose mass and evolves to the sub-stellar regime, its radius no longer shrinks in response to mass loss. Instead, it stays roughly constant and may even increase. When this happens - specifically when the effective mass-radius index along the evolutionary track falls below 1/3 (see 1.3.1), the orbital period and orbital separation begin to increase again (Warner 1995). Since $\dot{M}_2$ is a function of the donor's mass, it is expected that mass loss may become very weak or stop completely in highly evolved period bouncers. CVs with degenerate secondaries and $P_{orb} \gtrsim 2$ hr have an average $\dot{M} \lesssim 10^{-11}$ $M_\odot$ yr^{-1}; $L_X \lesssim 10^{29}$ erg s^{-1} (Knigge et al. 2011) making them difficult to observe unless they are caught in a bright state, e.g., after a *rare* nova or dwarf nova outburst. I will consider as a *dead* CV, any system where most of the accretion light is washed out by the brighter WD and may be almost indistinguishable from an isolated WD for most of their time.

Since the donor star radius is at least an order of magnitude larger than that of the WD, we can expect a high probability of full eclipses of the WD by the degenerate secondary. Furthermore, the peak wavelength in the SED of each component is remarkably different. This fact allows us to search for such *dead* CVs by targeting the optically brighter WDs as they are periodically eclipsed by bigger and opaque bodies (since typical brown dwarfs will peak in the NIR, they only make a very small contribution at optical wavelengths). Any observation obtained during such an eclipse will result in a non-detection or *dropout* in the photometric pipeline. In order to exploit this idea, a multi-epoch survey with large-sky coverage is used.

Similar approaches have been used by the exo-planet community. In order to study the survival of planets beyond the latest stages of the evolution of their stars, large synoptic surveys have been used to target WDs. This has already yielded constraints on the fraction of planetary companions to isolated WDs. The Catalina Real-Time Survey, using a colour selection of $\sim 12,000$ WDs from SDSS, searched this sample for possible eclipsing systems. They found 20 of these with late M stars, and 3 others with possible sub-stellar companions (Drake et al. 2010). There are two previous studies (Parsons et al. 2013; 2015) that search for eclipsing WDs. They re-analysed the data and extracted cleaner light curves than those available in the CRTS database. All of their targets were identified as WD-MS binaries. Despite these previous efforts, a search for dropouts has not yet been carried out in the survey (A. Drake, priv. comm.). Two other studies have used direct targeting of WDs in searches for Jupiter-size objects in close orbits. Faedi et al. (2011) carried out a search among 174 confirmed WDs in the *SuperWASP* survey (Pollacco et al. 2006), but found no eclipsing nor transiting sub-stellar companions. They therefore placed an upper limit to the frequency of such companions of $< 10\%$. Later, the *Pan-STARRS1* survey targeted 3179 photometrically selected WDs in a 70 deg^2 field of view. This survey provided $\sim 1,000 - 3,000$ measurement epochs per object, for a total of 4.3 million measurements. As with previous studies, they found no eclipsing WD system with a planetary size companion (Faedi et al. 2011). Their larger dataset allowed them to place a firm upper limit on the frequency of planets around WDs of $< 0.5\%$.

In this chapter, I present a search for short P_{orb} and low-accretion rate period bouncers in three large synoptic surveys: Catalina Real-time Transient Survey (CRTS, Drake et al. 2009), the Sloan Digital Sky Survey (SDSS, York et al. 2000) and the Palomar Transient Factory survey (PTF, Law et al. 2009). All of these surveys covered the *Stripe 82* region. I will present the selection of the WD candidates in Stripe 82 and describe the methodology employed to find eclipsing systems. Following the null-result in both surveys, I estimated a firm upper limit to the space density of period bouncers. Finally I discuss my results in the context of the standard evolution of CVs.

3.1 Catalina Real-time Transient Survey

One of the first searches for dead CVs was implemented in the Catalina Real-time Transient Survey[1] (CRTS, Drake et al. 2009) using data from the first release. This survey is done in white light and covers 33,000 deg^2 in both hemispheres with limiting magnitudes in V between 11.5 and 21.5 mag, spanning over 10 years of observations with variable cadence. CRTS avoids the plane of the Galaxy due to the higher density of stars which impedes the detection and extraction of blended targets.

Since the survey is monochromatic, it was not possible to select WD candidates photometrically from the sample itself. Therefore, I used the catalogue of spectroscopically confirmed WDs by Kleinman et al. (2013) in order to narrow down the candidate selection. This catalogue is confined to the SDSS footprint and is by no means complete since only sources with a spectrum were included. However, the catalogue contains $\sim$ 20,000 WDs in the CRTS survey area that can be searched for possible variability.

At the time of this study, CRTS had not made the original images available and did not provide upper limits for non-detections[2]. I queried the CRTS database[3] for the 20,407 WD sources within the CRTS footprint in the Kleinman et al. (2013) catalogue. About 1,839 objects were not in the CRTS source catalogue while 20 sources only had a single detection. Furthermore, the Kleinman et al. (2013) catalogue has multiple entries for some WD candidates, due to degeneracy of the WD atmosphere model fits. These repeated entries were excluded from the variability study.

The CRTS database provides limited information for each photometric measurement which prevents me from cleaning the sample from contaminants. One of the main problems was associated with a flag indicating that a source was blended with an adjacent star, most likely due to bad atmospheric conditions. Since we are looking for variable objects, discerning which of the two entries belongs to the WD can introduce false-positives. Therefore, I have removed all entries where the survey reports different magnitude measurements for the same date.

After applying these filters, I was able to construct light curves for 18,986 objects with 3,767,871 individual measurements (an example of such a light curve is shown in Figure 3.1). The overall distribution of epochs for the full sample is presented in Figure 3.2.

[1]The CSS survey is funded by the National Aeronautics and Space Administration under Grant No. NNG05GF22G issued through the Science Mission Directorate Near-Earth Objects Observations Program. The CRTS survey is supported by the U.S. National Science Foundation under grants AST-0909182.

[2]Original images for the CRTS entries will be released soon in data release 3, DR3

[3]All the data collected was performed in October 2013. The database query is accessible at http://nesssi.cacr.caltech.edu/cgi-bin/getmulticonedb_release2.cgi

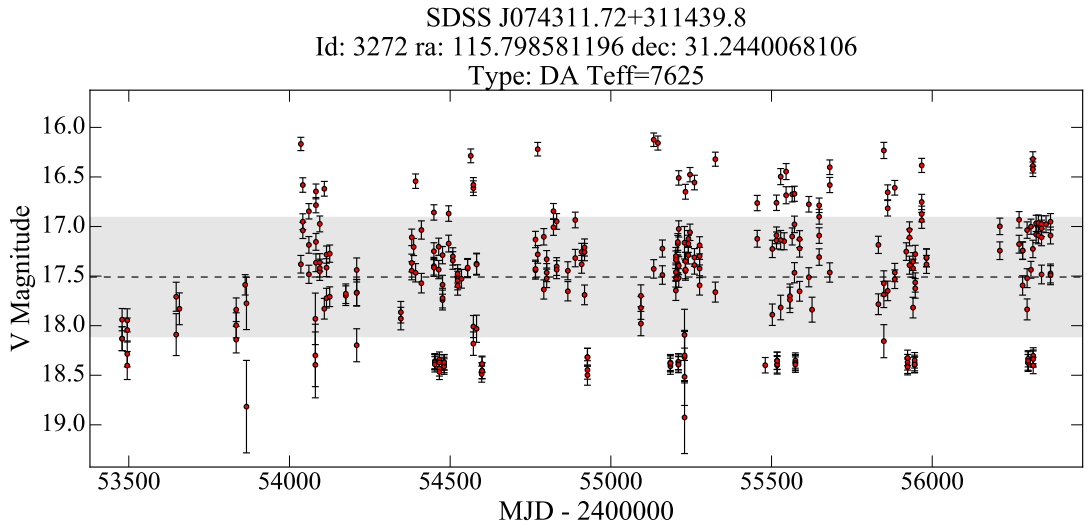

FIGURE 3.1: Example light curve of the white dwarf SDSS J074311.72+311439.8 from the CRTS dataset. The dashed line marks the median value and the gray band is the dispersion (rms) around the median. The measurements excluded are marked as blue.

On first examination of the light curves, it was noted that many presented strong variability. In order to select variable candidates from the full database automatically, I used two main variability indicators. Since all targets in this catalogue are confirmed WDs, it is reasonable to assume that the objects should be constant over time. Therefore, it is possible to test how probable it is that the source remained constant by calculating the χ^2_{lc} of every light curve relative to a constant (following the method described in Bell et al. 2014):

$$\chi^2_{lc} = \sum_i^n \frac{(m_i - \widetilde{m})^2}{\sigma_i^2} \tag{3.1}$$

where m_i and σ_i are the ith measurement and its associated error for each individual object, and $\widetilde{m}$ is the variance weighted mean defined as:

$$\widetilde{m} = \frac{\sum_i^n \frac{m_i}{\sigma_i^2}}{\sum_i^n \frac{1}{\sigma_i^2}} \quad . \tag{3.2}$$

Assuming that errors are normally distributed and independent, we expect that χ^2_{lc} will be distributed as the theoretical χ^2 distribution for the appropriate number of degrees of freedom (the number of measurements -1) because $\widetilde{m}$ is calculated for the data. Therefore, for any value of χ^2_{lc} we can estimate the probability, P, that the light curve was drawn randomly. I considered any object as potentially variable if $P < 0.001$. After applying this filter to the light curves, about ~ 60 % of the objects presented variability at this level. Thus, this statistic was not appropriate to discern any possible dropouts.

In order to narrow down the search, I used another approach to measure variability. I

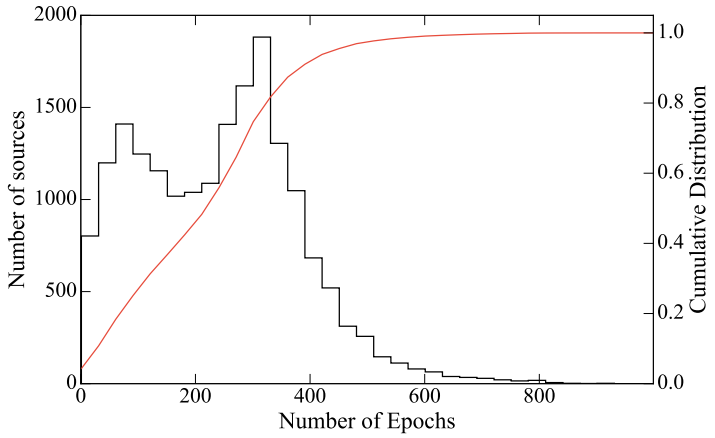

FIGURE 3.2: Distribution of the number of epochs per object for the white dwarfs in the CRTS database.

calculated the ratio of the standard deviation to the mean of a light curve, σ/μ, as well as estimating the flux difference between every measurement to the mean, $\tilde{m}$ and the median, $\langle m \rangle$, of the light curve for each object. The distribution of these statistics among the full CRTS sample is shown in Figure 3.3. I found 23,561 individual measurements where $m_i - \langle m \rangle > 1$ mag, that could indicate a possible eclipse candidate. These images would be suitable for further examination of contaminants and manual inspection.

In order to fully ensure that any flux drop is a real eclipse, and not an artefact of the observation, one would need to analyse the original images or at least use information on the atmospheric conditions. Therefore, it became extremely hard to identify with certainty any real eclipse for the dropout candidates. Furthermore, the survey does not provide any upper limit when the sources are not detected (A. Drake, priv. comm). I discuss the possibilities to enhance this part of the project in Chapter 5.

3.2 Stripe 82

Stripe 82[4] (York et al. 2000) consists of a 270 deg^2 band survey centred on the Celestial equator along the southern Galactic cap (-50° < RA<59°, -1.25° < DEC<1.25°; in galactic coordinates $b < -25°$), as seen in Figure 3.4. Stripe 82 was scanned numerous times during the SDSS so there is variability information available for sources in this region. In addition, I was also able to exploit the multi-wavelength nature of the SDSS in order to select WD candidates photometrically from the objects in the survey itself. The description of this selection is given below.

[4]Funding for the SDSS and SDSS-II has been provided by the Alfred P. Sloan Foundation, the Participating Institutions, the National Science Foundation, the U.S. Department of Energy, the National Aeronautics and Space Administration, the Japanese Monbukagakusho, the Max Planck Society, and the Higher Education Funding Council for England. The SDSS Web Site is http://www.sdss.org/.

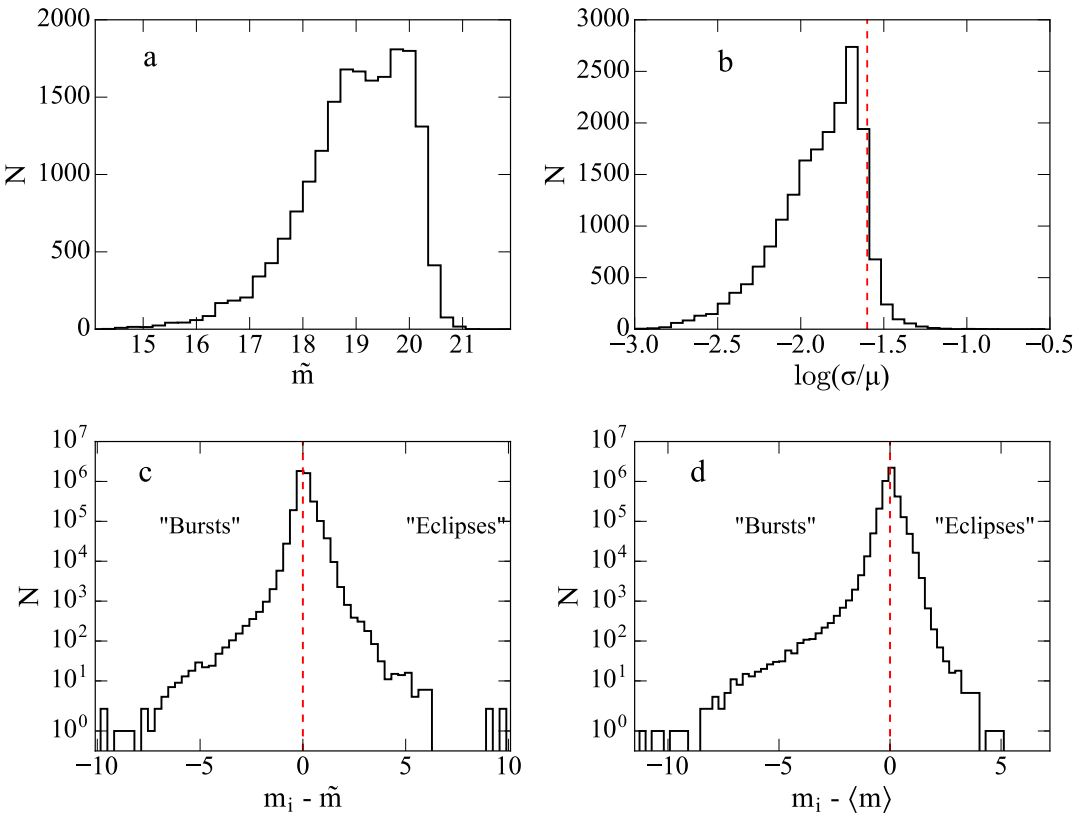

FIGURE 3.3: Photometric properties of the CRTS sample. a) Mean-weighted magnitude for each WD target, b) σ/μ ratio, c) Difference between every measurement and the $\tilde{m}$ of its corresponding light curve, d) Difference between every measurement and the $\langle m \rangle$ of its corresponding light curve.

3.2.1 Constructing the Stripe 82 WD sample

I constructed a sample of WD candidates in Stripe 82 by selecting objects from the high signal-to-noise catalogue (Annis et al. 2014). This allowed a uniform selection of candidates, as well as providing a simple, flux-limited sample (>95% completeness down to $g = 21$). I applied the photometric colour boxes (Girven et al. 2011) to select DA WDs in the SDSS Stripe 82 database through the Catalog Archive Server (CAS, see Appendix Figure C for SQL code to retrieve this selection)[5]. This photometric selection produced 2264 WD candidates. Allowing for incompleteness at a given magnitude range (Girven et al. 2011), I expected to have ∼1600 bona fide WDs in our sample. The general photometric properties of the WD sample is presented in Table 3.1.

The WDs in period bouncers are expected to be cool, $T_{eff} \lesssim 12{,}000$ K, due to their age and the low mass-accretion onto the WD surface (Knigge et al. 2011). Therefore, it is critical that our WD selection includes these low-temperature objects. Figure 3.5 shows

[5] http://cas.sdss.org/stripe82

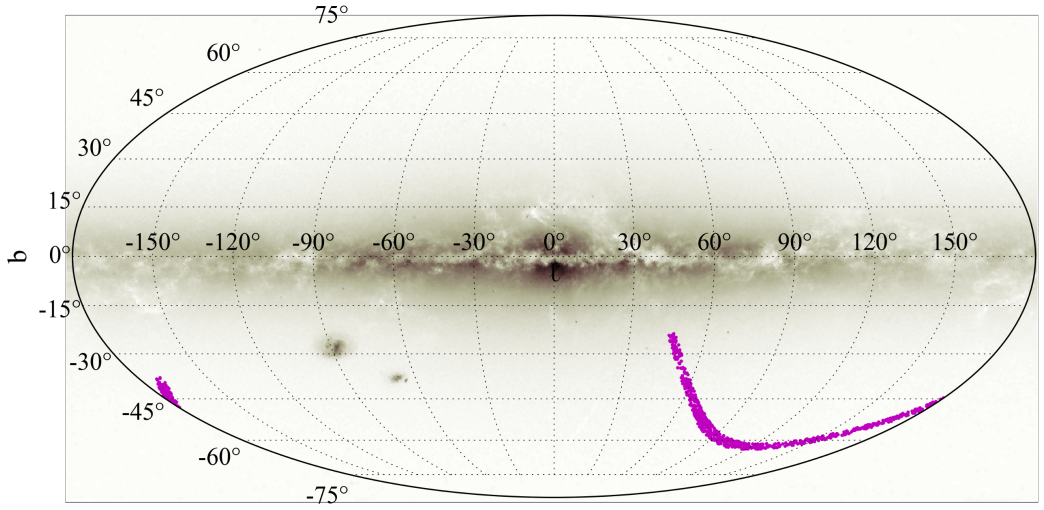

FIGURE 3.4: Stripe 82 Galactic map

my WD candidates against the Holberg & Bergeron (2006) theoretical cooling tracks[6]. It is encouraging that most of the targets lie between 7,000 - 15,000 K. Furthermore, a selection of the WDs in our sample have been spectroscopically confirmed by Kleinman et al. (2013). This allows us to compare the photometrically-selected sample with a larger one. In Figure 3.6, I show the distribution of effective temperature, T_{eff}, for the full sample and our candidates. It is clear that the two distributions are similar down to ∼6,000 K and that most of our WDs should lie in the region for post-minimum CVs. This confirms the sensitivity of the photometric selection to low-temperature WDs.

Accretion onto the surface of the WD is expected to produce soft X-rays for the boundary layer. Therefore, cross-matching our sample with X-ray catalogues might allow us to discern CVs from isolated WDs. I have cross-matched the WD sample with two catalogues from the *XMM-Newton* archive, the serendipitous catalogue (Rosen et al. 2016) and the 31 deg^2 in Stripe 82 (LaMassa et al. 2016). Only five matches were found, all of which turned out to be confirmed quasars (the largest contaminant in the WD sample). These objects were excluded from the final sample.

3.3 The SDSS Stripe 82 dataset

I used the publicly available data from the SDSS Legacy Survey survey of Stripe 82. The main part of the data, originally used in the search for supernovae, was obtained in three

[6] http://www.astro.umontreal.ca/~bergeron/CoolingModels

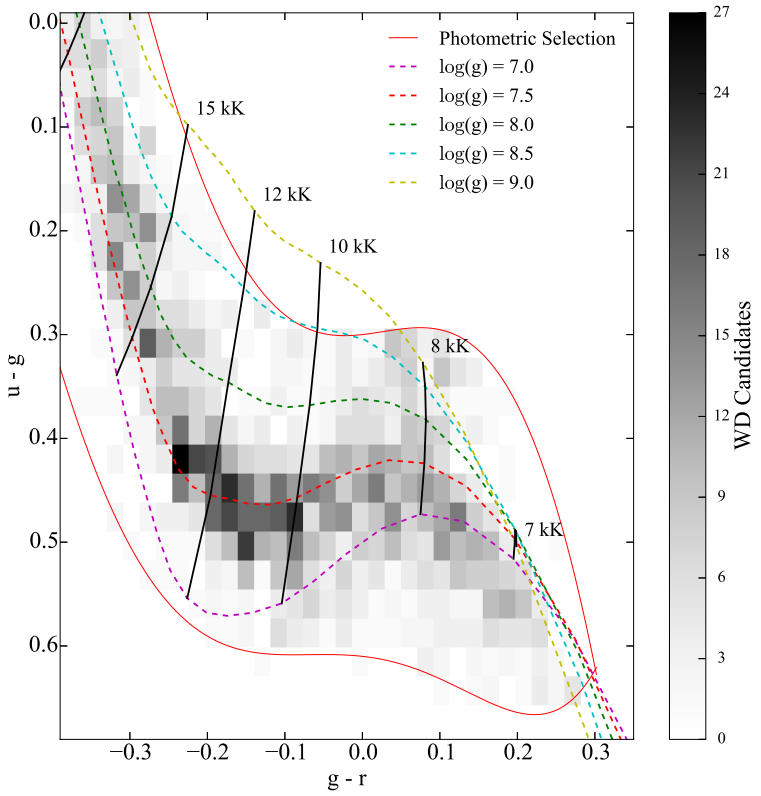

FIGURE 3.5: Photometric selection histogram of the WD candidates in SDSS Stripe 82. Colour-colour cuts are shown as the red continuous line (Girven et al. 2011) and WD cooling tracks (dashed lines) are overlaid for different log(g) in 0.5 steps (Holberg & Bergeron 2006).

seasons between 2005 and 2007. This adds to previous snapshots taken as part of SDSS-I Legacy. In total, the Stripe 82 database contains ∼80 observations for every object, taken over 302 scanning runs with exposure times of 54.1 s, with a variable cadence. The quality of the data is varied, with roughly one-quarter of the observations taken in photometric conditions (e.g. low cloud coverage). Despite this mixed quality, the data is still valuable for the project, since full eclipses of bright sources can be detected even in low quality data.

The distribution of epochs per target is shown in Figure 3.7. About $\lesssim 10\%$ of the objects appear to have more than 100 epochs. After closer inspection of the individual light curves, it was clear that they were data from stars within the query box for every WD candidate, appearing as duplicates in the light curve. These were removed from the final sample. I queried the SDSS CAS database for all the available photometry in a $3'$ radius of every WD candidate. This allowed me to construct multicolour light curves for every object, as shown in Figure 3.8.

The Stripe 82 dataset has, of course, been studied before (Sesar et al. 2007). However, no search for full eclipses or dropouts has previously been performed (Ivezic, private

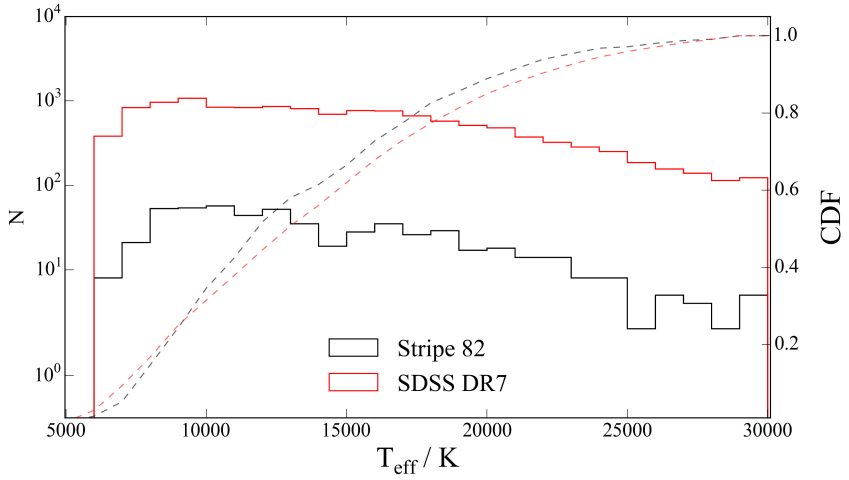

FIGURE 3.6: Comparison between the WD effective temperature distribution in my sample (*black line*) and the spectroscopic sample (*red line*). All these objects were spectroscopically confirmed in Kleinman et al. (2013).

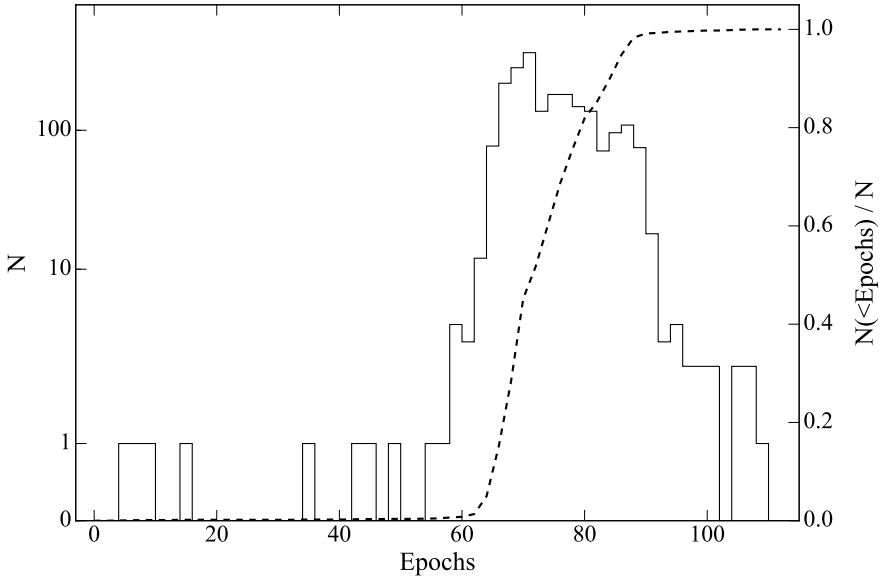

FIGURE 3.7: Epoch distribution for WD candidates in SDSS. The cumulative distribution is plotted as a dashed line.

WD id	RA	Dec	g'			R		
	deg	deg	mag	$\hat{m}$	rms	mag	$\hat{m}$	rms
0000	309.16595	-0.66203	18.13	0.02	0.099	17.98	0.02	0.049
0001	309.16953	0.36834	17.08	0.01	0.049	17.51	0.02	0.035
0002	...	...	...	...	...	...	...	...
0003	309.38998	0.32968	18.71	0.03	0.175	19.10	0.05	0.092
0004	309.49033	0.98303	16.36	0.03	0.071	16.62	0.01	0.058
0005	309.72900	0.65325	18.12	0.02	0.028	18.52	0.03	0.074
0006	309.72314	0.62537	18.66	0.02	0.047	18.49	0.03	0.155
0007	309.64340	-0.17908	18.81	0.03	0.059	19.23	0.06	0.098
0008	309.59900	1.10977	17.92	0.02	0.088	18.26	0.03	0.093
0009	309.78809	1.10119	16.43	0.01	0.079	16.80	0.01	0.019
0010	309.96603	0.66858	17.55	0.01	0.036	18.02	0.02	0.046
0011	310.45578	0.59884	18.83	0.03	0.091	19.22	0.05	0.073
0012	310.53851	-0.39504	18.74	0.03	0.080	19.23	0.05	0.110
0013	310.49573	0.05706	18.87	0.03	0.090	19.45	0.06	0.083
0014	310.56375	0.99690	18.95	0.03	0.102	19.26	0.05	0.074
0015	310.64890	0.93218	18.27	0.02	0.046	18.80	0.04	0.111
0016	310.75946	-1.11300	18.95	0.03	0.045	19.40	0.06	0.121
0017	310.75378	0.36253	17.70	0.02	0.023	18.29	0.03	0.060
			⋮					

TABLE 3.1: Photometric Properties of the WD candidates. WD entries were not on the PTF footprint and therefore no photometric information was recovered.

communication). In order to look for such dropouts without re-extracting the SDSS photometry from the raw images, I implemented selection criteria based on the information of sources' variability in the fields provided in the SDSS database.

3.3.1 Dropout search

Specifically, I queried the SDSS database photometry in all available fields that contain a WD candidate. Thus, for non-variable WDs, I should expect a consistent photometric measurement in each field. In practice, this idealised picture is far from reality since observational conditions and systematics of the data reduction pipeline contribute to false positives. In order to locate and discriminate potential eclipsing systems, I performed two basic tests.

First, I discarded any observation where the object was localised near the edges of the image, where the pipeline can provide incorrect flux measurements (since part of the star's point spread function might lie outside of the detector). By excluding data blindly, I avoid creating a bias selection in the sample, since, *a priori*, it is not expected that eclipses are preferentially observed at the edges of images. Second, I had to account for variable observational conditions. Clouds, bad seeing and cosmic rays can all potentially

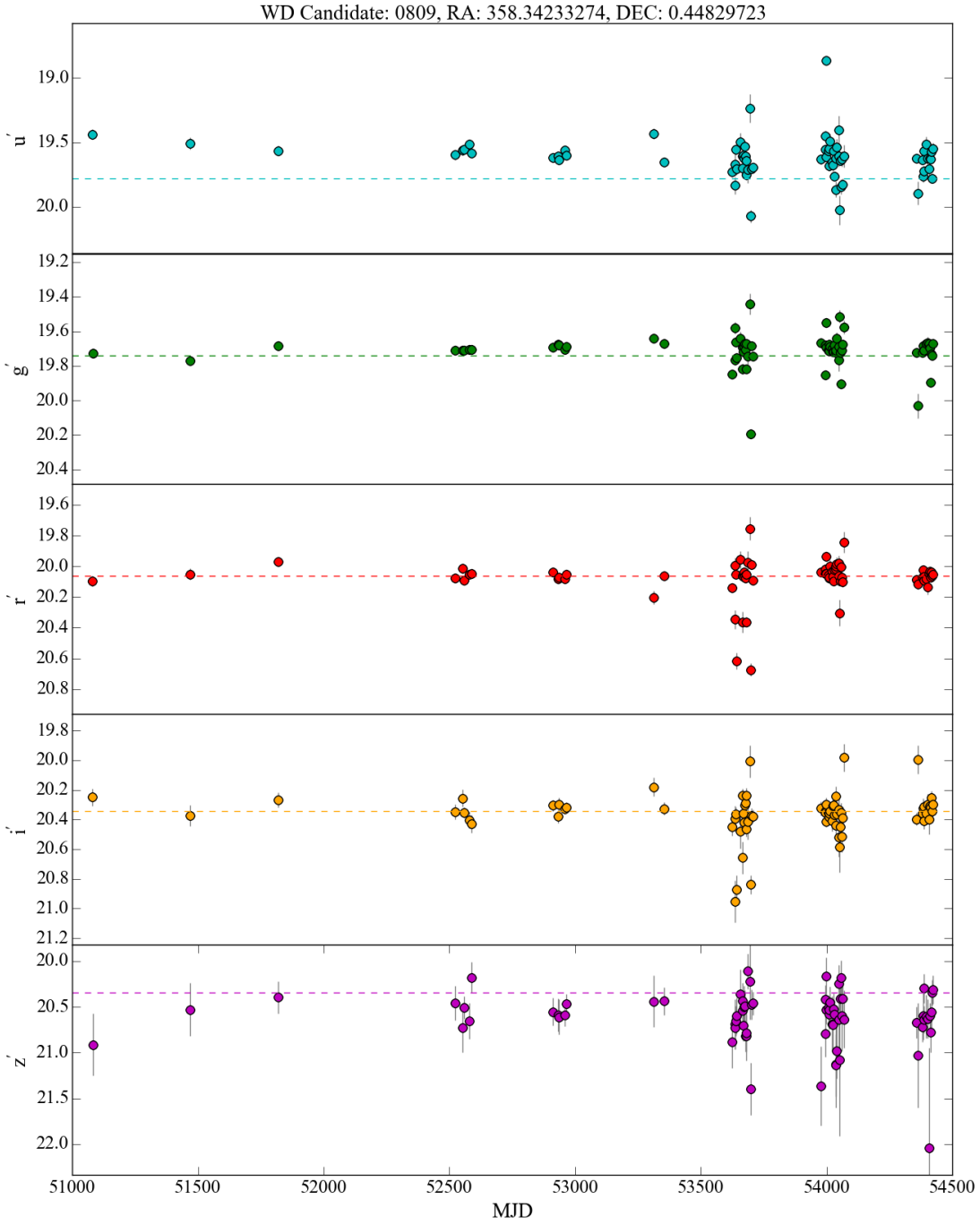

FIGURE 3.8: SDSS lightcurve of a WD candidate. The five SDSS filters *ugriz* are shown, as well as the mean magnitudes as dashed lines.

lead to non-detections[7]. In order to estimate the limiting magnitude in each individual frame, I employed an empirical procedure. Every non-detection candidate frame was queried for objects with similar brightness to the WD candidate within ±0.3 mag. If no object was detected, then the image (and associated datum) would be flagged as a

[7]In general, the survey was not performed in photometric conditions. The seeing conditions for individual runs can be found in www.sdss.org/dr7/coverage/sndr7.html. This allowed me to verify that some frames did not reach a deep limiting magnitude.

false-positive and excluded from the candidate sample. After these cuts, only 271 frames were left for visual inspection. After manually inspecting the raw images, I found no true dropouts in the sample. Most of the remaining false-positives were flagged due to the object being found just outside the selection area (at a distance $> 3''$). However, when inspected, the target star was visible in the individual images in all cases.

3.4 The Palomar Transient Factory Survey

The data available for this study spanned 5 years, from 2009 –2014, during which Stripe 82 was contained within the full PTF footprint (Law et al. 2009). The survey was mainly taken in two optical filters, R and the SDSS g' filter, both in 60 s exposures. I used both filters in my analysis. Fortunately, it is possible to access the raw images and perform photometry at any given position. This allowed me to search for any possible dropouts and later verify them through manual inspection.

I extracted the lightcurves of the WD candidates with the Supernova Legacy Survey (SNLS) pipeline (for further details on the data reduction see Firth et al. 2015). The pipeline produces forced PSF photometry on each target for all available fields. This provides upper limits on the location of the WD candidates as well as an estimate of the limiting magnitude in each individual frame. In total, the PTF sample contained 638,118 individual measurements from the WD candidate sample. The number of epochs available for each object is highly variable, depending on the specific location of the WD candidate in Stripe 82. On average, we found that every object has $N_R \sim 200$ in R and $N_g \sim 100$ in g', as shown in Figure 3.9.

3.4.1 Dropout search

In order to exclude false-positives, we developed the decision tree outlined in Figure 3.10. First, I excluded all data points that I considered as *bad* measurements. This allowed me to get rid of most false-positives in an unbiased way. I excluded all measurements close to the edge of the detector, where sensitivity drops, and the data reduction pipeline is not effective at retrieving photometric values. I also required sources to have an average magnitude, $\langle m_i \rangle$, at least 1 mag brighter than the limiting magnitude, $m_{lim} > \langle m_i \rangle + 1$, where m_{lim} corresponds to a 3σ detection above the background. This allowed me to be confident that, in case of an eclipse, the signal to noise in that specific frame would be enough to discern a true dropout. Finally, I removed all frames where photometric conditions were poor (where the parameter from the reduction pipeline, FLUXSCALE> 0.8, serves as a proxy for bad seeing conditions). This created a set of 295,463 *good measurements* for any given WD candidate. Only from these images, would we be confident of a dropout candidate.

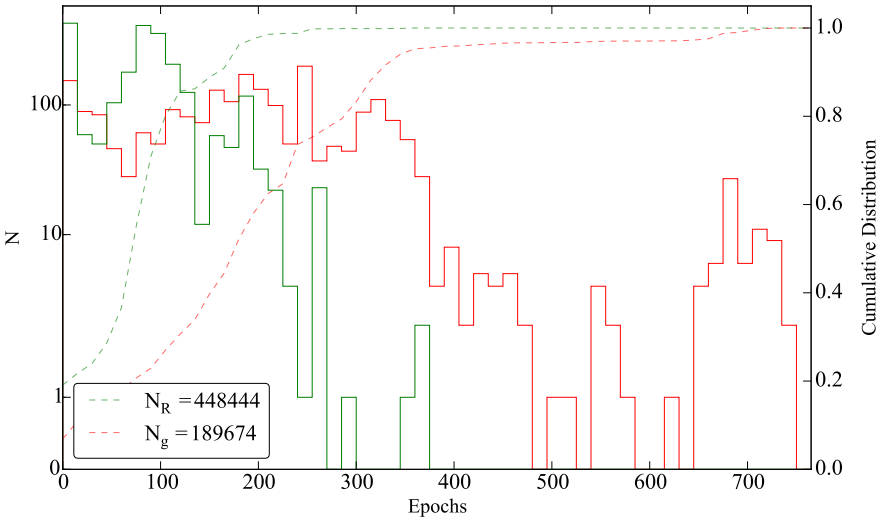

FIGURE 3.9: Epoch distribution for WD candidates in PTF. Observations are plotted in the individual R (red) and g' (green) filters. The cumulative distributions are plotted as dashed lines for both filters.

I then selected as eclipse candidates any data points where the pipeline could not retrieve a flux value or where I observed a drop in flux, $\Delta m = m_i - \langle m_i \rangle \geq 1$ mag. In Figure 3.12, I show all the different photometric properties of the PTF sample. The final selection yielded 606 images in both filters (see *Dropout candidates* in Figure 3.12) with candidate drop-outs. All of these were manually inspected. As with the SDSS data, all of these candidates turned out to be false positives. The main contaminant for non-detections (*NaN*) was the recurrence of the WD candidates in dead pixels of the CCD cameras, as exemplified in Figure 3.13.

3.5 Estimate of the space density

The absence of eclipsing systems in our sample is consistent with previous efforts on this front. In this section, I describe the theoretical framework I used to convert this into an upper limit on the space density of any *hidden* population of *dead* CVs.

3.5.1 Eclipse probability

In order to determine the probability that a system will undergo eclipses, we rely on the assumption that the WD is the dominant source in both R and g' bandpasses. Sub-stellar donors have very low temperatures ($\lesssim$ 2500 K), with spectral types later than $\gtrsim$L1 (Littlefair et al. 2008; this thesis). They are brightest in the near-infrared, and their contribution in the optical is negligible. Therefore, any eclipse will have a high contrast and can be modelled as a bright object being eclipsed by a dark opaque

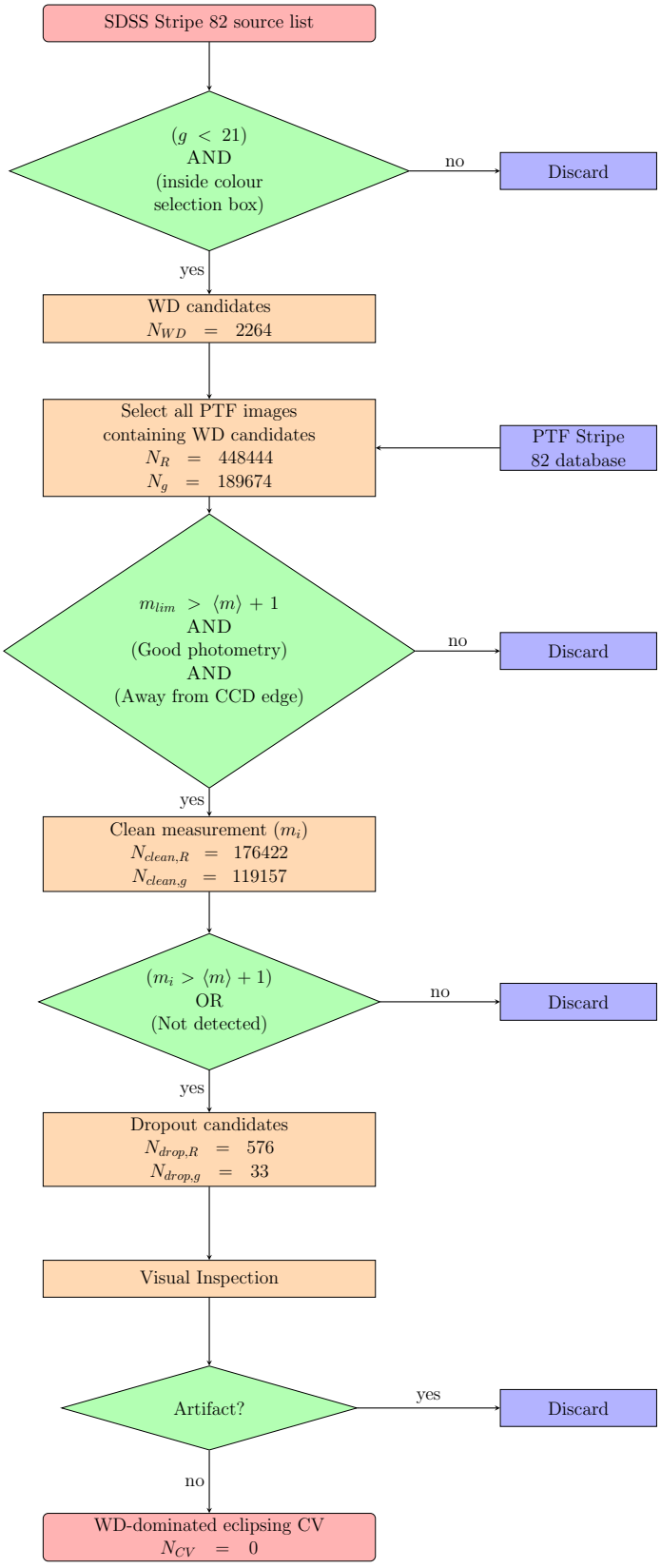

FIGURE 3.10: PTF decision tree. The different green diamonds represent the observational cuts.

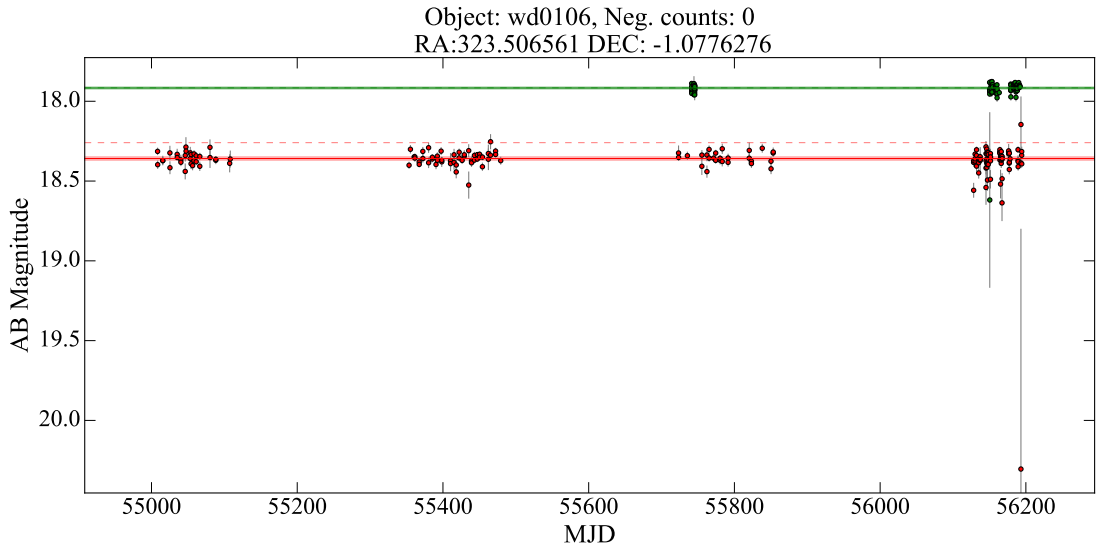

FIGURE 3.11: PTF R (red) and g' (green) lightcurves of a WD dropout candidate. The solid line is the median value of all the data in each filter while the dashed line is the mean SDSS value. Over the median PTF value, I show the r.m.s of the lightcurve as a band.

body. Furthermore, the donor is assumed to be filling its Roche-lobe. From Roche-lobe geometry, the duration of the half-width of an eclipse for any semi-detached system is given by (Chanan et al. 1976; Horne et al. 1982; Horne 1985):

$$\cos^2(2\pi\varphi_{1/2}) = \left[1 - \left(\frac{R_2}{a}\right)^2\right] \sin^{-2} i \quad , \tag{3.3}$$

where $\varphi_{1/2}$ is the half-width of the eclipse in phase. By combining Equations 3.3 and 1.5, we can obtain the eclipse width as a function of q and i.

The probability that an individual snapshot with an exposure time, t_{exp}, overlaps with an eclipse of duration, $t_{eclipse}$, is given by

$$P = \frac{t_{eclipse} + t_{exp}}{P_{orb}} \quad . \tag{3.4}$$

We can then estimate this probability since $t_{eclipse} = 2\pi\varphi_{1/2}$ and $t_{exp} = 60$ s for the PTF survey. However, the exposure time will be affected by the fact that the selection criteria (see Section 3.4.1) impose a flux drop of $\Delta m \geq 1.0$. An observation where the eclipse is partially observed can therefore achieve the selection criteria, thus modifying the t_{exp}. We can then define an *effective exposure time*, t_{eff}, given by

$$t_{eff} = t_{exp} + \Delta t \quad , \tag{3.5}$$

where Δt is a correction factor. In order to calculate Δt, we need to do some approximations for the eclipse. Due to the high-contrast between the WD and the sub-stellar

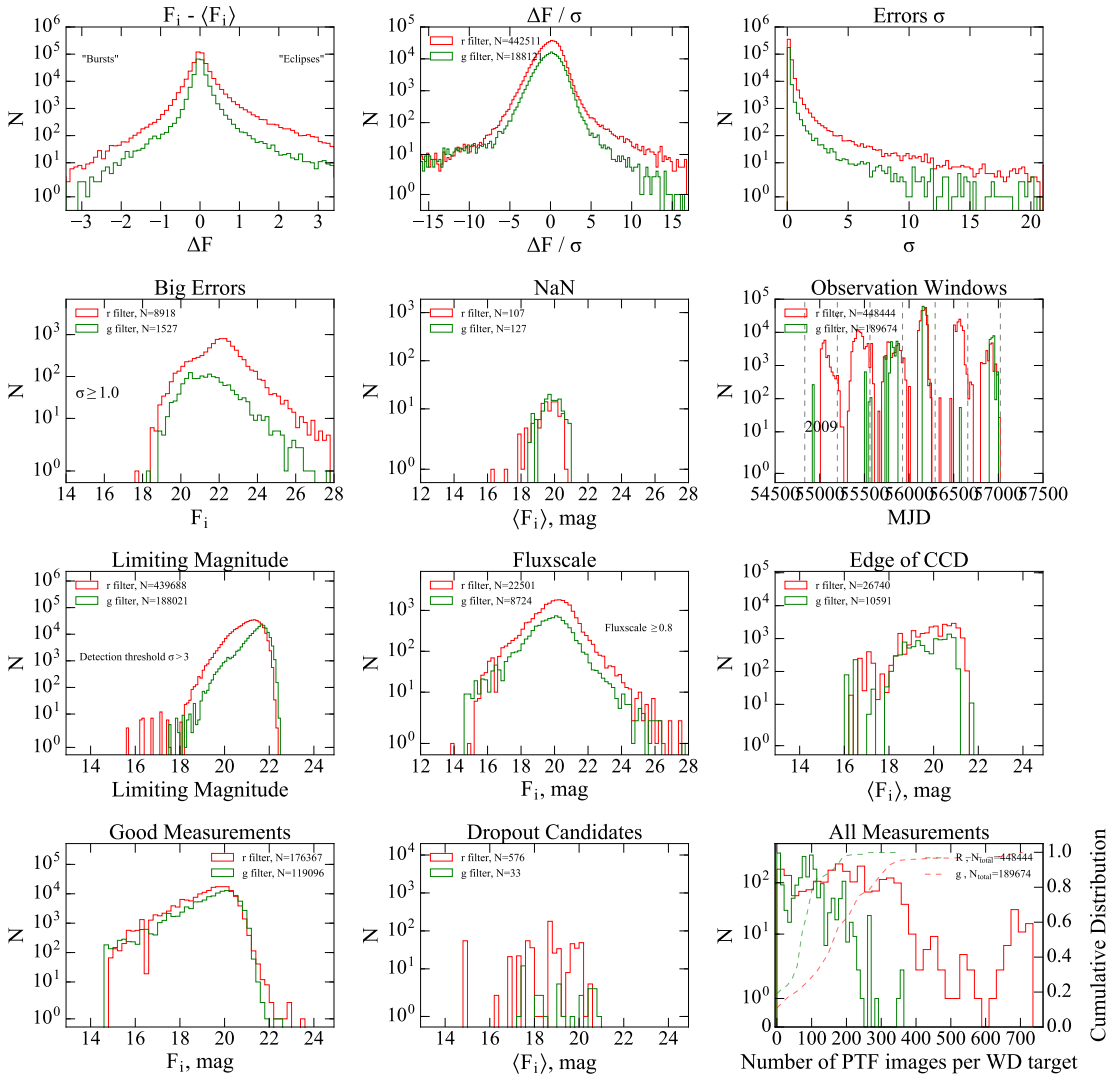

FIGURE 3.12: Photometric properties of the PTF sample. The different properties are divided by each filter used, i.e. R (red) and g' (green).

donor contributions at optical wavelengths, the eclipses can be approximated as a light source eclipsed by an opaque body, as exemplified in Figure 3.14. Therefore, the flux, f, measured in a single exposure will be determined by the ratio of time spent outside eclipse, t_{out}, over the entire exposure time:

$$f = \frac{t_{out}}{t_{exp}} \quad . \tag{3.6}$$

This is valid as long as the WD is a constant source of light.

Then, we can obtain the amount of time the eclipse has to be inside an individual exposure to comply with a given f. From Figure 3.14, we can define Δt as

$$\Delta t = t_{out} - \frac{1}{2} t_{exp} \quad . \tag{3.7}$$

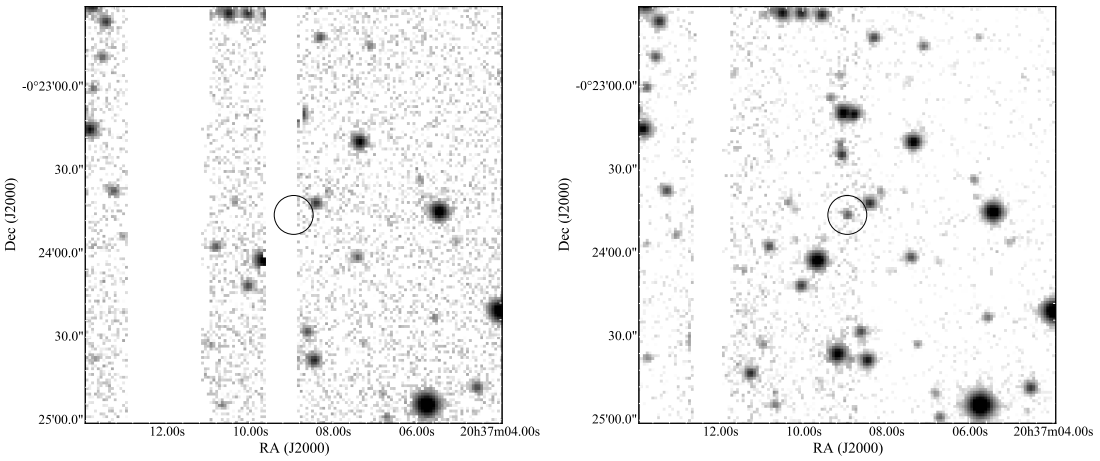

FIGURE 3.13: Manual inspection of a false positive in the PTF sample for a WD candidate (*black circle*). *Left* : The observed epoch for a WD candidate. The object is missing due to masking of bad pixels. *Right* : Reference image for the same field which clearly contains the WD.

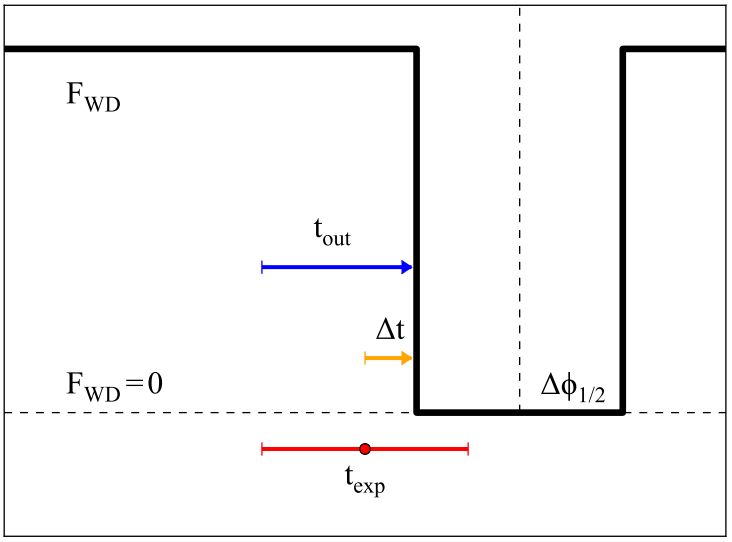

FIGURE 3.14: Schematic of a WD eclipse and the determination of the effective exposure time. The vertical dashed line represents mid-eclipse and the horizontal dashed line, the zero-flux level. The exposure time (t_{exp}, red), the time outside eclipse (t_{out}, blue) are marked for reference.

Due to the symmetry of the eclipse, the factor Δt has to be accounted twice since it can happen before and after the eclipse. Therefore, by multiplying by a factor of 2 Equation 3.7 and combining with Equation 3.6 the final correction factor for the exposure time is:

$$\Delta t = (2f - 1)t_{exp} \quad , \tag{3.8}$$

where I have set the flux drop to $f = 0.4$, the equivalent of $\Delta m = 1$ as defined in the photometric selection.

Thus, the probability of detecting an eclipse for a given exposure time is given by:

$$P_{\text{eclipse}} = \frac{2\varphi_{1/2}P_{orb} + t_{eff}}{P_{orb}} \quad , \tag{3.9}$$

It follows that the probability of observing no eclipses, $P_{\text{no eclipse}}$, in a light curve is given by

$$P_{\text{no eclipse}} = (1 - P_{\text{eclipse}})^N \quad , \tag{3.10}$$

where N is the number of observations of a WD candidate, given by the selection criteria described in Section 3.4. Then, the probability that a given WD should have been observed during *at least one* eclipse, P_1, becomes:

$$P_1 = 1 - P_{\text{no eclipse}} \quad . \tag{3.11}$$

The sum of the probabilities over every object will provide the Poisson expectation value of the number of eclipses observed in each population.

3.5.2 The Galactic CV model

The model I used to predict the number of observable CVs for a given space density has been used in past studies of CV space densities (Pretorius et al. 2007; Pretorius & Knigge 2012; Pretorius et al. 2013; Pretorius 2014). The space density of CVs, $\rho(z)$, is taken to be a function of their position in the Galaxy:

$$\rho(z) = \rho_0 \exp^{|z|/h} \quad , \tag{3.12}$$

where ρ_0 is the Galactic plane density, z is the distance from the Galactic plane and h is the characteristic scale height of the thin disc of the Galaxy. This assumption is reasonable, since CVs have been shown to reside mostly in the Galactic disc (Stehle et al. 1997; Ritter & Kolb 2003). However, the simulations were computed for two different scale height populations, one young with a scale height of $h = 250$ pc (typical of young systems) and h =450 pc (typical of older systems, and most likely to apply to period bouncers).

The density of neutral hydrogen also depends on z. The interstellar extinction is thus found by integrating the column density along the line of sight for every WD in our sample. The density dependence of the interstellar medium (ISM) on z is defined as:

$$\rho_{ISM} = \rho_{ISM,0} \exp^{-|z|/h_{ISM}} \quad , \tag{3.13}$$

where $h_{ISM} = 250$ pc (Robin et al. 2003), and the density in the plane, $\rho_{ISM,0}$, was obtained by assuming $A_V = 2$ mag kpc^{-1} for $b = 0°$ (Allen 1976), with $N_H = 1.79 \times 10^{21} A_V$ cm^{-2} (Predehl & Schmitt 1995).

3.5.3 Monte Carlo simulations

In order to predict the number of CVs in Stripe 82 as a function of space density, we performed a Monte Carlo simulation where we generated a galactic sample of dead CVs (as described in Section 3.5.2) in the Stripe 82 field. For computational efficiency, we created a grid of simulated dead CVs at four WD effective temperatures: 5,000 K, 7,500 K, 10,000 K and 12,500 K; and for two WD masses: $M_1 = 0.8$ $M_\odot$ (mean mass for CVs, Zorotovic et al. 2011) and $M_1 = 0.6$ $M_\odot$ (mean mass for field WDs, Kleinman et al. 2013). We used the WD cooling tracks to retrieve their absolute magnitudes (Holberg & Bergeron 2006). After applying galactic extinction, we selected those WDs that complied with the photometric selection criteria ($g < 21$).

Afterwards, I calculated the number of epochs of every simulated target as it would have been observed by the PTF survey. To do this empirically, I matched every simulated dead CV to its nearest WD candidate and assigned the same number of observable epochs considered as *good measurements* (see 3.4.1). As an initial simulation, I fixed the mass of the donor, $M_2 = 0.035$ $M_\odot$ as well as the orbital period, $P_{orb} = 1.4$ hr (typical values for a period bouncer, Knigge et al. 2011). This allowed me to randomly sample inclination angles for all these systems and calculate the eclipse width for each object.

Finally, I estimated the probability of observing at least one eclipse for each simulated WD and consequently the expectation value of number of objects detected at each WD temperature. To determine the upper limit for the mid-plane space density, I calculated ρ_0 such that we should have observed three systems, therefore a null detection is then a 2σ result. The space density, as a function of WD effective temperature, for the different combinations of h and M_1, is shown in Figure 3.15.

This result provides firm upper limits to this hidden population of dead CVs. Since systems around the period minimum have WD temperatures close to 12,500 K (SDSS J1433+1011 for example), period bouncers are likely to be a lot cooler than this. In fact, the WD corresponding to the P_{orb} simulated is $T_{eff} \sim 10,000$ K. Taking this temperature value (for $h = 450$ pc and $M_1 = 0.8$ $M_\odot$) as a typical dead CV, I found the upper limit for the space density to be $\rho_0 < 2 \times 10^{-5}$ pc^{-3}. At lower temperatures i.e. longer P_{orb} period bouncers, the upper limit for ρ_0 quickly increases, as the survey becomes less sensitive to dimmer objects, as is clear in Figure 3.15.

3.5.4 Robustness and caveats

I explored the robustness of the results by assuming limiting cases for the system components, particularly the effects of P_{orb} and M_2. In order to accommodate the viable parameter space of period bouncers, I ran the Monte-Carlo simulations for the extreme values of systems at the period minimum: $P_{orb} = 1.3$ hr and $M_2 = 0.06$ $M_\odot$; and a

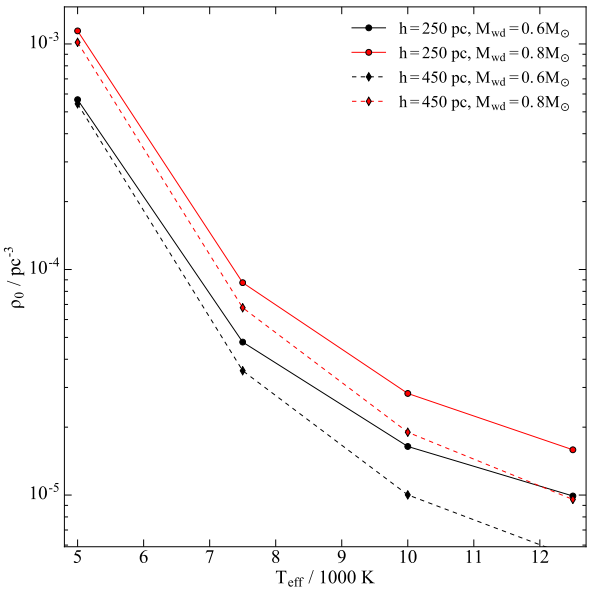

FIGURE 3.15: Space density upper limit for dead CVs. This simulation assumes $M_2 = 0.05$ $M_\odot$ and $P_{orb} = 1.4$ hr.

highly evolved CV with $P_{orb} = 3.0hr$ and $M_2 = 0.02$ $M_\odot$. In Figure 3.16, I show the results of this parameter study. As reflected in the plots, changing the limits results in a vertical shift of the upper limits. At WD temperatures of 10,000 K, however, I find maximum variations in the upper limit to be $\sim 50\%$. An important conclusion of this plot arises from the extreme case for the oldest CV in the simulation, as seen in the right lower corner of Figure 3.16. We can reasonably assume that temperatures for the WD are closer to 7,500 K, then for $P_{orb} = 3.0$ hr and $M_2 = 0.02$ $M_\odot$, the upper limit is $\rho_0 \lesssim 8 \times 10^{-5}$ pc^{-3}.

A possible caveat to the results presented in this chapter is the validity of the initial assumption that dead CVs resemble isolated WDs. There are other accreting systems which possess very low mass transfer rates $\dot{M} \lesssim 10^{-12}$ $M_\odot$ yr^{-1} such as AM CVn (Solheim 2010) and even NS systems (e.g. Degenaar et al. 2010), that display features of accretion e.g. emission lines, blue continuum and outbursts. This fact would prevent us from selecting them accurately in deep multi-colour surveys.

3.6 Discussion

In this chapter, I have presented a search for *dead* CVs in large-synoptic surveys. I focused on Stripe 82, where I photometrically selected $\simeq 2500$ WDs candidates. I used the SDSS and PTF surveys to look for eclipsing systems. The high contrast between the donors and WDs in these systems should produce high signal-to-noise eclipses that can be observed as non-detections (dropouts). I found no convincing candidate for such

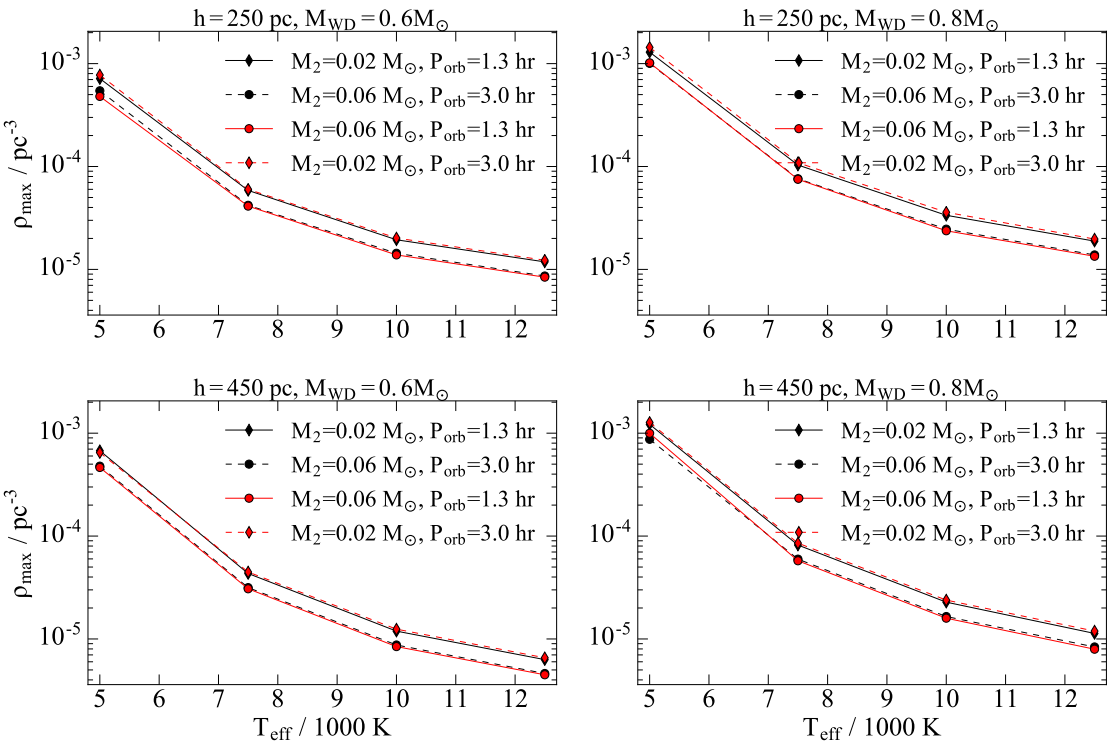

FIGURE 3.16: Parameter exploration for space density.

systems. This null-result allowed me to establish a firm upper limit to the space density of period bouncers. I will now discuss the implications of my results in the context of CV evolution.

3.6.1 Implications on CV evolution

It is not clear why the present-day population of CVs is inconsistent with theoretical predictions. The high fraction of period bouncers in relation to the full sample is particularly problematic, given the few candidates known. Even though large synoptic surveys are particularly biased against the discovery of period bouncers this tension remains even when accounting for such bias (Pretorius et al. 2007). Theoretical estimates of the space density of CVs have usually been found to be too optimistic (de Kool 1992; Kolb 1993; Politano 1996) when compared to observational constraints (Hertz et al. 1990; Shara et al. 1993; Patterson 1998; Warner 2001; Cieslinski et al. 2003; Schreiber & Gänsicke 2003; Pretorius & Knigge 2012). A summary of these estimates is presented in Figure 3.17. All of the observational constrains on ρ_0 have been performed for the total population of CVs.

In contrast, the work presented here had the aim to target exclusively this elusive subset of the CV population and has produced the first firm upper limit on the space density

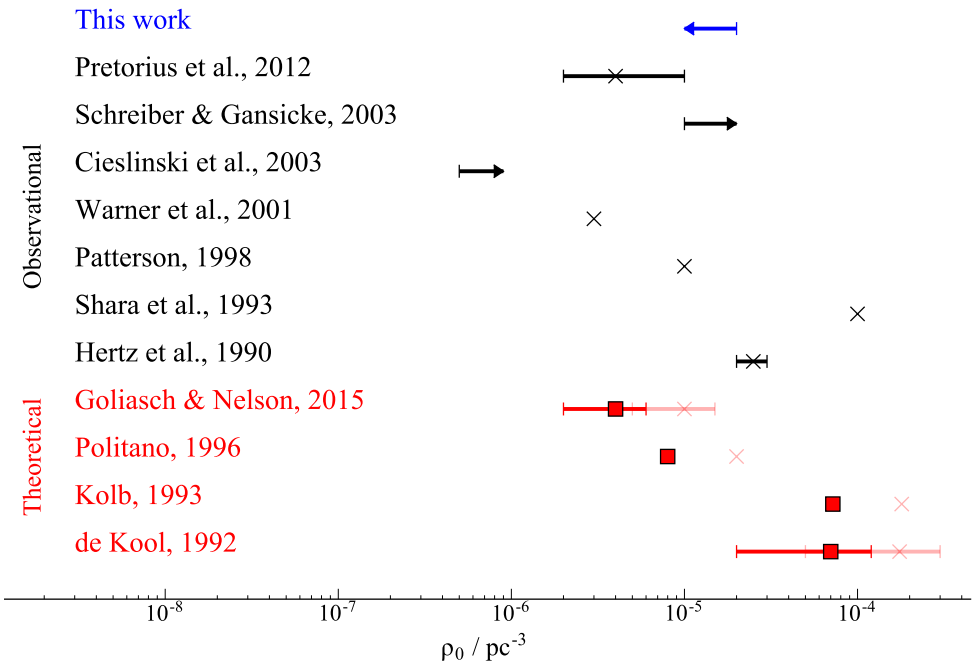

FIGURE 3.17: Space density comparison for CVs. The total ρ_0 are shown in *crosses* and the scaled *dead CVs* space densities are shown in *squares*.

of period bouncers, $\rho_0 < 2 \times 10^{-5}$ pc^{-3} for a typical T$_{\rm eff}$= 10,000 K. For this reason, a straightforward comparison between the estimate presented in this thesis and theoretical estimates is not adequate. I have scaled the space densities for the fraction of period bouncers recovered in the different theoretical works in Figure 3.17 (displayed as square markers). This fraction varies from 40-70% of the total population depending on the specific assumptions of the model. I have assumed the most pessimistic scenario (40%) to draw some general conclusions. The upper limit obtained in this work rules out the most optimistic models (de Kool 1992; Kolb 1993) and it is consistent with more recent simulations (Goliasch & Nelson 2015). If indeed period bouncers are not as common as predicted, then there must be a mechanism that prevents their creation or they must somehow be removed from the present-day CV population.

One of the ways to remove period bouncers is by accelerating the evolution of systems after the period gap, leading to the evaporation of the companion (Patterson 1998). This scenario would require a higher mass-transfer rate after the period minimum in order to lose most (or all) of its mass within the age of the Galaxy. Evidence for a higher $\dot{J}$ has been proposed based on empirical fits to the observed CV population (Knigge et al. 2011). A likely candidate for this discrepancy is the most poorly understood mechanism in CV evolution: magnetic braking. The idea of very weak magnetic fields in fully-convective stars including brown dwarfs has been contradicted by recent observational

evidence (e.g. Hilton 2011; Hallinan et al. 2015). Furthermore, observations of solar-type dynamo activity in convective stars might also invalidate the assumption of zero magnetic braking below the period gap (Wright & Drake 2016).

Understanding the origin of these discrepancies remains a highly active area of research, particularly in binary population synthesis models. Schreiber et al. (2016) presented an empirical model, in which they introduce an additional sink of angular momentum, associated with nova eruptions. They interpret this as a result of friction generated between the nova ejecta and the atmosphere of the donor, which can be an efficient AML mechanism particularly in systems with low-mass primaries (Schenker et al. 1998). Their simulations allowed them to reproduce the distribution of WD masses in CVs by removing systems from the overall population (particularly those with low-mass WDs as primaries, which have not been observed so far). Similarly, Nelemans et al. (2016) calculated that early nova outbursts in low-mass WD CVs can lead to unstable mass transfer regimes and an eventual merger. Both models might help to alleviate the tension between observational and theoretical estimates of space densities of CVs.

Another possibility to enhance the mass transfer rate is via a long post-nova relaxation time, proposed as an explanation to the long-term light curves of BK Lyn (Patterson et al. 2013). This system was first identified as a nova-like which eventually transitioned to a dwarf nova in 2005. The authors interpret this dramatic change in its behaviour as a natural cooling down after a nova eruption almost ~ 2000 years ago. This long-term relaxation (observed as a progressive brightness decline) was produced by an irradiated donor inducing higher mass transfer epochs (lasting $10^4 - 10^5$ yr). In this scenario, irradiation in the aftermath of a nova can therefore speed-up the long-term evolution of the system. Furthermore, the effects of novae on low-mass donors might be more destructive than previously thought. Systems such as T Pyx, where the mass transfer rate is extremely high for its P_{orb} ($\sim 10^{-7}$ $M_\odot$ yr^{-1}), might provide evidence for an accelerated evaporation of secondary stars in the later stages of a CV due to nova explosions (Patterson et al. 2016). This, in turn, could remove short orbital period CVs from the population.

Chapter 4

The Missing link: PSR J1023+0038

or how to transition between pulsar and LMXB

"Eureka! It's the elusive missing missing link! This will show Banjo, once and for all!"

- Prof. Hubert J. Farnsworth, *Futurama - A Clockwork Origin*

I would like to acknowledge D. Altamirano, A. Archibald, J. Hessels., C. Bassa and R. Breton for useful discussions. Part of the work presented in this chapter was published in Hernandez-Santisteban et al. 2016c...

PSR J1023+0038 (also known as AY Sex for its optical counterpart) was originally classified as the first radio-selected CV candidate (Bond et al. 2002) with a $P_{orb} = 4.7548$ hr (Woudt et al. 2004). Independently, Szkody et al. (2003) presented SDSS spectra revealing a blue continuum with broad emission lines. Together with its X-ray emission, PSR J1023+0038 was then classified as a magnetic CV. However, a few years later, the system displayed a completely different spectrum, consistent with a mid-G spectral type donor and no signs of accretion. Surprisingly, time-resolved spectroscopy and photometry revealed the accretor mass to be $M_1 > 1.4$ M$_\odot$ (Thorstensen & Armstrong 2005). The system was later re-discovered as a bright MSP ($P_{spin} = 1.6879874440059(4)$ ms) with a low magnetic field ($\lesssim 6\times10^6$ G) during the Green Bank Telescope radio survey (Archibald et al. 2009). Deller et al. (2012) used VLBA radio observations to obtain a precise distance determination, $d = 1368^{+42}_{-39}$ pc, and a primary mass of $M_1 = 1.71 \pm 0.16$ M$_\odot$, confirming the neutron star as the primary component of the system. All of this evidence confirmed that the system had transitioned between a pulsar and an accreting state, and provided validation for the recycling scenario (see Section 1.4.3).

In June 2013, the γ-ray emission of PSR J1023+0038 increased by a factor ~ 5 (Stappers et al. 2013), and follow-up radio observations observed no pulsations and emission consistent with a jet-like outflow (Deller et al. 2015). Optical spectroscopy confirmed the presence of doubled-peak emission lines, indicating the presence of an accretion disc (Halpern et al. 2013; Linares et al. 2014a). This confirmed the transition of PSR J1023+0038 back to an accreting state and triggered a multi-wavelength campaign (Papitto et al. 2013a; Kong 2013; Takata et al. 2014; Wang et al. 2014) in order to characterise its properties. Figure 4.1 shows X-ray, UV and optical evolution of the system since the initial trigger up to the latest data collected by the *Swift* satellite[1].

Multiple models have been put forward to explain the multi-wavelength spectrum of the system during its recent accretion state. The L_X, arising from X-ray pulsations interpreted as evidence of accretion onto the NS, has been estimated as $\dot{M} \lesssim 6 \times 10^{-13}$ $M_\odot$ yr^{-1}(Papitto & Torres 2015). At such low mass-transfer rates, the accretion disc would be truncated far out from the light cylinder and thus would prevent any material reaching the NS surface. One way to circumvent this problem is to make a higher mass transfer rate and assume that only a small fraction of material slips through onto the NS, while the rest is ejected. If material is indeed reaching close to r_{co} ($\sim 20 - 30$ km from the NS surface), then a possible scenario to reproduce the bolometric spectrum is for the system to be in a propeller regime (Papitto et al. 2014a; Papitto & Torres 2015). As the LMXB system evolves, the mass accretion rate will decrease, eventually passing through a regime where a propeller occurs naturally (Illarionov & Sunyaev 1975). In this interpretation, the system is expelling around 99% of the material supplied by the donor, while the rest accretes onto the NS to produce the observed X-ray pulsations during the accretion state (Campana et al. 2016).

An alternative way to explain the multi-wavelength behaviour of the system requires the pulsar to be active even during the disc state (Stappers et al. 2014; Takata et al. 2014; Coti Zelati et al. 2014; Li et al. 2014). In this rotation-powered pulsar scenario, the accretion disc is truncated by the intense γ-rays from the pulsar wind, producing a disc with peak emission in the UV. The X-ray spectrum in the disc state is consistent with shock-powered emission produced by the interaction of the pulsar wind and outflow. This model is successful in reproducing the overall spectrum, but it fails to explain the X-ray pulsations, since it requires accreted material to approach the r_{co}. Furthermore, none of these models explain the random mode-switching in the X-ray and optical bands (see Section 1.4.4.1). In order to test and develop these models further, it is critical to better characterise the accretion flow observationally.

[1]The figure contains all the available data up to 28 April 2016. The X-ray light curves were processed by Swift-XRT online tool http://www.swift.ac.uk/user_objects/ (Evans et al. 2007; 2009). UVOT data were processed with HEAsoft v6.18 and the latest calibration files. I acknowledge the useful help of Kim Page in the learning process of Swift data reduction. This work made use of data supplied by the UK Swift Science Data Centre at the University of Leicester.

In this chapter, I present my contribution to the multi-wavelength campaign following the accreting state of PSR J1023+0038. I will focus on the analysis of ultraviolet spectroscopy and high-time resolution photometry obtained with *HST*. Then, I will discuss the results in the context of models for the accretion state of PSR J1023+0038 as well as tMSP evolution. One of my main findings is the discovery that the FUV properties of PSR J1023+0038 are closely analogous to those observed in a peculiar accreting WD system.

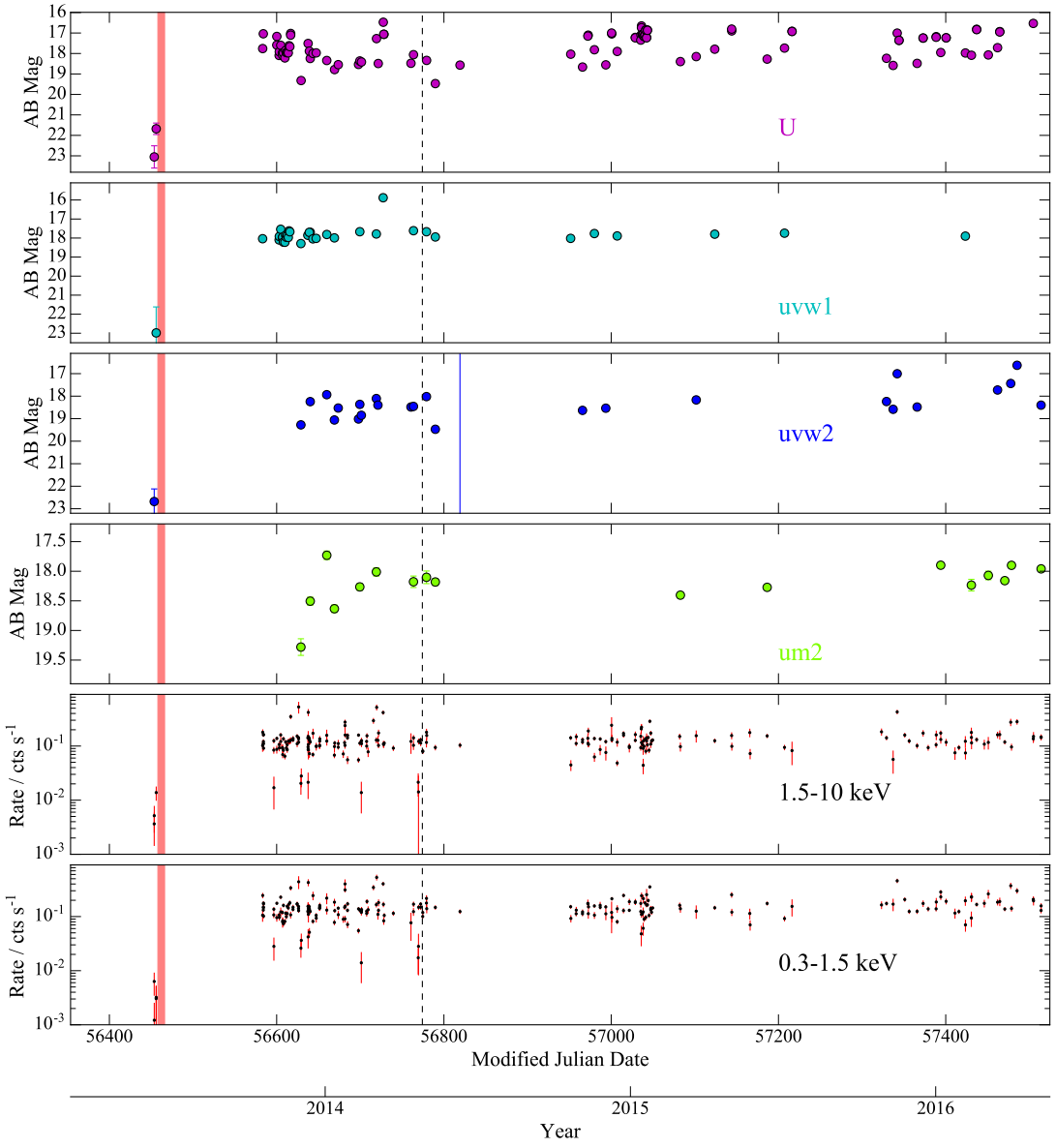

FIGURE 4.1: State transition of PSR J1023+0038 as seen by Swift-XRT/UVOT. The initial trigger (red line) and time of the HST observations (black dashed line) are shown for reference. Data has been binned per observation pointing.

4.1 HST Observations

The observations analysed in this chapter were taken in the far-ultraviolet (FUV) and near-ultraviolet (NUV) wavelength range with the *Hubble Space Telescope*[2] (HST) in response to a proposal for Director's Discretionary Time (DDT) [3] submitted in April 2014. The data comprise two visits, one dedicated to the FUV band, the other to the NUV band. The details of each visit are described below.

FUV observations were obtained with the Cosmic Origins Spectrograph (COS) for a total of 5 HST orbits, yielding a total exposure time of 11.9 ks (allowing for buffer dumps and visibility windows). Every orbit was divided into 4 sub-exposures: 420 s each for the first orbit (shortened by target acquisition) and 642 s for the rest. The observations were taken in TIME-TAG mode with a time resolution of 32 ms. The G140L/1105 grating was used to obtain a wavelength coverage from 1105 Å to 2253 Å at a spectral resolution of $R \sim 3000$. The data were reduced and extracted through the standard HST-COS pipeline[4]. All TIME-TAG events were corrected to a barycentric reference frame.

NUV observations were taken with the Space Telescope Imaging Spectrograph (STIS) for a total of 3 HST orbits, yielding a total exposure time of 8.3 ks. Every orbit consisted of one continuous integration of 2348.2 s for the first orbit and 2979.2 s for the rest. All observations were taken in TIME-TAG mode with a time resolution of 125 μs. We used the G230L grating and a 52×0.2 arcsec slit to achieve a spectral resolution of $R \sim 500$ in the range of 1570Å-3180Å. The spectra were reduced and extracted through the standard HST-STIS pipeline. All TIME-TAG events were corrected to a barycentric reference frame.

4.2 Spectroscopy

The FUV spectra are highly contaminated by geo-coronal emission from the atmosphere mainly from Lyα and OI 1301Å. In order to construct an average spectrum, I discarded all spectra where these lines were particularly bright, usually the first and second sub-exposures during every orbit as seen in Figure 4.10. During the fifth orbit with COS, a flare was observed in the system. I did not include these data in the following analysis (the flare is studied later on in detail in Section 4.4). The FUV average spectrum presents many strong, broad emission lines across a wide range of ionisation states, as seen in the top panel of Figure 4.2.

[2]Data were obtained through the Mikulski Archive for Space Telescopes (MAST). STScI is operated by the Association of Universities for Research in Astronomy, Inc., under NASA contract NASS-26555. Support for MAST for non-HST data is provided by the NASA Office of Space Science via grant NNX09AF08G and by other grants and contracts.

[3]PI: C. Knigge, DDT proposal number 13630

[4]http://www.stsci.edu/hst/cos/pipeline/

Some of the brightest emission lines are blended with adjacent features, so it is difficult to establish the individual contributions and the underlying continuum. Therefore, I limit the analysis to NV 1240 Å, SiIV 1400 Å and HeII 1640 Å, as representatives of the high ionisation lines. I subtracted the continuum by fitting a straight line to windows outside these lines. NV and SiIV emission lines are both doublets. So, I fitted a Gaussian profile to each individual component while fixing the theoretical separation and relative intensity[5]. I found a FWHM for NV to be 2231±250 km s^{-1} and for SiIV, 2622±340 km s^{-1}. The only line that presents a double-peaked profile is HeII 1640 Å. I fitted a double Gaussian with a variable separation between the peaks to this line. I found a FWHM= 1525 ± 250 km s^{-1} and a peak-to-peak separation of 720±200 km s^{-1}. These properties of HeII are consistent with other H and He lines observed in the optical region at the start of the outburst (Halpern et al. 2013; Linares et al. 2014a) and again ∼8 months after the HST observations (Coti Zelati et al. 2014).

The NUV average spectrum (bottom panel of Figure 4.2) has a very jagged and complex character. Its unusual shape is reminiscent of certain QSOs (Vestergaard & Wilkes 2001) which is attributed to FeII and FeIII emission lines. The spectrum is remarkably similar to the unique CV, AE Aqr (Eracleous et al. 1994; Eracleous & Horne 1996), as I will show and discuss in Section 4.6.1.

4.2.1 Spectral Energy Distribution

In order to study the overall emission of the system, I have constructed the full SED. For this, I combined the average UV spectra with quasi-simultaneous optical and NIR spectra obtained with X-Shooter[6], shown in Figure 4.3.

The combined spectrum was then dereddened using the Fitzpatrick (1999) reddening law and an estimated extinction value of E(B-V)=0.073 (obtained from the measurement of the hydrogen column density $N_H = 5.2 \times 10^{20}$ cm^{-2}, Coti Zelati et al. 2014; Shahbaz et al. 2015).

In order to dissect this SED, I modelled it with a combination of radiation produced by an optically thick accretion disc, F_{disc} (1.22, Shakura & Sunyaev 1973; King & Kolb 1995), and an irradiated donor star, F_{donor}. Therefore, the total continuum emission of the UV to NIR range is given by:

$$F_t = \frac{\cos i}{d^2} \cdot F_{disc}\left(\dot{m}, R_{in}, R_{out}\right) + \left(\frac{R_2}{d}\right)^2 F_{donor} \quad , \tag{4.1}$$

[5]Data taken from NIST Atomic Spectra Database Lines Data: http://physics.nist.gov/PhysRefData/ASD/lines_form.html

[6]These spectra were taken only ∼7 hours before the first HST orbit. The X-Shooter data were kindly provided by C. Bassa

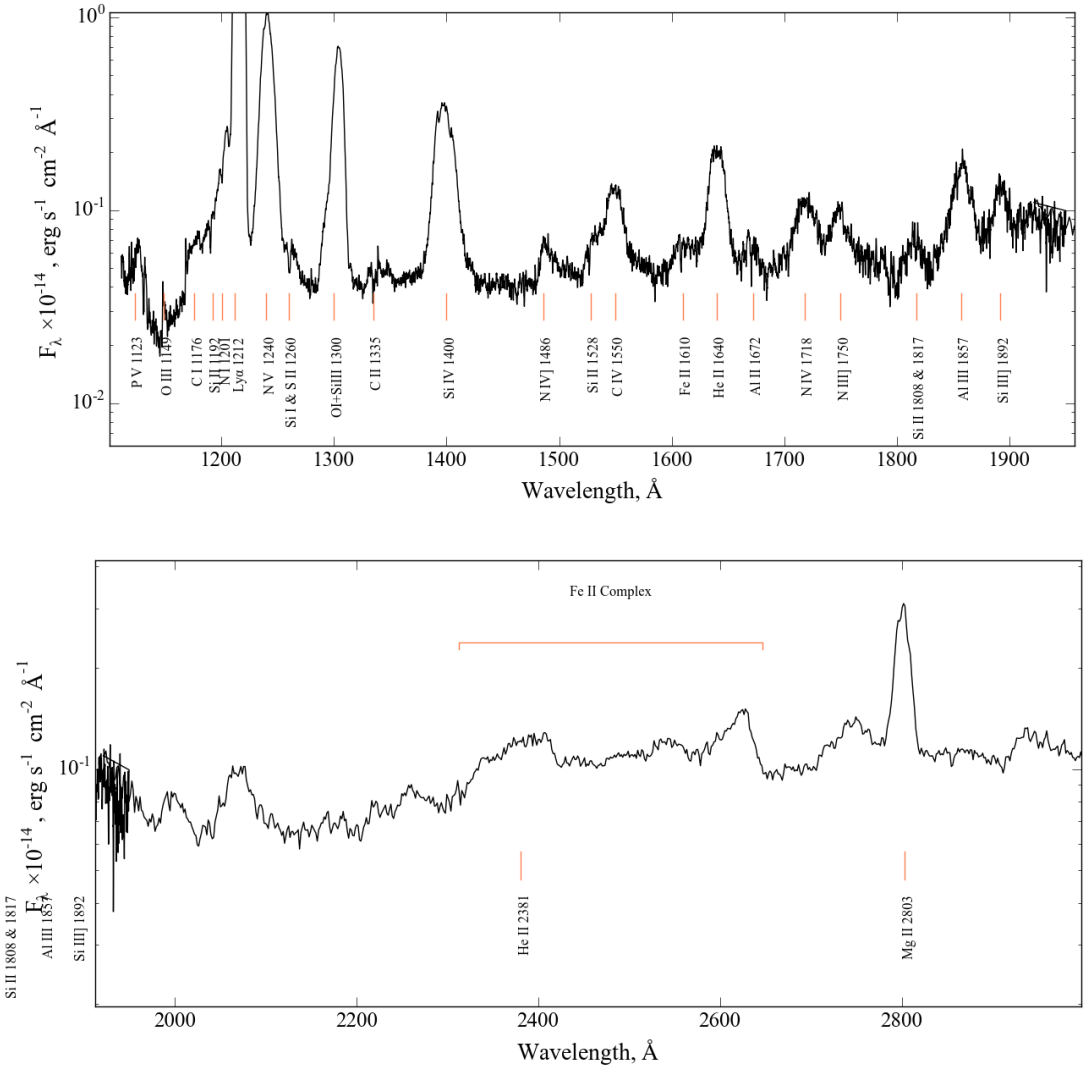

FIGURE 4.2: PSR J1023+0038 average spectra with line identifications. *Top* : FUV spectra. *Bottom*: NUV spectra

where R_{in} and R_{out} are the inner and outer radius of the accretion disc. The optical and NIR are mostly dominated by the irradiated G5V donor (Thorstensen & Armstrong 2005; Coti Zelati et al. 2014; Shahbaz et al. 2015). Combined NIR and mid-IR observations have revealed the donor to be mostly filling its Roche-lobe, even during quiescence (Wang et al. 2013). I therefore used a G5V synthetic spectrum (Castelli & Kurucz 2004) for the donor, F_{donor}. The emission and telluric lines, as well as regions with clear FeII features in the NUV, were masked so that the fit would trace only the underlying continuum.

To find the best fit, I explored the parameter space by using a MCMC procedure as implemented in EMCEE (Foreman-Mackey et al. 2013)[7]. I used a maximum likelihood

[7] http://dan.iel.fm/emcee/current/.

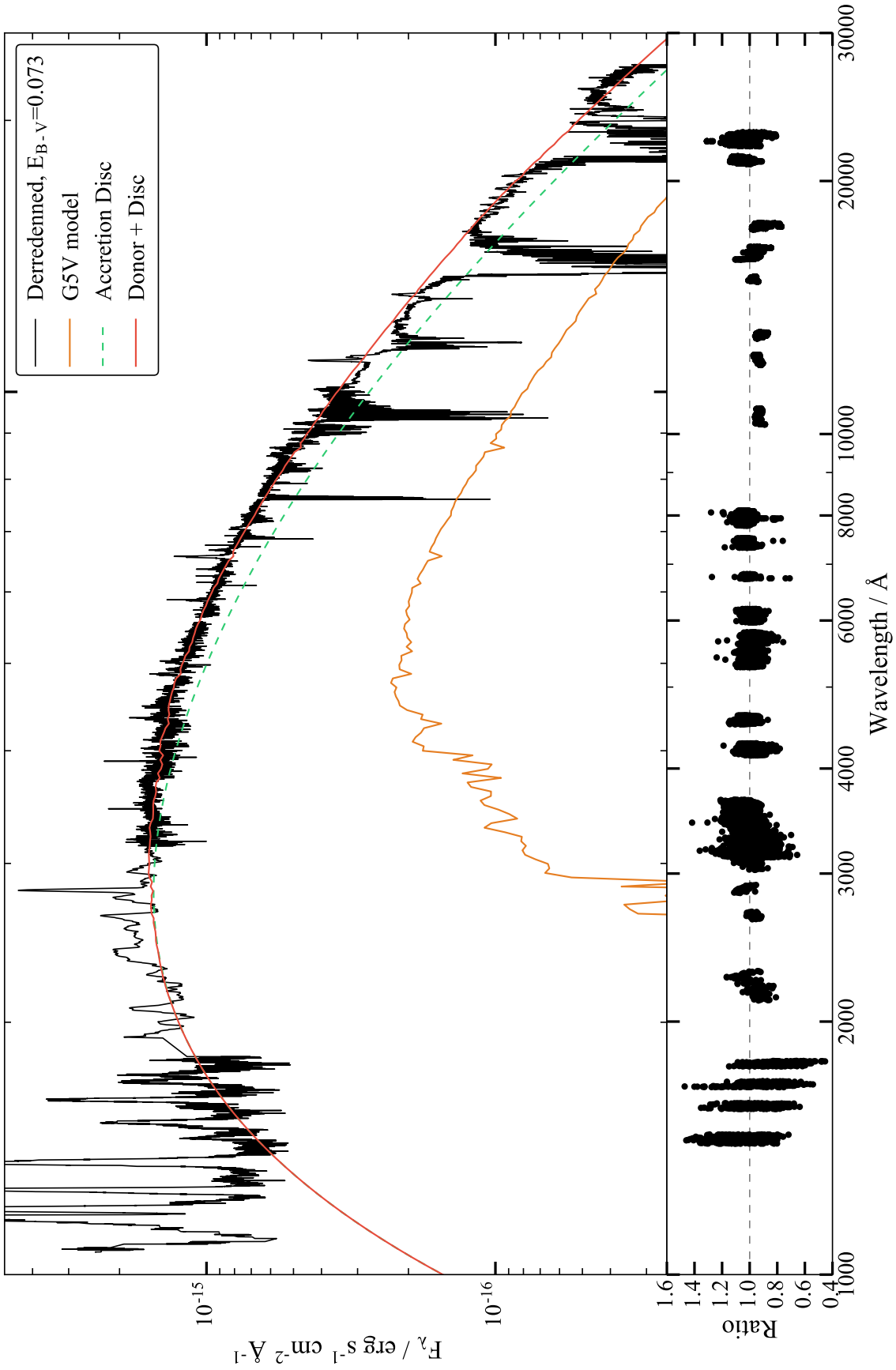

FIGURE 4.3: *Top* : Spectral energy distribution of PSR J1023+0038 from UV to NIR. The original spectrum (gray) has been dereddened (black) to enable a fit of the accretion disc parameters. The red line shows the best fit to the continuum generated by the addition of the donor (orange) and accretion disc (green). See text in Section 4.2.1 for details of the parameters. Telluric lines in the optical range have not been corrected. *Bottom* : Ratio between data and best-model.

as a measure of the goodness-of-fit:

$$\ln[F_t|A_{disc}, R_{in}, R_{out}] \propto \chi^2 = -\frac{1}{2}\left[\sum \frac{F_{t,i} - f_i}{\sigma_i}\right]^2 \quad . \tag{4.2}$$

In order to calculate the posterior probability of each model, I adopted the following priors for the parameters, defined as:

$$\begin{aligned} \log(R_{in}) &\sim U(7:10) \\ \log(R_{out}) &\sim U(9:11) \\ \cos(i) &\sim U(0:1) \\ \log(\dot{M}) &\sim U(-14:-8) \quad . \end{aligned} \tag{4.3}$$

I also established the condition that $R_{in} < R_{out}$. I used Gaussian priors for the remaining two parameters $R_2 = 0.39 \pm 0.07$ $R_\odot$($R_2 = R_L$, the volume-average Roche-lobe radius McConnell et al. 2015) and $d = 1368 \pm 42$ pc (Deller et al. 2012). Deller et al. (2012) present uneven limits for the 1σ confidence on the distance, therefore I assume the largest of the limits as the standard deviation in the Gaussian prior as an approximation. I employed 100 walkers and 1000 iterations, after discarding 1000 iterations as the burn-in period. The posterior probability distributions are shown in Figure 4.4. The marginal distributions are well described by Gaussians, so I could estimate the best fit parameters and their associated 1σ error as $R_{in} = 2.3^{+0.5}_{-0.3} \times 10^9$ cm, $R_{out} = 3.7^{+0.8}_{-0.5} \times 10^{10}$ cm and $\dot{M} = 3.6^{+3.6}_{-1.4} \times 10^{-10}$ $M_\odot$ yr^{-1}. The inner radius measurement is of particular interest, since it suggests that the accretion disc is truncated at $\sim$280 r_{lc} (where $r_{lc} \simeq 80$ km) far from the NS magnetosphere. A previous analysis using broad-band photometry also suggested a truncated disc structure with values consistent with this estimates (2×10^9 cm and 3×10^9 cm; Takata et al. 2014; Coti Zelati et al. 2014; respectively). The mass transfer inferred from the fit is higher than the observed in X-ray observations during the accreting phase, where $\dot{M} = 2 \times 10^{-11}$ $M_\odot$ yr^{-1} (Archibald et al. 2015).

As discussed in Section 2.1.1, the X-Shooter spectra may include a systematic error due to an absolute calibration. Furthermore, the intrinsic variability of the source may add extra scatter on the absolute normalisation of the model (with direct impact on i, d and R_2). However, the expected off-sets in the data will not change dramatically the overall shape of the SED, thus the estimate of the inner and outer radius of the accretion disc are robust.

4.3 Timing Analysis

The capability of both COS and STIS instruments to tag individual photons allowed me to perform a high resolution timing analysis. In addition, the data allows me to create energy-dependent light curves, as every photon is automatically provided with a

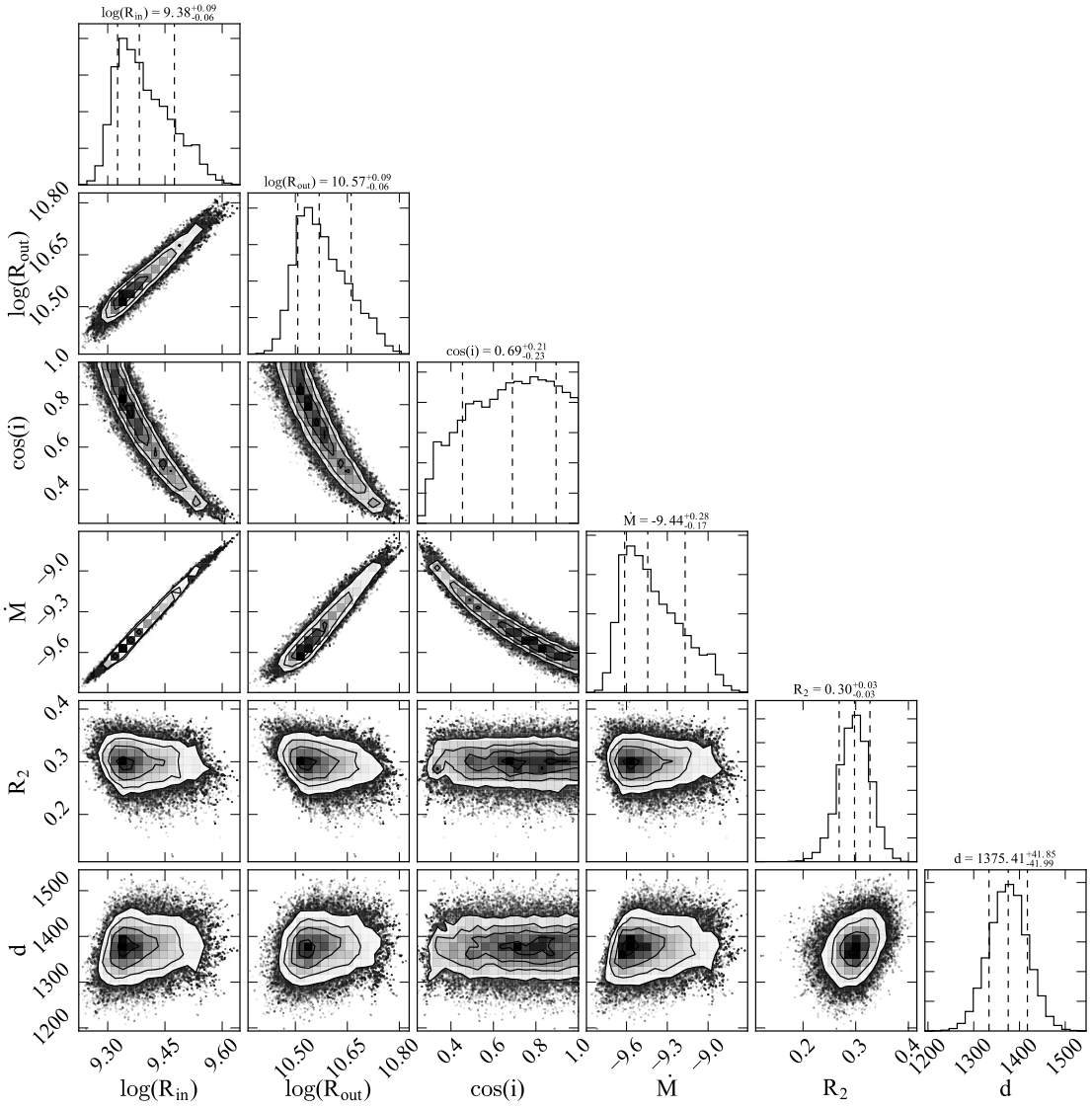

FIGURE 4.4: Posterior probability distributions for the accretion disc parameters. Colour scale contours show the joint probability for every combination of parameters. Contours represent the 1σ, 2σ and 3σ levels. Marginal posterior distributions are shown as histograms with the median and 1σ marked as dashed lines.

wavelength assignment. In this section, I present the results of the timing analysis on both datasets.

4.3.1 NUV

While the COS pipeline provides wavelength information for individual photons as part of the standard data products, the STIS instrument does not. Even though similar studies have been performed for flares in low-mass stars (Loyd & France 2014), no public release of code for such an analysis is available. Therefore, I developed my own

code to assign each individual photon to its corresponding wavelength, in a format that emulates the COS data products (for details see Appendix B).

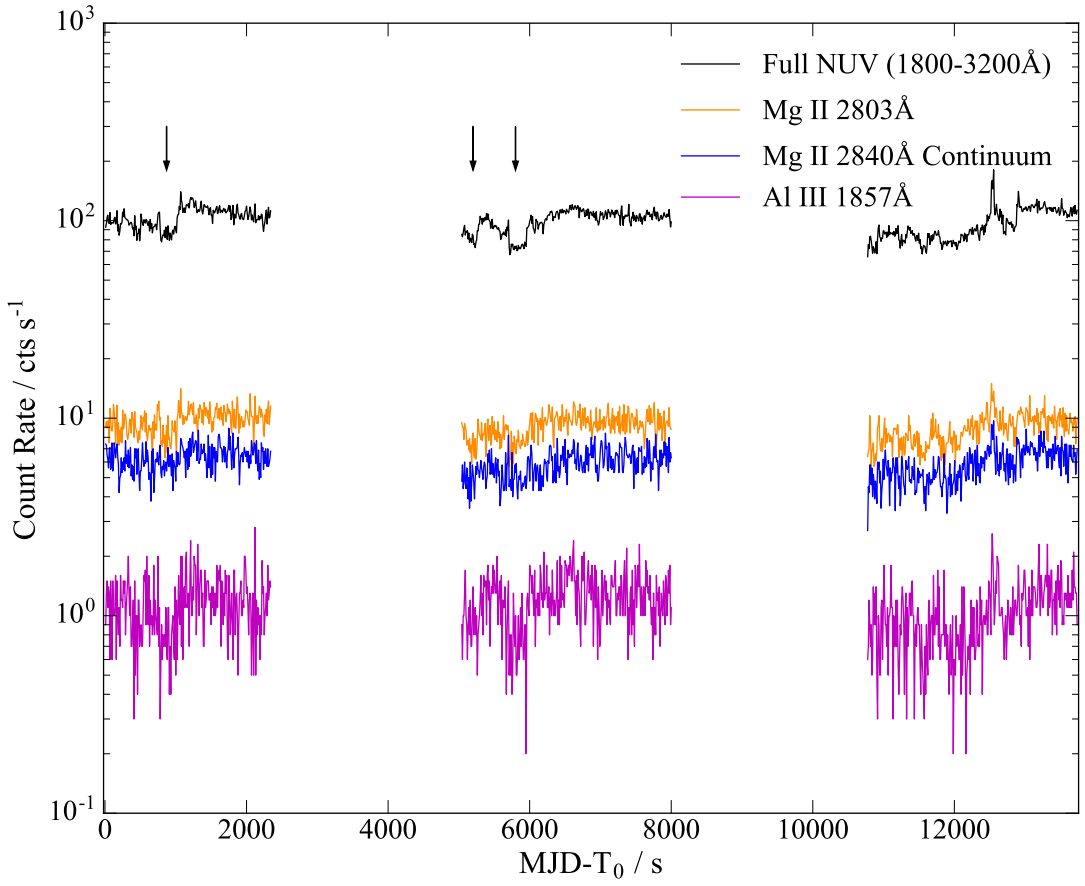

FIGURE 4.5: NUV lightcurves in 10 s bins.

The NUV light curves display broadly stable count rates throughout the three HST orbits, as shown in Figure 4.5 for the AlIII 1857 Å line, the MgII 2830 Å line and its adjacent continuum centred at 2840 Å. However, at times, the flux drops sharply (by a few percent), reminiscent of the mode-switching observed in X-rays (Bogdanov et al. 2015; Archibald et al. 2015) and at optical wavelengths (Shahbaz et al. 2015). There are hints of rectangular dips in the light curves (marked with arrows in Figure 4.5), which are observed in both the lines and the continuum. However, they are not as frequent as observed in X-rays (Bogdanov et al. 2015) or in red optical bands (Shahbaz et al. 2015).

The X-ray and optical light curves present bi-modal distributions of the count rates, observed as evidence for high and low modes (Archibald et al. 2015; Shahbaz et al. 2015). In Figure 4.6, I show the histogram of the count rates for the full NUV range using the 10-s bin light curve. Although the distribution is not clearly bi-modal, there are signs of an extended tail at lower count rates, with a possible bump. In order to assess the possible bi-modality of this distribution, I have employed a Gaussian mixture

modelling (GMM, Muratov & Gnedin 2010) to the NUV light curve. The data favours a bi-modal Gaussian distribution over a uni-modal distribution at a confidence level better than $P < 0.001$. The two distributions are centred at 85.5±1 counts s^{-1} and 107±1 counts s^{-1}.

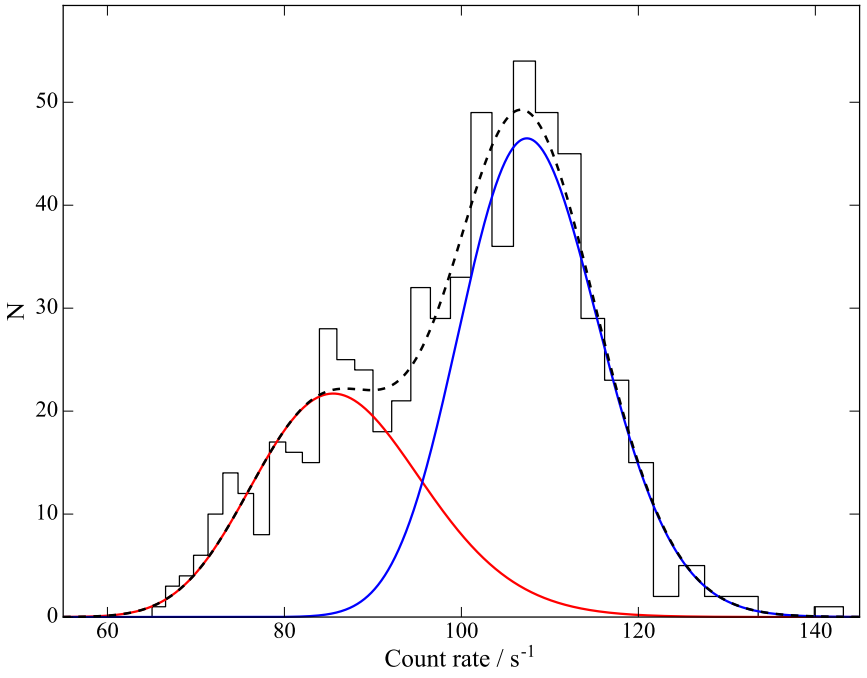

FIGURE 4.6: NUV count rate histogram in 10-s bins. I show the best bi-modal Gaussian distribution decomposition from the GMM analysis.

Close inspection reveals a connection within the NUV data, with both lines and continuum showing matched features. In order to study these correlations, I carried out a cross-correlation function (CCF) analysis. For this, the light curves were binned in 1 s and 10 s, in order to probe different timescales with maximum signal to noise. The 1-s CCFs in the left panel of Figure 4.7 show a spike at $\tau = 0$ s, but the coefficient is too low to be statistically significant. However, in the 10 s bin CCF (right panel), the maximum of the CCF peaks at $\tau = 0$ s, with a coefficient ~ 0.6. I found no lag in any of the CCFs computed.

The time resolution of STIS (125 μs) allows me to probe frequencies up to the spin period of the neutron star in PSR J1023+0038, $f_{spin} \simeq 600$ Hz (Archibald et al. 2009). Therefore, I computed the Fast Fourier Transform (e.g. van der Klis 1989) at the full instrumental time resolution. The power density spectra (PDS) for the three orbits show no evidence for coherent signals nor for quasi-periodic oscillations (QPOs) up to the Nyquist frequency ($\nu_{nyq} = 4000$ Hz), as shown in Figure 4.8. The PDS are consistent with white noise above 0.5 Hz, with a red noise component at lower frequencies. In order to characterise the red noise component, I rebinned the PDS logarithmically and rms-normalised by subtracting the white noise level (Leahy power = 2), while estimating a

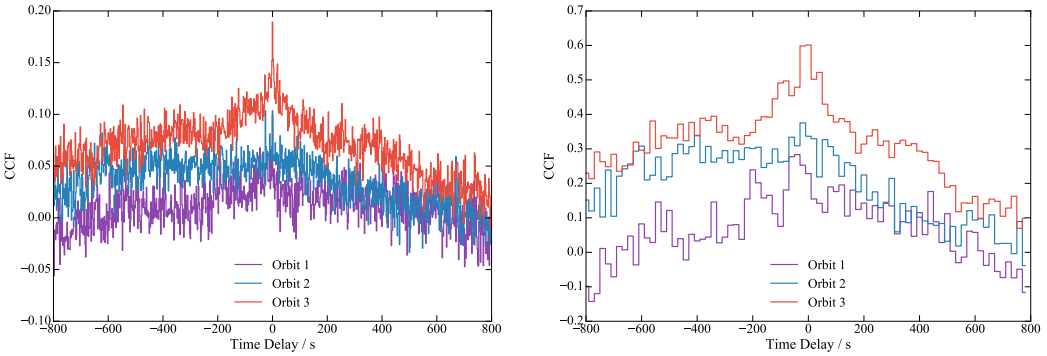

FIGURE 4.7: Cross-correlation functions between the MgII emission line and continuum. The CCF has been computed for every individual orbit with two different time bins: 1s (left) and 10s (right).

background count rate near the target on the detector. Errors in the PDS were calculated by adding in quadrature the data inside the new bin (errors on the full resolution PDS are 100% per point). Finally, I performed a least-squares fit of a simple power law, $P_\nu \propto \nu^\alpha$, to each PDS. I found the optimal spectral index for each orbit, shown as red lines in Figure 4.9, to be -1.19 ± 0.09, -1.45 ± 0.10 and -1.38 ± 0.10, respectively. These values are consistent with previous observations of PSR J1023+0038 in the optical (Shahbaz et al. 2015). Broad red-noise signals with power law indices between -1.0 and -2.0 have also been observed in other LMXBs and CVs (Hynes et al. 2003).

4.3.2 FUV

The FUV light curves, shown in Figure 4.10, highlight the behaviour of the 1303 Å geocoronal, SiIV 1400 Å and its adjacent continuum, CIV 1550 Å and HeII 1640 Å. The geocoronal line is very bright during the first exposures of every orbit, due to daytime air glow in the atmosphere; this decreases after 1-2 exposures. Then, the light curves follow the trend of the other lines, as well as the continuum. Aside from the clear flux variations throughout all orbits, there is a sudden increase in the count rate by a factor of ~ 5, during orbit 5. I will explore this independently in Section 4.4. The data does not present any clear modulation on the orbital period of 4.7 hr. The length of the observations is just under two binary orbits and the length of an HST orbit is $\simeq 1/3$ of a binary orbit. As a result, the observations produce a sparse light curve after phasing on the orbital period.

As with the NUV light curves, both emission lines present variability on different time scales and appear to be correlated with the continuum, as shown in Figure 4.10. To explore this further, I calculated the CCF between the different line species, as well as between the lines and the continuum (as an example, I show the highest signal to noise SiIV in Figure 4.11). The light curves were binned in 5 s bins. In all cases, the CCF

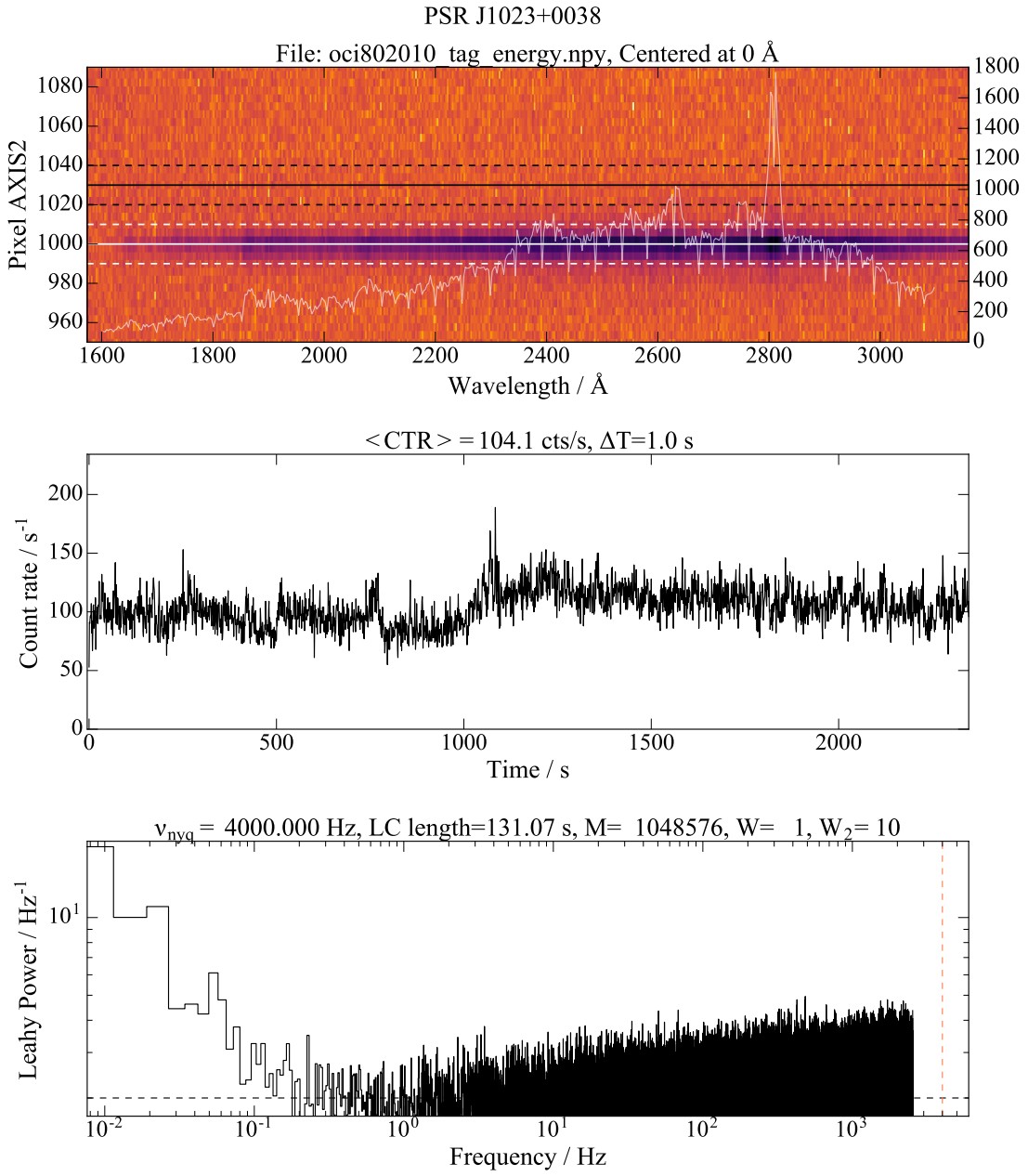

FIGURE 4.8: Lightcurve extraction of STIS data of the full slit of PSR J1023+0038. *Top* : Localisation of the slit in the image in pixel coordinates (white) and the background region (black). The summed spectrum is shown for reference. *Middle* : The full light curve constructed in 1 s bins, shown only for reference. *Bottom* : Power density spectrum constructed by binning the light curve at 125 μs.

presented a maximum at a lag $\tau = 0$ s and with a coefficient ~ 0.7. I found no lag between any of the CCFs computed.

I performed a similar analysis to the individual sub-exposures in the COS dataset. This resulted in 20 PDS similar to the one presented in Figure 4.12. As with the NUV data, the PDS present a clear red-noise spectrum at lower frequencies, while white noise at

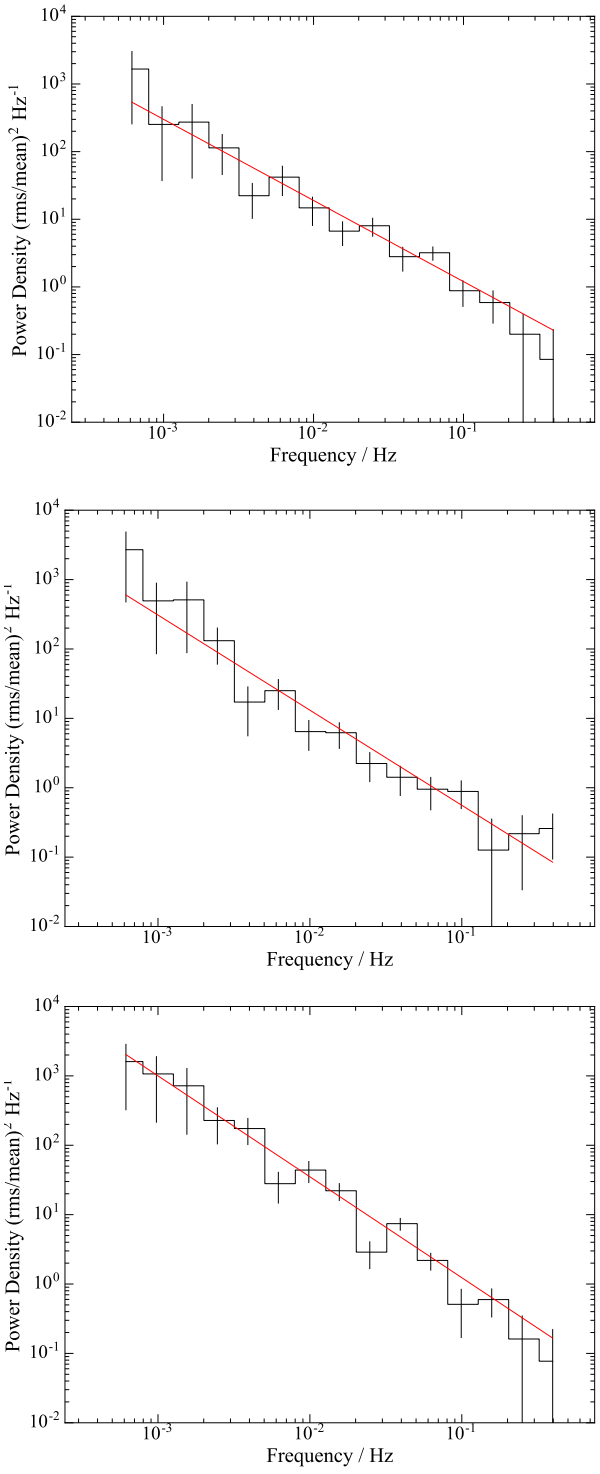

FIGURE 4.9: Power density spectra for each STIS orbit. White noise level has been subtracted and rebinned in logarithmic space. The red line shows the best fit power law.

higher frequencies. No QPO nor coherent pulsation was detected. Interestingly, the red-noise component cut-off varies from orbit to orbit, especially during the flare.

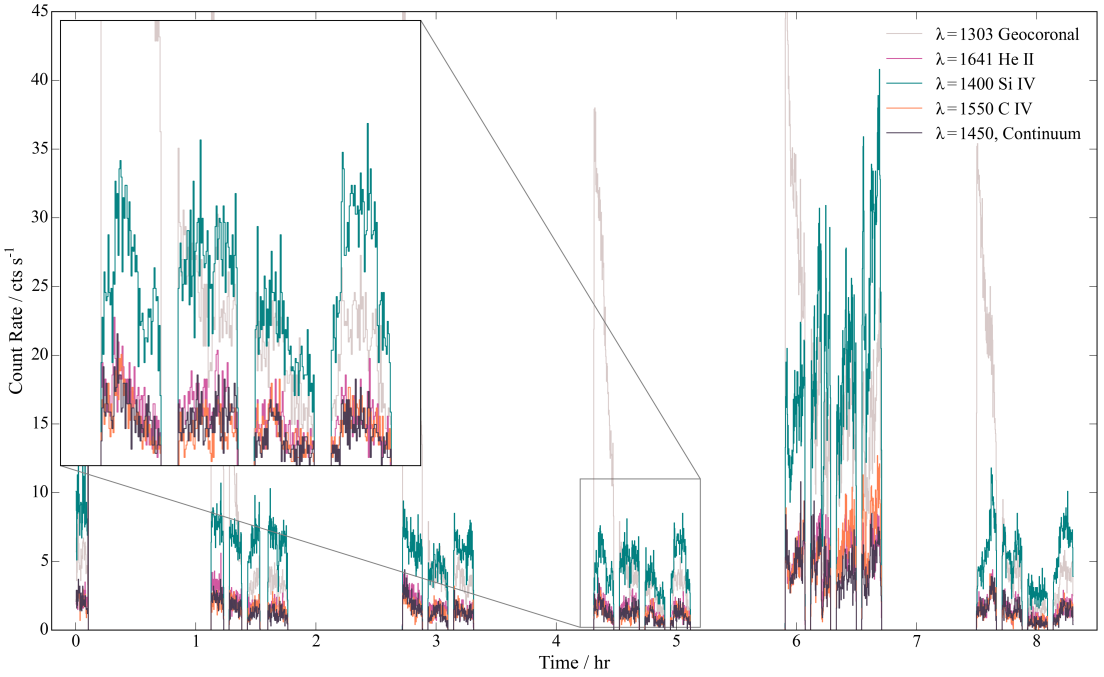

FIGURE 4.10: FUV lightcurves in 10 s bins. Time is given since the start of the first observation. Geocoronal emission is dominant in the first two exposures of each orbit.

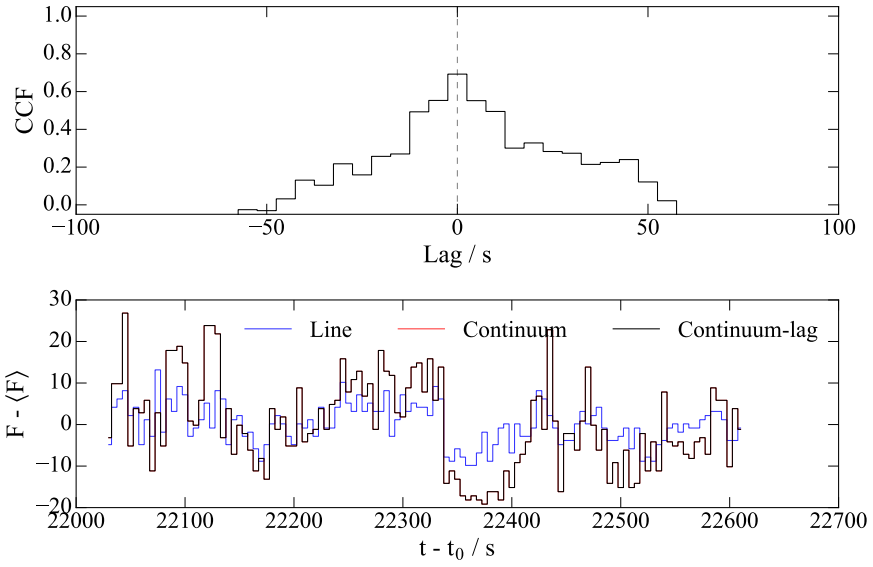

FIGURE 4.11: Cross-correlation functions between the SiIV emission line and the adjacent continuum. *Top* : The CCF has been computed for every individual orbit in 5s time bins. *Bottom* : The light curves of both line and continuum, as well as the corrected one by the lag found in the CCF.

4.4 Flare

The COS dataset contains a flare lasting ∼1 orbit during the 5th orbit of the observations. During this time, the count rate increased by a factor of ∼ 3 overall. The light

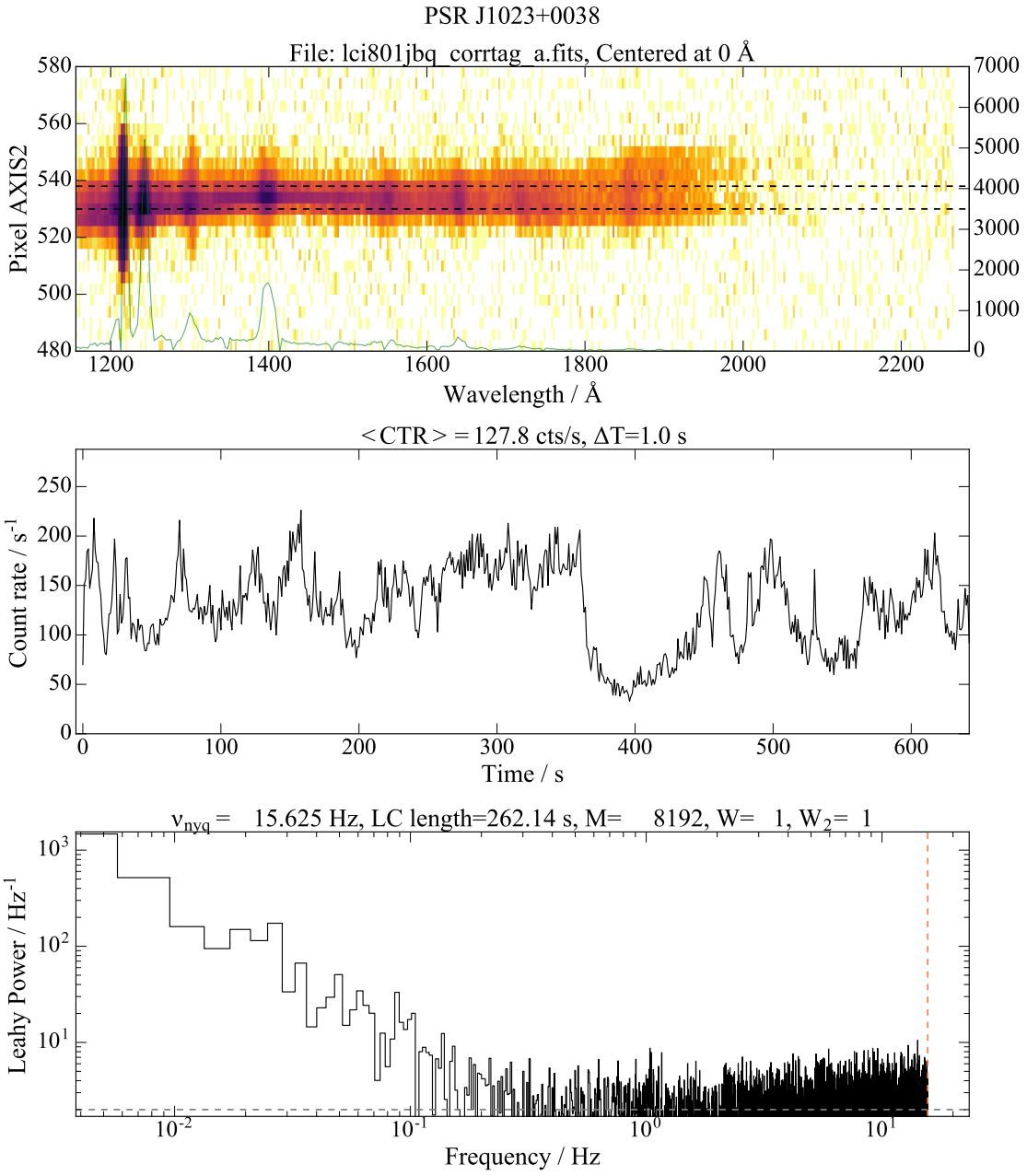

FIGURE 4.12: Light curve extraction of COS data of the full slit of PSR J1023+0038. *Top* : Localisation of the slit in the image in pixel coordinates (white). The summed spectrum is shown for reference (green). *Middle* : The full light curve constructed in 1 s bins, shown only for reference. *Bottom* : Power density spectrum constructed by binning the lightcurve at the instrument temporal resolution of 32 ms.

curve, shown in Figure 4.10, has otherwise similar properties to those seen in the *normal* state. Both the lines and the continuum are correlated with no apparent lag between them. However, the emission spectrum does present some important differences. In order to analyse and characterise these, I constructed average spectra of the flare and normal state. In doing so, I carefully avoided any sub-exposures where geo-coronal lines are clearly present (usually the first two sub-exposures in each orbit). Then, I fitted a

3rd-degree polynomial to the continuum (masking the emission lines) and subtracted it from each average spectrum, as shown in Figure 4.13. The two spectra present the same emission lines, but their strength increases by different amounts during the flare. The lines seem to rise with the continuum with no apparent lag, as shown in Section 4.3. In order to quantify the changes in the line spectrum during the flare, I integrated the flux of the individual lines and evaluated the ratio between them. The emission in most lines increases by a factor ~ 4. However, CIV and NIV, which have similar ionisation potentials seem to be higher with a factor close to ~ 8.

The presence of semi-forbidden lines of NIII], NIV] and SiIII] is an interesting characteristic of the FUV spectra, as they can provide constraints on the density of the emitting regions. I have used CHIANTI v.8.0 (Del Zanna et al. 2015) to estimate the critical densities for the different ion species, shown in Table 4.1. The NIII] line provides the best constraint on the critical density in the line-forming region, with $n_e < 8.7 \times 10^9$ cm^{-3}.

ion	Energy / eV		λ_0	Critical Density	F_{flare}/F_0
	Create	Ionise	Å	cm^{-3}	
PV			1124.0	...	9.80 ± 0.50
NV	77.7	97.9	1240.0	...	4.47 ± 0.02
SiIV	33.5	45.1	1400.0	...	4.33 ± 0.03
NIV]	47.4	77.7	1486.0	1.6×10^{10}	
CIV	47.9	64.5	1550.0	...	7.90 ± 0.20
NIV	47.4	77.7	1718.0	...	8.40 ± 0.40
NIII]	29.6	47.4	1750.0	8.7×10^{9}	
SiII	8.2	16.3	1811.5	...	1.00 ± 0.70
AlIII	18.8	26.4	1859.0	...	3.80 ± 0.20
SiIII]	16.3	33.5	1892.0	1.2×10^{11}	

TABLE 4.1: Ionisation Potential of the flare in PSR J1023+0038.

4.5 Anomalous Abundances

One of the possible models to explain the state transition in tMSPs is via a cycle induced by the energetic pulsar wind (S.Phinney priv. comm.)[8]. This wind can deposit heat via absorption of $\gamma-$rays deep inside the convective envelope of the donor, causing the companion to increase its radius just slightly, enabling RLOF. This mass transfer allows the system to enter the accreting state. Material will build up in the accretion disc, and eventually suppress the pulsar wind due to in-falling material onto the NS. This may, prevent $\gamma-$rays from reaching the companion, allowing the donor to contract and cease mass transfer. The disc, however, will then empty on its viscous time scale ($\sim 1-10$ yr), consequently allowing the NS to enter the MSP state again. The pulsar wind will then resume and re-start the cycle.

[8]S. Phinney initially presented this model at the 8th Bonn workshop on *Formation and Evolution of Neutron Stars* in Bonn, Germany (30 November 2015)

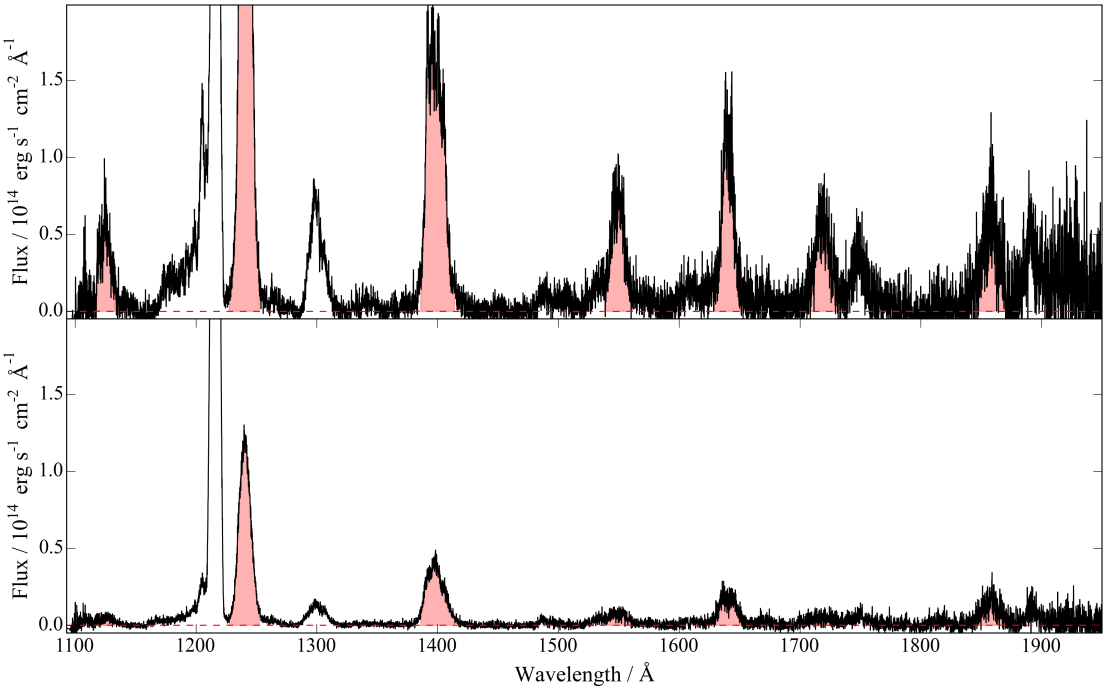

FIGURE 4.13: Flare spectrum of PSR J1023+0038. *Top:* Continuum-subtracted spectrum of the average flare. *Bottom:* Continuum-subtracted spectrum of outside a flare, used as a reference to obtain the relative change of the emission lines.

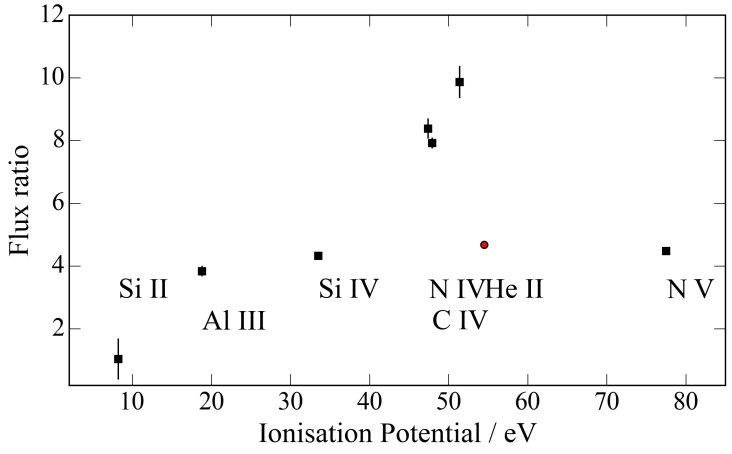

FIGURE 4.14: Ionisation potentials of the flare vs. non flare emission line ratios.

A key prediction of this model is the creation of anomalous abundances on the companion of lithium, boron and beryllium via spallation. Therefore, any traces in the accretion flow or outflow might provide direct evidence for this model. In particular, the UV region contains several strong lines, primarily of boron and beryllium. I manually inspected the UV regime for evidence of such BI, BII and BeI lines. However, I found no trace of any of these elements.

4.6 Discussion

The ultraviolet HST observations of PSR J1023+0038 have provided a unique insight to the accreting state of a transitional millisecond pulsar. The accretion disc in these systems was thought to peak in the UV, based on broad band optical photometry. In particular, Coti Zelati et al. (2014) and Takata et al. (2014) reported a value for the inner radius for the disc of $R_{in} \sim 250 r_{lc}$. This already provides for tension between models that make attempts to explain the observed mode switching, since they require the disc to be near the co-rotation radius (e.g. Ertan (2015)). However, the FUV and NUV range present rich and complex spectra, so any inference from broadband photometry alone may not give a reliable picture of the properties of the accretion disc.

The estimate of $R_{in} \sim 240 r_{lc}$, as calculated in 4.2.1 based on the global SED, is consistent with the picture of a truncated disc in PSR J1023+0038. Specifically, it seems to confirm that the disc is truncated way beyond the NS magnetosphere. In this picture, there should then be no accretion. However, recently discovered X-ray pulsations modulated on the spin period suggest that accretion onto the magnetic poles of the NS is occurring (Archibald et al. 2015). Therefore, how can the accreted material reach the NS? A possible mechanism is via advection-dominated accretion flows (ADAFs). This results when the mass accretion rate becomes so low that the density in the gas drops enough that the cooling becomes radiatively inefficient. Thus, the energy released by the accretion disc gets trapped, forcing it to expand and become optically thin. The flow can no longer be treated in the thin disc approximation and thus will not emit as a classical multi-blackbody spectrum. This scenario has been proposed as a mechanism to transport material in quiescent black-hole (Narayan et al. 1997; McClintock & Remillard 2000) and neutron-star binaries (Menou et al. 1999). These models propose a discontinuity in the flow between the Keplerian disc and the ADAF flow. However, the location of this truncation radius as well as the influence of the NS emission on the flow close to its surface, are still unclear in this scenario.

The *Swift* and *NuSTAR* light curves present luminosity variations from $\sim 5 \times 10^{32}$ erg s^{-1} in the low states, to an average level of $\sim 6 \times 10^{33}$ erg s^{-1}. These variations occur with no apparent correlation between the length of the dip or the time between dips. The typical time scale for these variations is 10 s$-$100 s, which corresponds to orbital radii of 7.8×10^8 cm and 3.6×10^9 cm, respectively (Patruno et al. 2014). These radii are outside the light cylinder, and remarkably similar to the inner radius I estimated for the truncated disc. This might indicate that the obscuring material could be associated with the inner edge of the accretion disc. The tentative evidence for a bi-modal distribution in the NUV flux is less convincing than in X-rays and other optical bands (e.g. Archibald et al. 2015). Recently, analysis of optical photometry with the K2 mission (Howell et al. 2014) on the well known LMXB, Sco X-1(Giacconi et al. 1962) has revealed a very

similar flux distribution in both optical and X-ray (Hakala et al. 2015; Scaringi et al. 2015a; Hynes et al. 2016).

4.6.1 AE Aqr: A tMSP twin

The idea of a propeller to explain the high-energy spectrum of PSR J1023+0038 has been explored by several authors, most recently Papitto & Torres (2015). They construct a model where the $\gamma-$ray emission in tMSPs is generated by a propeller mechanism due to self-synchrotron Compton emission originating at the inner radius of the disc when it penetrates the light cylinder (e.g. Section 1.4.2.1). This model reproduces successfully the X-ray and $\gamma-$ray regions of PSR J1023+0038's spectrum. However, as shown in Section 4.2.1, the inner disc does not actually seem to reach the NS magnetosphere.

A useful prototype of a propeller system is the magnetic white dwarf system AE Aqr (Patterson & Raymond 1985). Here, the magnetospheric radius of the WD also truncates most of the disc and most of the material transferred from the donor is expelled from the system (Wynn & King 1995; Wynn et al. 1997).

AE Aqr is a well studied system over a wide spectral range, particularly in the UV (Jameson et al. 1980; Eracleous et al. 1994; Eracleous & Horne 1996). A direct comparison between the two sets of spectra reveals remarkable similarities. In Figure 4.15, I show the smoothed average spectrum of PSR J1023+0038, scaled in order to compare it directly with AE Aqr. Both spectra show similar ionisation species, including the presence of the same semi-forbidden lines. The strongest resemblance occurs in the NUV spectra where unique features associated with the FeI and FeII complex in emission are observed. Besides the similarities between their spectra, the temporal variation of the lines in both systems also show similarities. There seems to be almost no lag between line and continuum variations (AE Aqr: Eracleous et al. (1994), PSR J1023+0038: Section 4.3), suggesting a common region where both are generated. Like PSR J1023+0038, AE Aqr produces sporadic flares, with the changes between the different states showing similar behaviour (i.e. different change among ionisation species, maximum strengthening of the lines at a certain ionisation energy). All this fits together when explained as a collision between *diamagnetic blobs* of ejected material. Therefore, the flare is the result of such a collision i.e. the radiative cooling of the expanding fireball (Eracleous & Horne 1996). This scenario was further supported via interpreting Hα Doppler tomograms of AE Aqr in light of simulations of these blob-blob collisions (Wynn & King 1995; Wynn et al. 1997).

Radio emission in AE Aqr presents a shallow spectrum with a spectral index $\alpha \approx 0.38$ from 4.9 to 87.7 GHz, with variability in flux as well as in the spectrum due to flaring activity (Abada-Simon et al. 1993). These values are similar to recent radio observations of PSR J1023+0038 with the Very Large Array where a flat spectrum is also observed

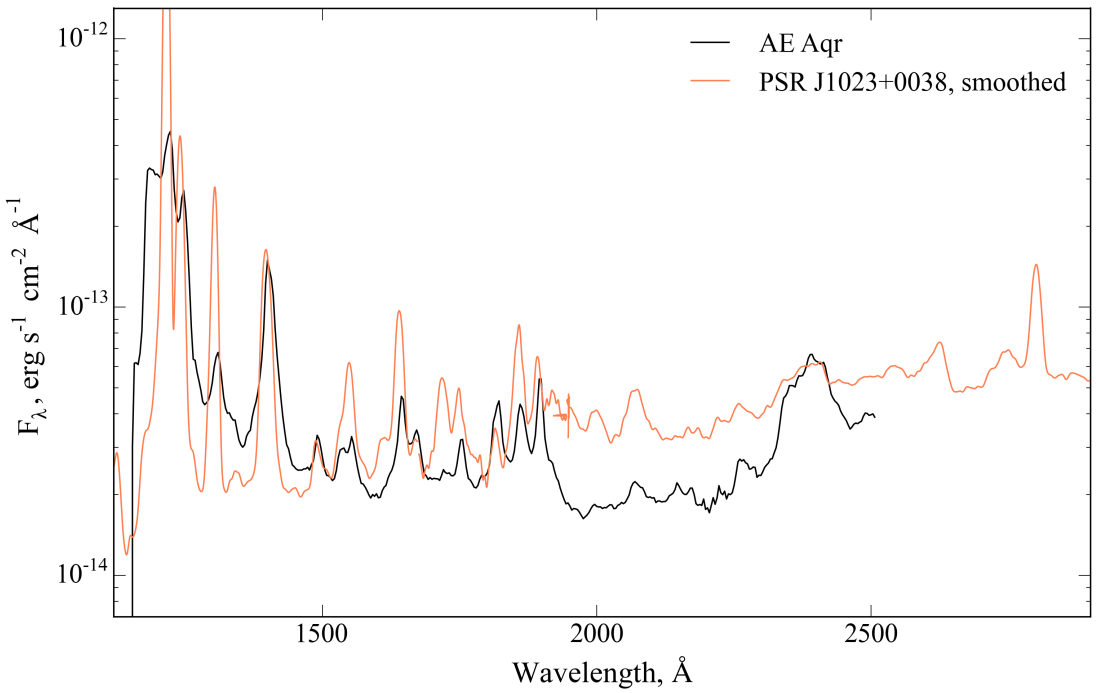

FIGURE 4.15: Comparison of UV spectra between AE Aqr and PSR J1023+0038. The average HST spectrum has been smoothed to the resolution of the AE Aqr data and scaled for comparison (M. Eracleous priv. comm.)

with a median spectral index $\alpha \approx 0.04 \pm 0.3$ at 10 GHz (Deller et al. 2015). Deller et al. (2015) interpret their results in the framework of a collimated jet but they do not observe any polarisation or any other evidence for a collimated outflow. On the other hand, these properties, as well as the timescales of the observed radio variability, are similar to the emission in AE Aqr. This is thought to be due to synchrotron radiation by relativistic electrons in the propeller outflow.

Baglio et al. (2016) revealed evidence of optical polarisation in PSR J1023+0038, with a decreasing fraction towards the NIR. However, the SED is very well reproduced by the superposition of the accretion disc and donor, particularly in the NIR (also exemplified in the fit in Section 4.2.1). In contrast with Deller et al. (2015), they interpret their results as evidence for induced polarisation via Thomson scattering in the bright accretion disc (or outflow) instead of synchrotron radiation from a relativistic jet.

Although it is tempting to use AE Aqr as an analogous system to transitional millisecond pulsars, there are still some unexplained traits of PSR J1023+0038 that make the comparison difficult. In AE Aqr, the electromagnetic radiation is two orders of magnitude lower than the measured spin-down luminosity (1.1×10^{34} erg s^{-1}, Eracleous & Horne 1996). This implies that the system is using the remaining energy to drag and expel $\sim$99% of the accreted material. In the case of PSR J1023+0038, radio observations during quiescence provide a precise estimate of the spin-down luminosity, $L_{sd} = 4.4 \times 10^{34}$

erg s^{-1} (Archibald et al. 2013). The discovery of X-ray pulsations on the spin period (the smoking gun of accretion, Archibald et al. 2015) also prompted long cadence X-ray monitoring of the source throughout the outburst, which constrained the spin-down rate in the accreting state, $\dot{P}_{accr}$, to be comparable with that inferred from radio observations in quiescence, $\dot{P}_{accr} = \dot{P}_{radio}(1 \pm 0.08)$ (A. Jaodand priv. comm.). A similar result has been found in XSS J1227.0-4859 where the peak X-ray luminosity observed with *NuStar* ($L_X \simeq 1.2 \times 10^{34}$ erg s^{-1}) is a significant fraction of L_{sd}. Thus if there is a substantial outflow in the system, it must be carrying a very small fraction of the total energy, in direct contrast to AE Aqr.

Chapter 5

Conclusions and Future Work

The projects that integrate this thesis present multi-wavelength observations that investigate the late evolution of CVs and the accretion state of tMSPs. In this Chapter, I summarise the main results and discuss future work suggested by the research outlined in this thesis.

5.1 The late evolution of CVs

The work presented in Chapters 2 and 3 have tackled two aspects of the late evolution of CVs. First, the time-resolved optical and NIR spectroscopy of SDSS J1433+1011, allowed us to perform a study of a candidate sub-stellar donor in a cataclysmic variable. By dissecting the contribution of the optically brighter WD and accretion disc, I was able to directly detect the full SED of a L1±1 brown dwarf. The radial velocity analysis of the absorption lines in the atmosphere of the donor, allowed us to measure a $M_2 = 0.054 \pm 0.04$ $M_\odot$, confirming the first transition of a star into a brown dwarf in an accreting white dwarf. This is a vindication of the evolutionary models for CVs.

Second, in Chapter 3 I developed a proof-of-concept project, in order to search for the oldest period bouncers, where the mass transfer rate is so low that the system might be indistinguishable from an isolated WD, in other words, a *dead* CV. If these dead CVs have sub-stellar companions, then eclipsing systems will present high-signal to noise eclipses observed as dropouts or non detections. The vast amount of multi-epoch data generated by large synoptic surveys provided ideal conditions to carry out such a project. I created a sample of candidate WDs in the well-observed region *Stripe 82* and retrieved the photometric data from two surveys: SDSS and PTF. I developed a pipeline that searched in both surveys for dropouts in ∼2,600 WD candidates. In total, a sample of $\sim 10^6$ individual measurements were analysed, spanning over 5 years of observations.

The null detection of eclipsing WDs allowed me to constrain, for the first time, the space density of dead CVs. I employed a Monte Carlo simulation of the Galactic population and, by applying the observational cuts used in the PTF sample, I was able to derive an upper limit of $\rho_0 < 2 \times 10^{-5}$ pc^{-3} for systems with typical WD temperature of 10,000 K. This value is lower than predicted by the most optimistic theoretical estimates (e.g. Politano 1996). However, recent theoretical studies (Goliasch & Nelson 2015; Schreiber et al. 2016) have suggested space densities much closer to observational ones (Pretorius & Knigge 2012) and in line with the upper limit found in this work.

5.1.1 Future work

It is evident that, if we are to understand this late evolution, both characterisation of individual systems and large surveys, are required. One of the main problems in locating period bouncers is the ability to select candidates systems. However, the multi-coloured nature of next-generation surveys, such as the *Large Synoptic Survey Telescope* (LSST, Ivezic et al. 2008) and the *Javalambre J-PAS* survey (Benitez et al. 2014), will allow us to perform a clear selection of candidate WDs in a large area of the sky. Furthermore, the temporal information will allow us to discover this hidden population or constrain even further the lack of period bouncers. Many of these new candidates, however, are very faint and require large telescope facilities (such as VLT) in order to retrieve their dynamical parameters. Despite this, there exists a strong candidate list of period bouncers awaiting characterisation. The independent determination of q via superhump measurement during outbursts (Patterson 2011), can allow us to trace systems that may otherwise be undetectable.

5.2 Sub-stellar atmosphere test-beds

In Chapter 2, I used the time-resolved data to estimate the average irradiation-induced temperature difference between the day- and night-side of the sub-stellar donor (57 K) and the maximum difference between the hottest and coolest parts of its surface (200 K). I modelled the observations with a simple geometric reprocessing model and found an upper limit to the bolometric (Bond) albedo $A_B < 0.54$ at 2σ confidence level. Also, I was able to constrain the lateral heat redistribution efficiency $\epsilon < 0.54$ at 2σ. This implies that the sub-stellar object presents a high reprocessing efficiency but poor redistribution, consistent with previous studies of hot-Jupiters (Cowan & Agol 2011).

The donors of period bouncers in accreting white dwarfs lie in an interesting corner of the parameter space of sub-stellar and planetary objects, where its internal flux and the external irradiation flux they are subjected to (from the hotter WD) are both comparable. Future observation of candidate period bouncers will provide access to an unexplored irradiation regime and contribute with measurements of atmospheric parameters.

5.2.1 Future work

Observational constraints on atmospheric parameters such as A_B and ϵ, can allow us to quantitatively test irradiated models of atmospheres in this regime. Unfortunately, as stated in the previous section, systems with sub-stellar donors are difficult to find and even more so to characterise. Few studies have systematically focused on the NIR as a way to retrieve information on the temperature of the donor (e.g. Ishioka et al. 2007). Nonetheless, there are a few systems which are bright and are suited for this kind of detailed analysis.

A natural candidate, is the eclipsing system SDSS J1035+0551 (Littlefair et al. 2006). As with SDSS J1433+1011, this short orbital period ($P_{orb} \simeq 82$ min) and WD-dominated system, most likely harbours a sub-stellar donor. Littlefair et al. (2006) and Savoury et al. (2011) estimated a mass of $M_2 = 0.0475 \pm 0.0012$ $M_\odot$, well below the hydrogen burning limit. This system might be the first true period bouncer to be directly detected.

There are two bright sources ($V \sim 15$) which I believe are perfect candidates (and overdue) for a detailed analysis, similar to that presented in Chapter 2. First, is the prototype for short-period CVs, WZ Sge[1]. The donor is likely a sub-stellar object (Steeghs et al. 2001) and recent $K-$band NIR observations, have determined a SpT=L1 (Harrison 2016). The second object, is another example of a bright system at $P_{orb} = 103$ min, GD 552. This system is most likely a period bouncer with a brown dwarf donor ($M_2 < 0.08$ $M_\odot$; Unda-Sanzana et al. 2008). Furthermore, at this orbital period, it could be the oldest CV we know of, with an estimated age of 7 Gyr. Confirming the sub-stellar nature of GD 552, can allow us to test the survival of CVs in the latter stages of their evolution.

5.3 The accreting state of a tMSP

In Chapter 4, I presented the first Hubble Space Telescope ultra-violet spectroscopic observations of the transitional millisecond pulsar, PSR J1023+0038. The FUV and NUV spectra revealed complex and rich features with broad emission lines from different ionised species. In particular, I observed FeII usually associated with outflows in quasars. The light curves revealed correlations between emission lines and continuum. In addition, the lack of lag between these light curves might indicate a common origin. This is further supported by the presence of a sudden flare lasting a full orbit. The increased but preferable in certain ionisation species, allowing to constrain the density of the outflow. I combined the average UV spectra with a quasi-simultaneous optical and NIR spectrum in order to retrieve information on the different components of the SED. The fit provided an estimate to the accretion disc inner radius to be $R_{in} = 8.552 \pm 0.001 \times 10^8$

[1]Previous observations with Keck have been unable to observe the donor (Howell et al. 2004).

cm ($\sim 100 r_{lc}$). This direct measurement of the truncation radius contrasts with the different models for the accreting state of PSR J1023+0038, where the disc is required to reach the NS magnetosphere.

Recently, it has been suggested that there are weakly-accreting X-ray binaries with luminosities ~ 100 lower than most LMXBs (Heinke et al. 2015). These luminosities ($L_X \sim 10^{33} - 10^{34}$ erg s^{-1}) are very similar to tMSPs which imply low mass transfer rates. Optical follow-up has shown that even at very low mass transfer rates, material can reach the NS surface and possibly form a truncated disc in the outer edges of the compact object, observed as prominent Hα in emission (e.g. 1RXH J173523.7 − 354013, Degenaar et al. 2010). It is possible that many of these weakly-accreting X-ray binaries might transition to a radio pulsar state when accretion fully stops or drops below $\sim 10^{33}$ erg s^{-1} (Heinke et al. 2015).

The spectroscopic and photometric characteristics of the UV wavelength region in PSR J1023+0038, are remarkably similar to the magnetic WD system, AE Aqr. In particular, these features resemble the outflow signatures from the propeller regime in AE Aqr, a model suggested as well for PSR J1023+0038. However, if there is a substantial outflow in the system, it must be carrying a very small fraction of the total energy in direct contrast to AE Aqr. If a propeller is active in this system, one way to understand and predict its behaviour is by studying analogue systems. In this category, AE Aqr and the recently discovered AR Sco (Marsh et al. 2016) can provide invaluable insight since they are brighter and more easily observable sources than most tMSPs.

5.3.1 Future work

The possibility of obtaining detailed UV-studies of these peculiar systems is unfortunately tied to the instrumentation available. The limited life-span of HST, with no clear successor on the horizon, should drive great urgency to carry out such studies. With only a handful of transitional candidates, it is imperative that we investigate and build up a good sample of UV-spectra of these systems. In particular, time-resolved spectroscopy can allow us to characterise the outflow and test theoretical models (such as the propeller scenario). Added to this, such observations can, in fact, be extended to other weakly-accreting LMXBs in quiescence where a truncated disc is suspected to remain after an outburst (Hynes & Jones 2009). Two other candidates that require UV and optical follow-up are:

1. XSS J12270-4859 has been visible as a millisecond radio pulsar since late 2012 (i.e., displaying radio pulsations, faint X-ray emission at $\sim 10^{32}$ erg s^{-1} and no optical signs of an accretion disc Casares et al. 2014; Bassa et al. 2014; Roy et al. 2014). This period of quiescence has allowed the donor to be observed, revealing a G/K-type companion star. Prior to this, between 2005-2012, it had been observed

in a quiescent LMXB state (e.g. Pretorius 2009; Hill et al. 2011; de Martino et al. 2013).

2. 1RXS J154439.4112820 (1RXS J1544 hereafter) is a new candidate for a transitional millisecond pulsar binary, recently associated with Fermi-LAT source 3FGL J1544.61125 (Bogdanov & Halpern 2015). The object exhibits X-ray and optical variability remarkably similar to the other three confirmed tMSPs. Therefore, the system is believed to be in an accreting state, and may switch off at any time to re-appear as a millisecond radio pulsar.

Appendix A

Brown Dwarf Sequence

I present the brown dwarf sequence used to interpolate the atmosphere grid in ICARUS. We used the template spectra from the IRTF spectral library[1] and calibrated the sequence with the bolometric luminosities and distances taken from Cushing et al. (2005).

TABLE A.1: Brown Dwarf Template Grid used in ICARUS

SpT	Name	d pc	R $R_\odot$	$\log_{10}(L_{bol})$ $L_\odot$	$T_{\rm eff}$[a] K	T_{eff}[b] K	M_K
M6 V	Gl 406	2.39	0.13	-2.98	2792	2776	9.241
M8	VB 10 (LHS 474)	6.086	0.11	-3.34	2493	2546	10.00
M9.5 V	BRI B0021-0214	11.54	0.10	-3.51	2342	2332	10.37
L0	LHS 2924	11.11	0.10	-3.62	2219	2258	10.48
L1	2MASS J14392836+1929149	14.36	0.10	-3.72	2129	2112	10.71
L3.5	2MASS J00361617+1821104	8.756	0.09	-3.97	1895	1778	11.35
L4.5	2MASS J22244381-0158521	11.4	0.09	-4.20	1665	1666	11.65
L7.5	2MASS J08251968+2115521	10.66	0.10	-4.58	1269	1424	12.75
L8	DENIS-P 025503.3-470049.0	4.96[c]	0.11	-4.62	1213	1396	12.96

[a] Bolometric measurements by Cushing et al. (2005)

[b] Calibration by Stephens et al. (2009). $T_{\rm eff} = 2265.9+347.82X-60.558*X^2+3.151X^3-0.060481X^4+0.00024506X^5$, where where $6 \leq X \leq 28$ relates to spectral type as M6 $\leq$ SpT $\leq$ T8

[c] Parallax from Kirkpatrick et al. (2008).

To obtain the new water band index, we made use of all the brown dwarf templates available. The best fit with its associated errors, is:

$$X = -26.5(\pm 0.5) H_2O^a + 19.5(\pm 0.3) \quad \text{(A.1)}$$

[1] http://irtfweb.ifa.hawaii.edu/~spex/IRTF_Spectral_Library

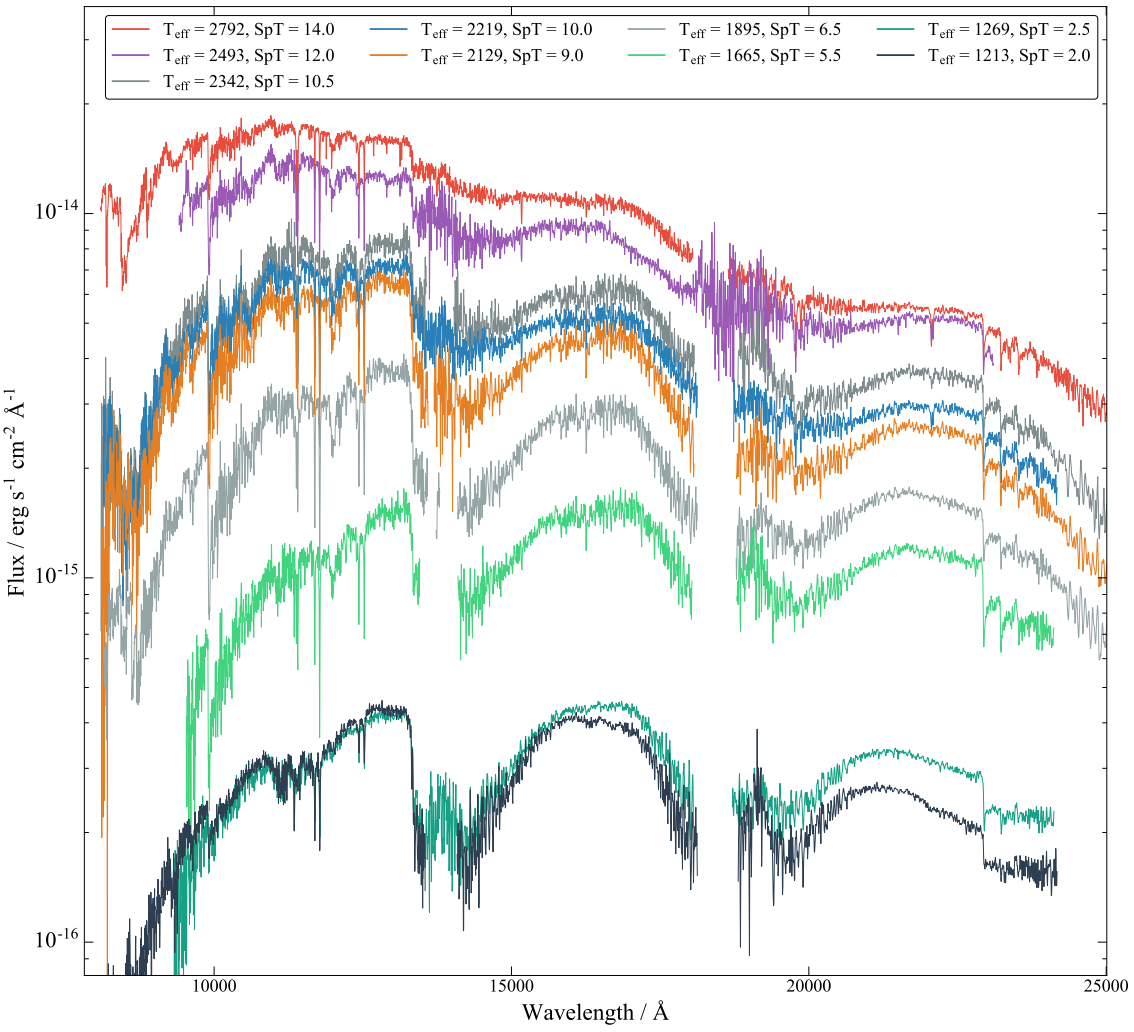

FIGURE A.1: Brown dwarf sequence spectra. All spectra have been renormalised to a fixed radius and a distance.

where $-9 \leq X \leq 19$ relates to spectral type as M1 $\leq$ SpT $\leq$ T9.

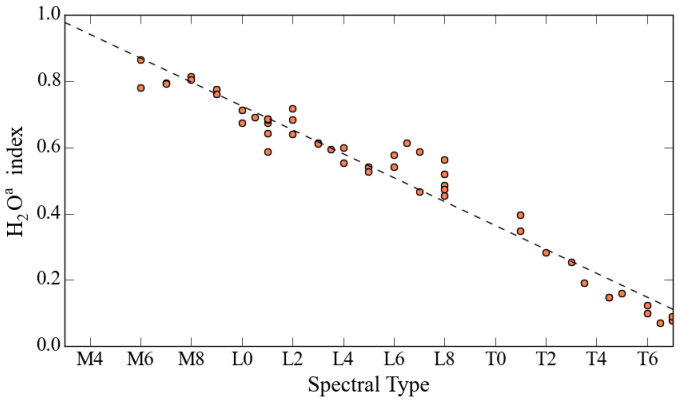

FIGURE A.2: Water band index. The brown dwarf measurements are shown as well as the best fit.

Appendix B

Light Curve Modelling

In order to retrieve the information from the observed spectrum and light curves, it is necessary to recreate a model that includes different physical processes. I made use of the code ICARUS to model and retrieve physical parameters from the light curve. This software allows us to simulate photometry and spectroscopy of binary systems, by providing an external atmosphere grid. For a full description of the code I refer to the original instrument paper of Breton et al. (2012). However, I will summarise the method in this section.

In the case of an overflowing donor star, the atmosphere will expand up to the Roche-lobe surface (calculated by Equation 1.1) before overflowing the L_1 point. As a result, the donor geometry will deviate significantly from a sphere. Therefore, it is necessary to account for the geometrical distortions of the star. The model is created by segmenting the Roche-potential surface of the donor in j elements as shown in Figure B.1. This allows us to follow the local conditions on the surface and eventually calculate the integrated effect. For fully convective stars the outgoing flux is given by the local surface

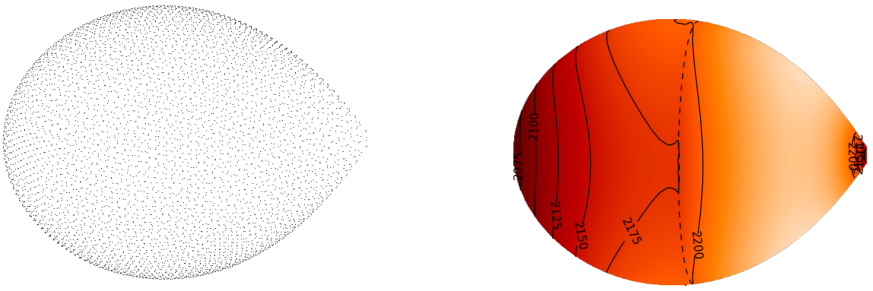

FIGURE B.1: Discrete segmentation of the surface of the donor (*left*) and temperature iso-contours of an irradiated donor (*right*), after implementation of gravity and limb darkening. For a full animation use Adobe Acrobat Reader[2]

gravity, g_j, at each specific point in the star (von Zeipel 1924; White et al. 2012). This

gravity darkening will have an effect on the local internal temperature, $T_{\mathrm{int},j}$, which can be parametrised as:

$$\frac{T_{\mathrm{int},j}}{T_{\mathrm{pole}}} = \left[\frac{g_{\mathrm{int},j}}{g_{\mathrm{pole}}}\right]^{\beta} \tag{B.1}$$

where $\beta = 0.8$ (Lucy 1967). In rotating stars, the higher flux is located at the poles (since g is higher). The donors in most accreting systems are Roche-lobe filling (or close to it), therefore gravity darkening can produce dramatic temperature gradients at critical points such as L_1 (seen at lower temperatures). Consequently, the internal flux, $F_{\mathrm{int},j}$, radiated by every surface element is given by:

$$F_{\mathrm{int},j} = A_j \sigma T^4_{\mathrm{int},j}, \tag{B.2}$$

where A_j is the area of the surface element, and σ is the Stefan-Boltzmann constant.

In many systems, the donor is being engulfed in an external irradiation field from a nearby source e.g. a compact object. Therefore, the total outgoing flux, F_{tot}, from every surface element j on the heated side of the donor is defined by the sum of the internal flux, F_{int} and the absorbed irradiation flux, F_{irr}:

$$F_{\mathrm{tot},j} = F_{\mathrm{int},j} + F_{\mathrm{irr},j}. \tag{B.3}$$

In the absence of any redistribution of heat across the interior of the star, the local effective temperature for fully convective stars is then defined as (Ruciński 1969; Beech 1985) :

$$T_{\mathrm{tot},j} = \left[T^4_{\mathrm{int},j} + T_{\mathrm{irr},j}\frac{\cos(\alpha)}{r^2}\right]^{1/4} \tag{B.4}$$

where α and r are the projected angle and distance of the surface element to the irradiating source, respectively.

Once the properties of every surface element such as $T(x, y, z)$ and $g(x, y, z)$ are determined, it is possible to produce the spectrum by integrating the specific intensities over the surface at each orbital phase. We have used pre-computed theoretical atmosphere grids (e.g. CIFIST Baraffe et al. 2015) or those based on empirical brown dwarf templates (Appendix A). The physical flux, F_λ, calculated in the output spectrum is a function of the line of sight since the light emitted in each surface element will be affected by limb darkening:

$$F_\lambda = 2\pi \int_0^1 I_\lambda(\mu)\mu \mathrm{d}\mu \tag{B.5}$$

where $I_\lambda(\mu)$ is the specific intensity, μ is the cosine of the angle between the surface element and the line of sight. Limb darkening is defined as the ratio of intensity from the centre towards the edge:

$$f_\lambda(\mu) = \frac{I_\lambda(\mu)}{I_\lambda(1)} \tag{B.6}$$

However, since we used a set of empirical templates, it was necessary to recompute the specific intensities at each μ. Thus, we must assume a limb darkening law to inverse the process. This limb darkening law is in fact wavelength dependant, however, there is no study of its impact at NIR wavelengths except for broad-band filters (Claret et al. 2012). For simplicity, I assumed its validity throughout the associated broad-band filter region. Therefore, it was possible to compute a grid of specific intensities by combining Equations B.5 and B.6:

$$\hat{I}_\lambda(\mu) = \frac{F_\lambda f_\lambda(\mu)}{2\pi \int_0^1 f_\lambda(\mu)\mu \mathrm{d}\mu} \tag{B.7}$$

where $\hat{I}_\lambda(\mu)$ is the retrieved specific intensity for a given limb darkening law.

In order to compare with other studies, mainly in the planetary community, it is convenient to define the average temperatures of the day- and night-side of the donor. The average day-side temperature is obtained by integrating over all the surface elements that experience irradiation:

$$\langle T_{\mathrm{day}} \rangle = \left(\frac{1}{\sigma} \frac{\sum_{j,\mathrm{day}} F_{\mathrm{tot}_j}}{\sum_{j,\mathrm{day}} A_j} \right)^{1/4} . \tag{B.8}$$

Conversely, the night-side temperature is defined as:

$$\langle T_{\mathrm{night}} \rangle = \left(\frac{1}{\sigma} \frac{\sum_{j,\mathrm{night}} F_{\mathrm{int},j}}{\sum_{j,\mathrm{night}} A_j} \right)^{1/4} . \tag{B.9}$$

Appendix C

SDSS White Dwarf selection

I used the following SQL code used through the Catalog Archive Server (CAS)[1] to retrieve the photometric data of the WD candidates. I followed the colour-colour cuts for WD suggested by Girven et al. (2011) and the best selection criteria for objects in the co-add catalogue of Stripe 82 (Annis et al. 2014).

```
SELECT objid,ra,dec,u,g,r,i,z,run,rerun, camcol, field,primtarget, psfMag_u, psfMag_g, psfMag_r, psfMag_i,
     psfMag_z, flags, psfmagerr_u, psfmagerr_g, psfmagerr_r, psfmagerr_i, psfmagerr_z
FROM PhotoObj
WHERE (run = 106 OR run = 206)
AND (u-g)>=-20.653*power(g-r,5) +10.816*power(g-r,4) +15.718*power(g-r,3)
     -1.294*power(g-r,2)-0.084*(g-r)+0.300
AND (u-g)<=-24.384*power(g-r,5) -19.000*power(g-r,4) +3.497*power(g-r,3)
     +1.193*power(g-r,2)+0.083*(g-r)+0.610
AND (g-r)<=-0.693*power(r-i,2) +0.947*(r-i) +0.192
AND (g-r)>=-1.320*power(r-i,3) +2.173*power(r-i,2) +2.452*(r-i)-0.070
AND (r-i)>=-0.560
AND (r-i)<=0.176*(i-z)+0.127
AND (r-i)<=-0.754*(i-z)+0.110
AND ((flags & 0x10000000) != 0)
AND ((flags & 0x8100000c00a4) = 0)
AND (((flags & 0x400000000000) = 0)
OR (psfmagerr_r <= 0.2 AND psfmagerr_i<=0.2 AND psfmagerr_g<=0.2)) AND (((flags&0x100000000000) = 0) OR
     (flags & 0x1000) = 0)
AND type = 6
AND mode = 1
AND g<21
ORDER BY g
```

[1] http://cas.sdss.org/stripe82

Appendix D

STIS timing code

The code described below was used to perform the time analysis in Chapter 4. The main purpose is to perform a quick wavelength solution to individual TIME-TAG events in order to perform time-domain analysis. This code makes use of the bets calibration files associated to each observation. I carry on a description of the code as well as a test case of the Crab pulsar (Gull et al. 1997).

Every TIME-TAG event provides a physical location on the MAMA detector onboard HST, stored in the **_tag** file. However, only a small portion of the detector is iluminated by the source, hence it is necessary to provide the location of the slit. This location is found in the **_x2d** file. This allows to trace and rectify the individual position of the TIME-TAG events to a linear configuration centred at the middle of the slit (the slit is positioned diagonally on the MAMA detector), as shown in the middle panel of Figure D.1. Afterwards, it is possible to assign the respective wavelength, λ, to individual events by solving the following equation:

$$s = A_0 + A_1 m\lambda + A_2(m\lambda)^2 + A_3 m + A_4\lambda + A_5 m^2\lambda + A_6 m\lambda^2 + A_7(m\lambda)^3 \qquad \text{(D.1)}$$

where s is pixel in the the AXIS1 detector, m is the spectral order and A_i are the dispersion coefficients. I used the corresponding reference file **_x2d** file to retrieve the best values for A_i and m. Finally, the code returns a new fits file, containing all the information of the original **_tag** file with an added wavelength column, as shown in the middle panel of Figure D.1. I used a well-study case, the Crab pulsar (Gull et al. 1997) to test the code and the end products. In Figure D.2, I show the corrected and calibrated TIME-TAG spectrum. I extracted only the events around the slit (50 pixels) and binned the lightcurve in 1 s bins. Then, I performed a FFT to search for the pulsations, shown in the PSD (bottom panel of Figure D.2). The peaks found are the fundamental frequency ($f_0 = 29.84819$ Hz) and its harmonics. Finally, I calculated the phase of individual events and binned the lightcurve in 100 spin bins, revealing the characteristic double pulse of the Crab, shown in Figure D.3.

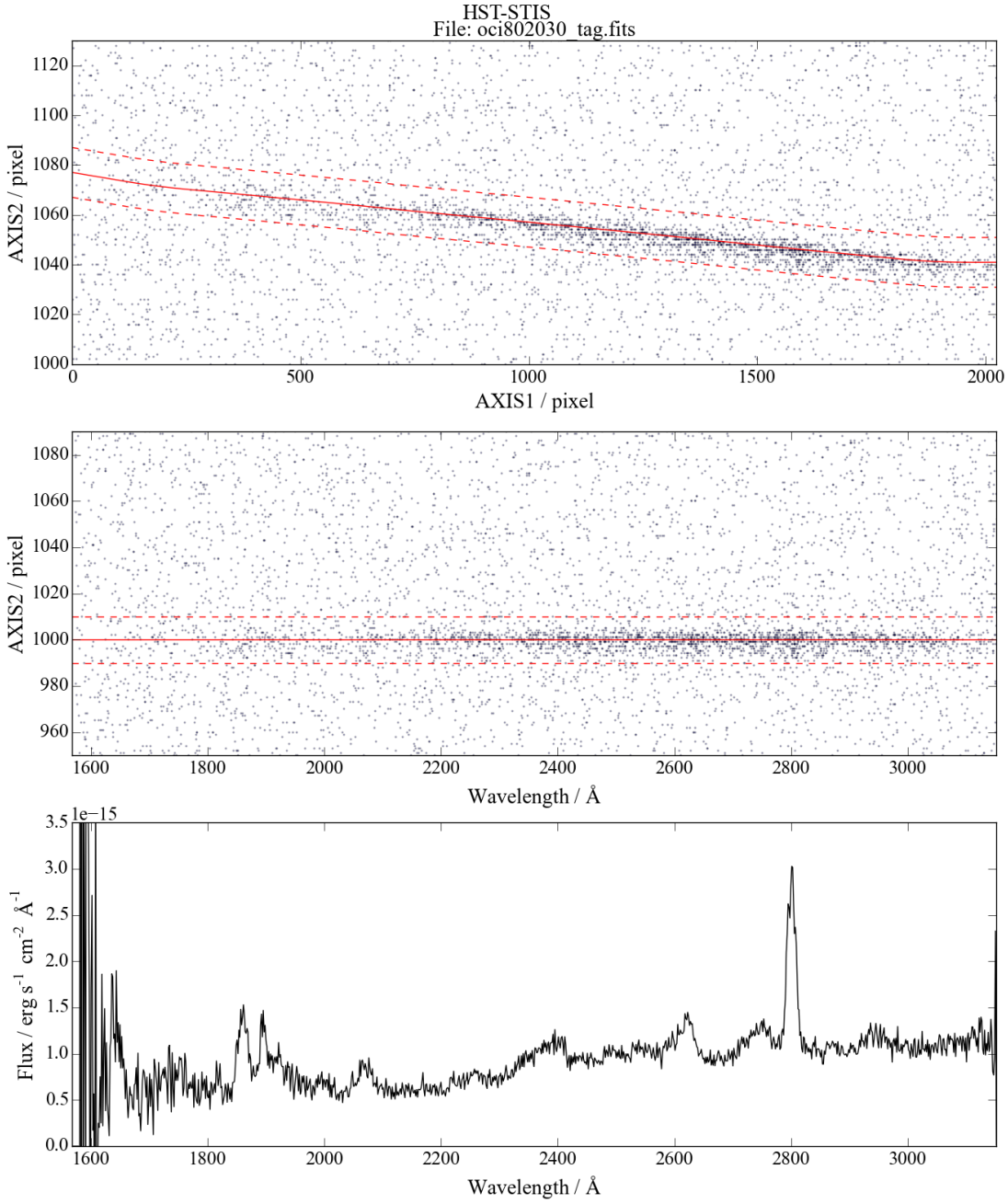

FIGURE D.1: Example extraction of STIS lightcurve of MgI 2810 Å. *Top* : Localisation of the slit in the image in pixel coordinates. *Middle* : Corrected image after wavelength assignment. *Bottom* : 1D spectra of the target, used as a reference.

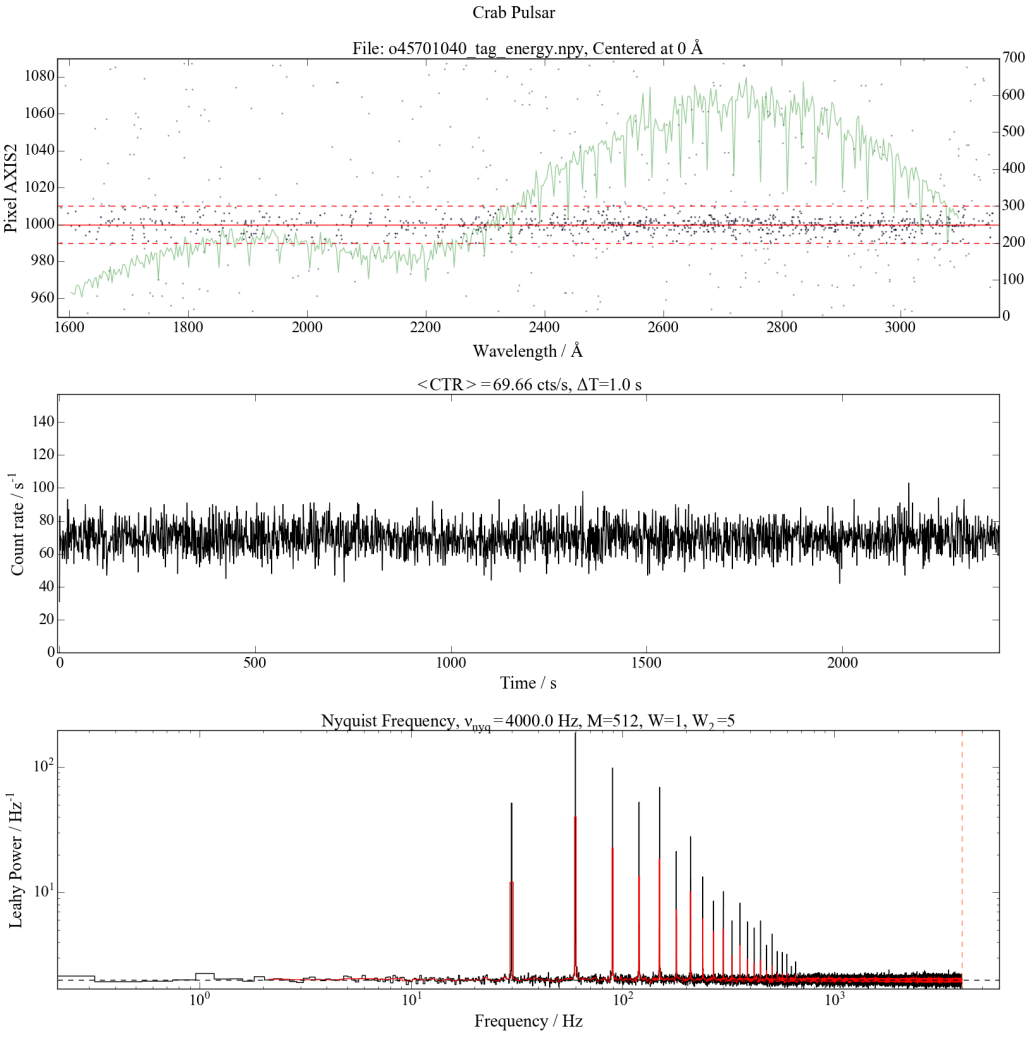

FIGURE D.2: Example extraction of STIS lightcurve of the full slit for the Crab Pulsar. *Top* : Localisation of the slit in the image in pixel coordinates. *Middle* : 1 s binned lightcurve. *Bottom* : Power spectrum distribution.

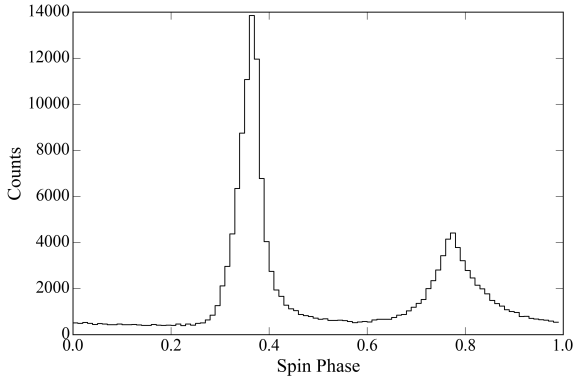

FIGURE D.3: Folded STIS lightcurve of the Crab Pulsar on the spin period.

Bibliography

Abada-Simon, M., Lecacheux, A., Bastian, T. S., Bookbinder, J. A., & Dulk, G. A. 1993, ApJ, 406, 692

Abdo, A. A., Ajello, M., Allafort, A., et al. 2013, ApJS, 208, 17

Abramowicz, M. A., & Fragile, P. C. 2013, Living Reviews in Relativity, 16, arXiv:1104.5499 [astro-ph.HE]

Allard, F., Homeier, D., & Freytag, B. 2012, Royal Society of London Philosophical Transactions Series A, 370, 2765

Allen, C. W. 1976, Astrophysical Quantities

Alpar, M. A., Cheng, A. F., Ruderman, M. A., & Shaham, J. 1982, Nature, 300, 728

Andrae, R., Schulze-Hartung, T., & Melchior, P. 2010, ArXiv e-prints, arXiv:1012.3754 [astro-ph.IM]

Annis, J., Soares-Santos, M., Strauss, M. A., et al. 2014, ApJ, 794, 120

Archibald, A. M., Kaspi, V. M., Hessels, J. W. T., et al. 2013, ArXiv e-prints, arXiv:1311.5161 [astro-ph.HE]

Archibald, A. M., Stairs, I. H., Ransom, S. M., et al. 2009, Science, 324, 1411

Archibald, A. M., Bogdanov, S., Patruno, A., et al. 2015, ApJ, 807, 62

Arras, P., & Bildsten, L. 2006, ApJ, 650, 394

Aviles, A., Zharikov, S., Tovmassian, G., et al. 2010, ApJ, 711, 389

Baade, W., & Zwicky, F. 1934, Physical Review, 46, 76

Bachetti, M., Harrison, F. A., Walton, D. J., et al. 2014, Nature, 514, 202

Baglio, M. C., D'Avanzo, P., Campana, S., et al. 2016, A&A, 591, A101

Baraffe, I., Homeier, D., Allard, F., & Chabrier, G. 2015, A&A, 577, A42

Barman, T. S., Hauschildt, P. H., & Allard, F. 2004, ApJ, 614, 338

Barnes, T. G., & Evans, D. S. 1976, MNRAS, 174, 489

Bassa, C. G., Patruno, A., Hessels, J. W. T., et al. 2014, MNRAS, 441, 1825

Beech, M. 1985, Ap&SS, 117, 69

Bell, M. E., Murphy, T., Kaplan, D. L., et al. 2014, MNRAS, 438, 352

Belloni, T., Psaltis, D., & van der Klis, M. 2002, ApJ, 572, 392

Benitez, N., Dupke, R., Moles, M., et al. 2014, ArXiv e-prints, arXiv:1403.5237 [astro-ph.CO]

Benvenuto, O. G., De Vito, M. A., & Horvath, J. E. 2014, ApJ, 786, L7

—. 2015, MNRAS, 449, 4184

Beuermann, K. 2006, A&A, 460, 783

Bhattacharya, D., & van den Heuvel, E. P. J. 1991, Phys. Rep., 203, 1

Bildsten, L. 1998, ApJ, 501, L89

Boffin, H. M. J., Steeghs, D., & Cuypers, J., eds. 2001, Lecture Notes in Physics, Berlin Springer Verlag, Vol. 573, Astrotomography: Indirect Imaging Methods in Observational Astronomy, ed. H. M. J. Boffin, D. Steeghs, & J. Cuypers (Springer)

Bogdanov, S., & Halpern, J. P. 2015, ApJ, 803, L27

Bogdanov, S., Archibald, A. M., Bassa, C., et al. 2015, ApJ, 806, 148

Bond, H. E., White, R. L., Becker, R. H., & O'Brien, M. S. 2002, PASP, 114, 1359

Breedt, E., Gänsicke, B. T., Drake, A. J., et al. 2014, MNRAS, 443, 3174

Breton, R. P., Rappaport, S. A., van Kerkwijk, M. H., & Carter, J. A. 2012, ApJ, 748, 115

Burgasser, A. J., Reid, I. N., Siegler, N., et al. 2007, Protostars and Planets V, 427

Camenzind, M. 2007, Compact objects in astrophysics : white dwarfs, neutron stars, and black holes

Camilo, F., Reynolds, J. E., Ransom, S. M., et al. 2016, ApJ, 820, 6

Campana, S., Coti Zelati, F., Papitto, A., et al. 2016, A&A, 594, A31

Casares, J., de Martino, D., Mason, E., et al. 2014, The Astronomer's Telegram, 5747

Casewell, S. L., Burleigh, M. R., Lawrie, K. A., et al. 2013, Mem. Soc. Astron. Italiana, 84, 1022

Castelli, F., & Kurucz, R. L. 2004, ArXiv Astrophysics e-prints, astro-ph/0405087

Chabrier, G., & Baraffe, I. 1997, A&A, 327, 1039

Chabrier, G., Baraffe, I., Leconte, J., Gallardo, J., & Barman, T. 2009, in American Institute of Physics Conference Series, Vol. 1094, 15th Cambridge Workshop on Cool Stars, Stellar Systems, and the Sun, ed. E. Stempels, 102

Chakrabarty, D., Morgan, E. H., Muno, M. P., et al. 2003, Nature, 424, 42

Chanan, G. A., Middleditch, J., & Nelson, J. E. 1976, ApJ, 208, 512

Charles, P. A., & Coe, M. J. 2006, Optical, ultraviolet and infrared observations of X-ray binaries, ed. W. H. G. Lewin & M. van der Klis, 215

Chen, H.-L., Chen, X., Tauris, T. M., & Han, Z. 2013, ApJ, 775, 27

Chen, J., & Kipping, D. M. 2016, ArXiv e-prints, arXiv:1603.08614 [astro-ph.EP]

Cieslinski, D., Diaz, M. P., Mennickent, R. E., & Pietrzyński, G. 2003, PASP, 115, 193

Claret, A., Hauschildt, P. H., & Witte, S. 2012, A&A, 546, A14

Coppejans, D. L., Körding, E. G., Knigge, C., et al. 2016, MNRAS, 456, 4441

Coti Zelati, F., Baglio, M. C., Campana, S., et al. 2014, MNRAS, 444, 1783

Cowan, N. B., & Agol, E. 2011, ApJ, 729, 54

Cushing, M. C., Rayner, J. T., & Vacca, W. D. 2005, ApJ, 623, 1115

de Kool, M. 1992, A&A, 261, 188

de Martino, D., Falanga, M., Bonnet-Bidaud, J.-M., et al. 2010, A&A, 515, A25

de Martino, D., Belloni, T., Falanga, M., et al. 2013, A&A, 550, A89

Degenaar, N., Jonker, P. G., Torres, M. A. P., et al. 2010, MNRAS, 404, 1591

Del Zanna, G., Dere, K. P., Young, P. R., Landi, E., & Mason, H. E. 2015, A&A, 582, A56

Deller, A. T., Archibald, A. M., Brisken, W. F., et al. 2012, ApJ, 756, L25

Deller, A. T., Moldon, J., Miller-Jones, J. C. A., et al. 2015, ApJ, 809, 13

Dhillon, V. S., Marsh, T. R., Stevenson, M. J., et al. 2007, MNRAS, 378, 825

Douglas, S. T., Agüeros, M. A., Covey, K. R., et al. 2014, ApJ, 795, 161

Drake, A. J., Djorgovski, S. G., Mahabal, A., et al. 2009, ApJ, 696, 870

Drake, A. J., Beshore, E., Catelan, M., et al. 2010, ArXiv e-prints, arXiv:1009.3048 [astro-ph.EP]

Dupuy, T. J., & Liu, M. C. 2012, ApJS, 201, 19

Duquennoy, A., & Mayor, M. 1991, A&A, 248, 485

Echevarria, J. 1983, Rev. Mex. Astron. Astrofis., 8, 109

Eddington, A. S. 1926, The Internal Constitution of the Stars

Eggleton, P. P. 1983, ApJ, 268, 368

Eracleous, M., & Horne, K. 1996, ApJ, 471, 427

Eracleous, M., Horne, K., Robinson, E. L., et al. 1994, ApJ, 433, 313

Ertan, U. 2015, ArXiv e-prints, arXiv:1504.03996 [astro-ph.HE]

Evans, P. A., Beardmore, A. P., Page, K. L., et al. 2007, A&A, 469, 379

—. 2009, MNRAS, 397, 1177

Faedi, F., West, R. G., Burleigh, M. R., Goad, M. R., & Hebb, L. 2011, MNRAS, 410, 899

Firth, R. E., Sullivan, M., Gal-Yam, A., et al. 2015, MNRAS, 446, 3895

Fitzpatrick, E. L. 1999, PASP, 111, 63

Fontaine, G., Brassard, P., & Bergeron, P. 2001, PASP, 113, 409

Foreman-Mackey, D., Hogg, D. W., Lang, D., & Goodman, J. 2013, PASP, 125, 306

Frank, J., King, A., & Raine, D. J. 2002, Accretion Power in Astrophysics: Third Edition, 398

Friend, M. T., Smith, R. C., Martin, J. S., & Jones, D. H. P. 1988, MNRAS, 233, 451

Fruchter, A. S., Gunn, J. E., Lauer, T. R., & Dressler, A. 1988a, Nature, 334, 686

Fruchter, A. S., Stinebring, D. R., & Taylor, J. H. 1988b, Nature, 333, 237

Gänsicke, B. T., Dillon, M., Southworth, J., et al. 2009, MNRAS, 397, 2170

Gayley, K. G., & Owocki, S. P. 1994, ApJ, 434, 684

Ghosh, P., & Lamb, F. K. 1979, ApJ, 232, 259

Giacconi, R., Gursky, H., Paolini, F. R., & Rossi, B. B. 1962, Physical Review Letters, 9, 439

Girven, J., Gänsicke, B. T., Steeghs, D., & Koester, D. 2011, MNRAS, 417, 1210

Goliasch, J., & Nelson, L. 2015, ApJ, 809, 80

González Martínez-País, I., Shahbaz, T., & Casares Velázquez, J. 2014, Accretion Processes in Astrophysics

Gray, D. F. 2008, The Observation and Analysis of Stellar Photospheres

Grether, D., & Lineweaver, C. H. 2006, ApJ, 640, 1051

Gull, T. R., Lindler, D. J., Crenshaw, D. M., et al. 1997, ArXiv Astrophysics e-prints, astro-ph/9712355

Hachisu, I., & Kato, M. 2006, ApJS, 167, 59

Hakala, P., Ramsay, G., Barclay, T., & Charles, P. 2015, MNRAS, 453, L6

Hallinan, G., Littlefair, S. P., Cotter, G., et al. 2015, Nature, 523, 568

Halpern, J. P., Gaidos, E., Sheffield, A., Price-Whelan, A. M., & Bogdanov, S. 2013, The Astronomer's Telegram, 5514, 1

Harrison, T. E. 2016, ApJ, 816, 4

Heinke, C. O., Bahramian, A., Degenaar, N., & Wijnands, R. 2015, MNRAS, 447, 3034

Hellier, C. 2001, Cataclysmic Variable Stars, ed. Hellier, C.

Hernández Santisteban, J. V., Knigge, C., Littlefair, S. P., et al. 2016, Nature, 533, 366

Herschel, W. 1803, Philosophical Transactions of the Royal Society of London Series I, 93, 339

Hertz, P., Bailyn, C. D., Grindlay, J. E., et al. 1990, ApJ, 364, 251

Hessels, J. W. T., Ransom, S. M., Stairs, I. H., et al. 2006, Science, 311, 1901

Hewish, A., Bell, S. J., Pilkington, J. D. H., Scott, P. F., & Collins, R. A. 1968, Nature, 217, 709

Hill, A. B., Szostek, A., Corbel, S., et al. 2011, MNRAS, 415, 235

Hilton, E. J. 2011, PhD thesis, University of Washington

Holberg, J. B., & Bergeron, P. 2006, AJ, 132, 1221

Horne, K. 1985, MNRAS, 213, 129

Horne, K., Gomer, R. H., & Lanning, H. H. 1982, ApJ, 252, 681

Horne, K., Wade, R. A., & Szkody, P. 1986, MNRAS, 219, 791

Howell, S. B., Harrison, T. E., & Szkody, P. 2004, ApJ, 602, L49

Howell, S. B., Rappaport, S., & Politano, M. 1997, MNRAS, 287, 929

Howell, S. B., Sobeck, C., Haas, M., et al. 2014, PASP, 126, 398

Hubeny, I., Burrows, A., & Sudarsky, D. 2003, ApJ, 594, 1011

Hubeny, I., & Lanz, T. 1995, ApJ, 439, 875

Hunter, J. D. 2007, Computing In Science & Engineering, 9, 90

Hynes, R. I., Charles, P. A., Casares, J., et al. 2003, MNRAS, 340, 447

Hynes, R. I., & Jones, E. D. 2009, ApJ, 697, L14

Hynes, R. I., Schaefer, B. E., Baum, Z. A., et al. 2016, MNRAS, 459, 3596

Illarionov, A. F., & Sunyaev, R. A. 1975, A&A, 39, 185

Ishioka, R., Sekiguchi, K., & Maehara, H. 2007, PASJ, 59, 929

Ivanova, N., Justham, S., Chen, X., et al. 2013, A&ARv, 21, 59

Ivezic, Z., Tyson, J. A., Abel, B., et al. 2008, ArXiv e-prints, arXiv:0805.2366

Jameson, R. F., King, A. R., & Sherrington, M. R. 1980, MNRAS, 191, 559

Janka, H.-T., Kifonidis, K., & Rampp, M. 2001, in Lecture Notes in Physics, Berlin Springer Verlag, Vol. 578, Physics of Neutron Star Interiors, ed. D. Blaschke, N. K. Glendenning, & A. Sedrakian, 363

Jia, K., & Li, X.-D. 2015, ApJ, 814, 74

Jumper, P. H., & Fisher, R. T. 2013, ApJ, 769, 9

Kahabka, P. 2002, ArXiv Astrophysics e-prints, astro-ph/0212037

Kato, T., & Osaki, Y. 2013, PASJ, 65, arXiv:1307.5588 [astro-ph.SR]

Kausch, W., Noll, S., Smette, A., et al. 2014, in Astronomical Society of the Pacific Conference Series, Vol. 485, Astronomical Society of the Pacific Conference Series, ed. N. Manset & P. Forshay, 403

Kawaler, S. D. 1988, ApJ, 333, 236

Kepler, S. O., Pelisoli, I., Koester, D., et al. 2015, MNRAS, 446, 4078

King, A. R. 1988, QJRAS, 29, 1

King, A. R., Beer, M. E., Rolfe, D. J., Schenker, K., & Skipp, J. M. 2005, MNRAS, 358, 1501

King, A. R., Davies, M. B., & Beer, M. E. 2003, MNRAS, 345, 678

King, A. R., & Kolb, U. 1995, ApJ, 439, 330

Kirkpatrick, J. D., Reid, I. N., Liebert, J., et al. 1999, ApJ, 519, 802

Kirkpatrick, J. D., Cruz, K. L., Barman, T. S., et al. 2008, ApJ, 689, 1295

Kleinman, S. J., Kepler, S. O., Koester, D., et al. 2013, ApJS, 204, 5

Knigge, C. 2006, MNRAS, 373, 484

Knigge, C. 2011a, in Astronomical Society of the Pacific Conference Series, Vol. 447, Evolution of Compact Binaries, ed. L. Schmidtobreick, M. R. Schreiber, & C. Tappert, 3

—. 2011b, ArXiv e-prints, arXiv:1101.1538 [astro-ph.SR]

Knigge, C., Baraffe, I., & Patterson, J. 2011, ApJS, 194, 28

Kolb, U. 1993, A&A, 271, 149

Kolb, U., & Baraffe, I. 1999, MNRAS, 309, 1034

Kolb, U., & de Kool, M. 1993, A&A, 279, L5

Kong, A. K. H. 2013, The Astronomer's Telegram, 5515, 1

Kopal, Z. 1978, Astrophysics and Space Science Library, Vol. 68, Dynamics of Close Binary Sistems (Dordrecht, Netherlands: D. Reidel Publishing Company)

LaMassa, S. M., Urry, C. M., Cappelluti, N., et al. 2016, ApJ, 817, 172

Lamb, F. K., & Ghosh, P. 1991, Interaction of accretion disks with magnetospheres, ed. J. van Paradijs, M. van der Klis, & A. Achterberg, 37

Landau, L. D., & Lifshitz, E. M. 1971, The classical theory of fields

Lasota, J.-P. 2001, New Astron. Rev., 45, 449

Law, N. M., Kulkarni, S. R., Dekany, R. G., et al. 2009, PASP, 121, 1395

Li, K. L., Kong, A. K. H., Takata, J., et al. 2014, ApJ, 797, 111

Linares, M. 2014, ApJ, 795, 72

Linares, M., Casares, J., Rodriguez-Gil, P., & Shahbaz, T. 2014a, The Astronomer's Telegram, 5868, 1

Linares, M., Bahramian, A., Heinke, C., et al. 2014b, MNRAS, 438, 251

Littlefair, S. P., Dhillon, V. S., Marsh, T. R., et al. 2008, MNRAS, 388, 1582

—. 2006, Science, 314, 1578

Littlefair, S. P., Savoury, C. D. J., Dhillon, V. S., et al. 2013, MNRAS, 431, 2820

Lorimer, D. R. 2008, Living Reviews in Relativity, 11, 8

Loyd, R. O. P., & France, K. 2014, ApJS, 211, 9

Lucy, L. B. 1967, Z. Astrophys., 65, 89

Manchester, R. N., Hobbs, G. B., Teoh, A., & Hobbs, M. 2005, AJ, 129, 1993

Marsh, T. R. 1988, MNRAS, 231, 1117

Marsh, T. R., & Horne, K. 1988, MNRAS, 235, 269

Marsh, T. R., Gänsicke, B. T., Hümmerich, S., et al. 2016, Nature, 537, 374

Martin, D. C., Fanson, J., Schiminovich, D., et al. 2005, ApJ, 619, L1

Matt, S. P., Brun, A. S., Baraffe, I., Bouvier, J., & Chabrier, G. 2015, ApJ, 799, L23

McAllister, M. J., Littlefair, S. P., Baraffe, I., et al. 2015, MNRAS, 451, 114

McClintock, J. E., & Remillard, R. A. 2000, ApJ, 531, 956

McConnell, O., Callanan, P. J., Kennedy, M., et al. 2015, MNRAS, 451, 3468

McLean, I. S., McGovern, M. R., Burgasser, A. J., et al. 2003, ApJ, 596, 561

McLean, I. S., Prato, L., McGovern, M. R., et al. 2007, ApJ, 658, 1217

Menou, K., Esin, A. A., Narayan, R., et al. 1999, ApJ, 520, 276

Modigliani, A., Goldoni, P., Royer, F., et al. 2010, in Society of Photo-Optical Instrumentation Engineers (SPIE) Conference Series, Vol. 7737, Society of Photo-Optical Instrumentation Engineers (SPIE) Conference Series

Mohanty, S., & Basri, G. 2003, ApJ, 583, 451

Muratov, A. L., & Gnedin, O. Y. 2010, ApJ, 718, 1266

Narayan, R., Garcia, M. R., & McClintock, J. E. 1997, ApJ, 478, L79

Nelemans, G., Siess, L., Repetto, S., Toonen, S., & Phinney, E. S. 2016, ApJ, 817, 69

Newsham, G., Starrfield, S., & Timmes, F. X. 2014, in Astronomical Society of the Pacific Conference Series, Vol. 490, Stellar Novae: Past and Future Decades, ed. P. A. Woudt & V. A. R. M. Ribeiro, 287

Nordhaus, J., & Spiegel, D. S. 2013, MNRAS, 432, 500

Osaki, Y. 1974, PASJ, 26, 429

Otulakowska-Hypka, M., Olech, A., & Patterson, J. 2016, ArXiv e-prints, arXiv:1605.02937 [astro-ph.SR]

Paczyński, B. 1967, Acta Astron., 17, 287

—. 1971, ARA&A, 9, 183

Paczynski, B. 1976, in IAU Symposium, Vol. 73, Structure and Evolution of Close Binary Systems, ed. P. Eggleton, S. Mitton, & J. Whelan, 75

Paczynski, B. 1977, ApJ, 216, 822

Pala, A. F., Gänsicke, B. T., Beuermann, K., et al. 2015, in Astronomical Society of the Pacific Conference Series, Vol. 493, 19th European Workshop on White Dwarfs, ed. P. Dufour, P. Bergeron, & G. Fontaine, 521

Papitto, A., Bozzo, E., Ferrigno, C., & Rea, N. 2013a, The Astronomer's Telegram, 5534, 1

Papitto, A., & Torres, D. F. 2015, ApJ, 807, 33

Papitto, A., Torres, D. F., & Li, J. 2014a, MNRAS, 438, 2105

Papitto, A., Torres, D. F., Rea, N., & Tauris, T. M. 2014b, A&A, 566, A64

Papitto, A., Ferrigno, C., Bozzo, E., et al. 2013b, Nature, 501, 517

Parsons, S. G., Gänsicke, B. T., Marsh, T. R., et al. 2013, MNRAS, 429, 256

Parsons, S. G., Agurto-Gangas, C., Gänsicke, B. T., et al. 2015, MNRAS, 449, 2194

Patruno, A., & Watts, A. L. 2012, ArXiv e-prints, arXiv:1206.2727 [astro-ph.HE]

Patruno, A., Archibald, A. M., Hessels, J. W. T., et al. 2014, ApJ, 781, L3

Patterson, J. 1984, ApJS, 54, 443

—. 1994, PASP, 106, 209

—. 1998, PASP, 110, 1132

—. 2011, MNRAS, 411, 2695

Patterson, J., & Raymond, J. C. 1985, ApJ, 292, 550

Patterson, J., Uthas, H., Kemp, J., et al. 2013, MNRAS, 434, 1902

Patterson, J., Oksanen, A., Kemp, J., et al. 2016, ArXiv e-prints, arXiv:1603.00291 [astro-ph.SR]

Paxton, B., Bildsten, L., Dotter, A., et al. 2011, ApJS, 192, 3

Perez-Becker, D., & Showman, A. P. 2013, ApJ, 776, 134

Phinney, E. S., Evans, C. R., Blandford, R. D., & Kulkarni, S. R. 1988, Nature, 333, 832

Politano, M. 1996, ApJ, 465, 338

—. 2004, ApJ, 604, 817

Pollacco, D. L., Skillen, I., Collier Cameron, A., et al. 2006, PASP, 118, 1407

Popov, S. B., Lipunov, V. M., Prokhorov, M. E., & Postnov, K. A. 1998, Astronomy Reports, 42, 29

Predehl, P., & Schmitt, J. H. M. M. 1995, A&A, 293, 889

Pretorius, M. L. 2009, MNRAS, 395, 386

—. 2014, ArXiv e-prints, arXiv:1407.3149 [astro-ph.SR]

Pretorius, M. L., & Knigge, C. 2012, MNRAS, 419, 1442

Pretorius, M. L., Knigge, C., & Kolb, U. 2007, MNRAS, 374, 1495

Pretorius, M. L., Knigge, C., & Schwope, A. D. 2013, MNRAS, 432, 570

Pringle, J. E. 1981, ARA&A, 19, 137

Rappaport, S., Verbunt, F., & Joss, P. C. 1983, ApJ, 275, 713

Reiners, A., & Basri, G. 2007, ApJ, 656, 1121

Ritter, H., & Kolb, U. 2003, A&A, 404, 301

Roberts, M. S. E. 2013, in IAU Symposium, Vol. 291, IAU Symposium, ed. J. van Leeuwen, 127

Robin, A. C., Reylé, C., Derrière, S., & Picaud, S. 2003, A&A, 409, 523

Robinson, E. L., Barker, E. S., Cochran, A. L., Cochran, W. D., & Nather, R. E. 1981, ApJ, 251, 611

Rosen, S. R., Webb, N. A., Watson, M. G., et al. 2016, A&A, 590, A1

Roy, J., Bhattacharyya, B., & Ray, P. S. 2014, The Astronomer's Telegram, 5890

Ruciński, S. M. 1969, Acta Astron., 19, 245

Savoury, C. D. J., Littlefair, S. P., Dhillon, V. S., et al. 2011, MNRAS, 415, 2025

Scaringi, S., Maccarone, T. J., Hynes, R. I., et al. 2015a, MNRAS, 451, 3857

Scaringi, S., Maccarone, T. J., Kording, E., et al. 2015b, Science Advances, 1, e1500686

Schenker, K., Kolb, U., & Ritter, H. 1998, MNRAS, 297, 633

Schreiber, M. R., & Gänsicke, B. T. 2003, A&A, 406, 305

Schreiber, M. R., Zorotovic, M., & Wijnen, T. P. G. 2016, MNRAS, 455, L16

Sesar, B., Ivezić, Ž., Lupton, R. H., et al. 2007, AJ, 134, 2236

Shahbaz, T., Linares, M., Nevado, S. P., et al. 2015, MNRAS, 453, 3461

Shakura, N. I., & Sunyaev, R. A. 1973, A&A, 24, 337

Shara, M., Moffat, A., Potter, M., Bode, M., & Stephenson, F. R. 1993, in Annals of the Israel Physical Society, Vol. 10, Cataclysmic Variables and Related Physics, ed. O. Regev & G. Shaviv, 84

Shen, K. J., & Bildsten, L. 2009, ApJ, 692, 324

Showman, A. P. 2016, Nature, 533, 330

Showman, A. P., & Kaspi, Y. 2013, ApJ, 776, 85

Skumanich, A. 1972, ApJ, 171, 565

Smak, J. 1971, Acta Astron., 21, 15

Smedley, S. L., Tout, C. A., Ferrario, L., & Wickramasinghe, D. T. 2015, MNRAS, 446, 2540

Smith, M. A. 1979, PASP, 91, 737

Sokoloski, J. L. 2003, Journal of the American Association of Variable Star Observers (JAAVSO), 31, 89

Solheim, J.-E. 2010, PASP, 122, 1133

Spruit, H. C. 1998, ArXiv Astrophysics e-prints, arXiv:astro-ph/9806141

Srinivasan, G. 2010, New Astron. Rev., 54, 93

Stappers, B. W., Archibald, A., Bassa, C., et al. 2013, The Astronomer's Telegram, 5513, 1

Stappers, B. W., Archibald, A. M., Hessels, J. W. T., et al. 2014, ApJ, 790, 39

Steeghs, D., Marsh, T., Knigge, C., et al. 2001, ApJ, 562, L145

Stehle, R., Kolb, U., & Ritter, H. 1997, A&A, 320, 136

Stehle, R., Ritter, H., & Kolb, U. 1996, MNRAS, 279, 581

Stephens, D. C., Leggett, S. K., Cushing, M. C., et al. 2009, ApJ, 702, 154

Strader, J., Chomiuk, L., Cheung, C. C., et al. 2015, ApJ, 804, L12

Szkody, P., Fraser, O., Silvestri, N., et al. 2003, AJ, 126, 1499

Szkody, P., Henden, A., Mannikko, L., et al. 2007, AJ, 134, 185

Takata, J., Li, K. L., Leung, G. C. K., et al. 2014, ApJ, 785, 131

Tassoul, J.-L., & Tassoul, M. 1992, ApJ, 395, 259

Tauris, T. M. 2012, Science, 335, 561

Tauris, T. M., & Savonije, G. J. 1999, A&A, 350, 928

Thorstensen, J. R., & Armstrong, E. 2005, AJ, 130, 759

Townsley, D. M., & Bildsten, L. 2003, ApJ, 596, L227

Townsley, D. M., & Gänsicke, B. T. 2009, ApJ, 693, 1007

Truran, J. W. 2002, in Astronomical Society of the Pacific Conference Series, Vol. 261, The Physics of Cataclysmic Variables and Related Objects, ed. B. T. Gänsicke, K. Beuermann, & K. Reinsch, 576

Tulloch, S. M., Rodríguez-Gil, P., & Dhillon, V. S. 2009, MNRAS, 397, L82

Unda-Sanzana, E., Marsh, T. R., Gänsicke, B. T., et al. 2008, MNRAS, 388, 889

Uthas, H., Knigge, C., Long, K. S., Patterson, J., & Thorstensen, J. 2011, MNRAS, 414, L85

Uttley, P., & McHardy, I. M. 2001, MNRAS, 323, L26

van den Heuvel, E. P. J., & van Paradijs, J. 1988, Nature, 334, 227

van der Klis, M. 1989, ARA&A, 27, 517

Verbunt, F., & Zwaan, C. 1981, A&A, 100, L7

Vernet, J., Dekker, H., D'Odorico, S., et al. 2011, A&A, 536, A105

Vestergaard, M., & Wilkes, B. J. 2001, ApJS, 134, 1

von Zeipel, H. 1924, MNRAS, 84, 665

Wade, R. A., & Horne, K. 1988, ApJ, 324, 411

Wang, X., Wang, Z., & Morrell, N. 2013, ApJ, 764, 144

Wang, Z., Tziamtzis, A., Kaplan, D. L., et al. 2014, The Astronomer's Telegram, 6103

Warner, B. 1995, Cambridge Astrophysics Series, 28

Warner, B. 2001, in Astronomical Society of the Pacific Conference Series, Vol. 246, IAU Colloq. 183: Small Telescope Astronomy on Global Scales, ed. B. Paczynski, W.-P. Chen, & C. Lemme, 159

Warner, B., & Nather, R. E. 1971, MNRAS, 152, 219

Watson, C. A., Steeghs, D., Shahbaz, T., & Dhillon, V. S. 2007, MNRAS, 382, 1105

White, H. E., Baumgarte, T. W., & Shapiro, S. L. 2012, ApJ, 752, 122

Wijnands, R., & van der Klis, M. 1998, Nature, 394, 344

Woosley, S., & Janka, T. 2005, Nature Physics, 1, 147

Woudt, P. A., Warner, B., & Pretorius, M. L. 2004, MNRAS, 351, 1015

Wright, N. J., & Drake, J. J. 2016, Nature, 535, 526

Wynn, G. A., & King, A. R. 1995, MNRAS, 275, 9

Wynn, G. A., King, A. R., & Horne, K. 1997, MNRAS, 286, 436

Yan, Z., & Yu, W. 2015, ApJ, 805, 87

York, D. G., Adelman, J., Anderson, Jr., J. E., et al. 2000, AJ, 120, 1579

Yungelson, L., & Livio, M. 1998, ApJ, 497, 168

Zahn, J.-P. 1975, A&A, 41, 329

Zorotovic, M., Schreiber, M. R., & Gänsicke, B. T. 2011, A&A, 536, A42

Zorotovic, M., Schreiber, M. R., Parsons, S. G., et al. 2016, MNRAS, 457, 3867